Modeling of Multicomponent Coatings

A dissertation submitted to the Graduate School of the University of Minnesota by

Christopher Karl-Olof Larsson

In partial fulfillment of the requirements for the degree of Doctor of Philosophy

Advisor: Satish Kumar

May 2023

Acknowledgments

The last five years have been an amazing journey. There are so many people that have helped to make this achievement possible. First and foremost, I would like to thank my advisor, Dr. Satish Kumar, for his guidance. He provided me with all of the resources I needed to grow into a proficient and independent researcher. Satish taught me how to approach and think about problems, and I cannot thank him enough for the growth I have seen in myself.

Of course, this would not have been possible without the support from my parents and my fiance, Ethan. They mean the world to me, and this journey would have been so much more difficult without them. There are too many things to thank them for individually, but I want to especially thank them for putting up with my nearly nocturnal lifestyle.

Finally, I would like to thank all of the Kumar group members, especially Saurabh and Ninad, for the countless discussions we have had (both intellectual and casual). Even though they could be brief, and whether it was discussing a derivation or simply venting about numerical simulations not converging, these conversations helped immensely. Furthermore, I extend my thanks to the CEMS department as well as the Industrial Partnership for Research in Interfacial and Materials Engineering of the University of Minnesota for supporting the work presented in this thesis. In addition, I am grateful for a fellowship awarded by the PPG Foundation as well as the Minnesota Supercomputing Institute (MSI) for providing computing resources.

dedicated to Mom and Dad and my fiance, Ethan

"Fire and smoke, flame and rage."

Contents

List of Figures

List of Tables

Chapter 1

Introduction

I Motivation and Overview

Coatings are integral to numerous industrial processes ranging from the mass-production of chocolate bars to the meticulous fabrication of life-saving stents.[1–11] The formulation and application of these coatings is a complex process that is crucial to obtaining desired properties; the chocolate coating on candy bars should be glossy and smooth, while the coating on stents must uniformly elute drugs to prevent inflammation and clotting. Such a wide range of applications requires a diverse set of chemistry and application techniques, so effectively improving and optimizing coating processes requires a deep understanding of the related physics.

Coatings can be applied in many ways depending on the application, including slot-die[12] and spray coating and inkjet printing[7]. Often, the coating is first applied as a liquid to aid with spreading and then is solidified through a mechanism such as drying or UV curing. The evolution of the liquid coating during this time is

paramount in determining the quality of the final product, since aspects such as thickness or species concentration gradients are desirable for some applications and catastrophic in others. Thus, it is important to fundamentally understand the evolution of these liquid coatings so that their properties can be optimized for the desired application.

There are many phenomena that effect the evolution of liquid coatings. For example, in a multicomponent coating, capillary flow, Marangoni flow, species transport, and evaporation all play an important role. Theoretical modeling is a powerful tool for developing fundamental understanding because it allows for systematic exploration of these phenomena that may otherwise require costly experimentation. Furthermore, the understanding gained is often not limited to the specific system the model describes. By utilizing theoretical models of liquid coatings, one can gain a deep fundamental understanding of how the liquid coating evolves as it solidifies – aiding in the design and improvement of coating processes.

This thesis utilizes theoretical modeling to develop fundamental understanding of challenging problems in coating processes. Chapter 2 focuses on multilayer coating; coatings are often applied in multiple layers, each with distinct functionality that are usually applied separately. A prominent example is automobile paint which has primer, pigment, and gloss layers. The efficiency and speed of such processes can be increased if the layers are applied at the same time – known as "wet-on-wet" coating.[12] However, this makes it more difficult to control the properties of the coating, so chapter 2 develops a fundamental understanding of

how these multilayer coatings evolve.

Chapter 3 focuses on developing understanding of theoretical models for evaporating liquid coatings. As a multicomponent liquid coating dries, a concentration gradient develops where nonvolatile components accumulate at the liquid-air interface. Since the coating is typically thin, vertical diffusion is often considered rapid enough to smooth out any depth-wise concentration gradients, giving rise to the vertical-averaging (VA) approximation.[13] This considerably reduces the complexity of including evaporation in a theoretical model, but formally requires strict assumptions on the Péclet number that are often not valid for physical systems (e.g., coatings containing large particles). Nevertheless, the convenience of the VA approximation has led to its use in numerous studies that often violate its formal assumptions.[14–22] Thus, chapter 3 presents a systematic evaluation of the VA approximation and develops a fundamental understanding of the mechanism it fails to capture and when they are important to the film evolution.

A major complication that arises when modeling drying coatings, especially those that involve discrete liquid droplets such as inkjet printing, is modeling the evaporation process. Existing models for evaporation are largely distinguished by which part of the evaporation process is assumed to be rate limiting; the two predominant evaporation models are the one-sided model and the diffusion-limited model. Both have been widely used in previous work, but have vastly different formulations and it is often unclear *a priori* which evaporation model is most appropriate for a physical system. A fundamental understanding of the

differences between these evaporation models is lacking, so chapter 4 develops this understanding by making direct comparisons between predictions from the two models.

II Background

This section provides background on the physics and mathematics that are useful for understanding the modeling work presented in the remainder of this thesis. First, §A introduces the phenomena of capillary flow, Marangoni flow, and evaporation, all of which are central to the evolution of liquid coatings and the work presented in this thesis. Next, §B discusses the basics of lubrication theory, why it is applicable to liquid coatings, and how it simplifies theoretical models such as those used in this thesis.

A Capillary Flow, Marangoni Flow, and Evaporation

Capillary flow arises from gradients in the liquid-air interface curvature and tends to create a uniform coating thickness. By the Young-Laplace equation, the pressure difference ΔP due to a curved interface is

$$\Delta P \sim \frac{\sigma}{R}, \tag{1.1}$$

where σ is the surface tension and R is the radius of curvature. As the interface curves and R decreases, the pressure increases. This drives flow to other regions of low curvature (having lower pressure), acting to level the interface over

time. Depending on the application, this can be either desirable (e.g., paints) or undesirable (e.g., topographical patterning[23]).

Marangoni flow arises from gradients in surface tension that are caused by gradients in composition, temperature, or other quantities that affect surface tension. Regions of higher surface tension "pull" on neighboring regions of lower surface tension, creating a shear stress that drives flow from low to high surface tension. In practical applications, this effect can arise from a multitude of phenomena, including contaminants in the coating liquid or thermal gradients from evaporation. The flows that develop typically cause nonuniformity in the coating thickness – undesirable in many scenarios but desirable in others. Thus it is important that we fundamentally understand both capillary and Marangoni flow in liquid coatings so they can be tuned towards the desired outcome.

Evaporation is central to liquid coatings since it is the primary mechanism through which they are solidified. Evaporation proceeds through two main steps: Liquid first undergoes phase change into vapor and is then transported away from the liquid-gas interface into the surroundings. Evaporation typically cools the liquid and can lead to gradients in temperature that cause Marangoni flow and complicate the evolution of the coating. Furthermore, in multicomponent coatings, nonvolatile components accumulate near the liquid-air interface and create composition gradients. Due to this, evaporation and Marangoni flow (both solutal and thermal) are coupled together and can lead to unexpected behaviors in liquid coatings.

B Lubrication Theory and Free Surfaces

Lubrication theory exploits a disparity in length scales to greatly simplify the hydrodynamics of a theoretical model. For example, a coated liquid is often very thin compared to the extent of the area it is covering (e.g., paint), so lubrication theory can be applied. In a standard hydrodynamic model, one takes the liquid velocity vector $\mathbf{v}$ and pressure p to be governed by the Navier-Stokes equations. Furthermore, the position of the liquid-air interface (or alternatively, the thickness of the coating) is an unknown h governed by a kinematic condition. In general, one then has five equations to solve for the five unknowns. Since the position of the interface is unknown, this is a free-surface problem and solving the Navier-Stokes equations becomes significantly more complex.

However, leveraging lubrication theory, analytical expressions can be developed for the velocities and pressure, reducing the number of equations and unknowns to one. This greatly reduces the model complexity and makes it much easier to develop fundamental insight into complex physical systems. The equation that results for the liquid thickness h generally has the nondimensional form

$$\frac{\partial h}{\partial t} = \underbrace{\frac{Ca}{3}\boldsymbol{\nabla}\cdot\left(h^3\boldsymbol{\nabla}p\right)}_{\text{Capillary Flow}} - \underbrace{\frac{Ma}{2}\boldsymbol{\nabla}\cdot\left(h^2\boldsymbol{\nabla}\sigma\right)}_{\text{Marangoni Flow}} - \underbrace{EJ}_{\text{Evaporation}} \quad . \tag{1.2}$$

This partial differential equation relates the change in thickness h over time t to the physical phenomena discussed in §A. The magnitude of the nondimensional groups (capillary number Ca, Marangoni number Ma, and evaporative number

E) give the relative importance of that physical phenomena in comparison to the others. Depending on the system, the surface tension σ can be a function of solute or surfactant concentration, temperature, and other quantities, so equation (1.2) is usually coupled to additional conservation equations for the relevant quantities. Furthermore, an evaporation model is required to express the evaporative flux J in terms of other quantities such as h or the liquid temperature.

Equation (1.2) underpins all of the theoretical models used in this thesis; by solving this equation, we can predict how the liquid coating evolves and develop fundamental understanding of coating processes. However, it is usually not possible to obtain analytical solutions, so numerical methods must be employed to solve equation (1.2). An in-depth discussion of numerical methods is beyond the scope of this thesis, but each chapter briefly discusses the numerical methods used to solve the relevant governing equations.

Chapter 2

Nonuniformities in Miscible Two-Layer Two-Component Thin Liquid Films*

I Introduction

Ranging from the production of OLED screens,[1] printed electronics,[2] and pharmaceuticals[3] to the tear-film protecting our eyes,[4,5] thin liquid films are ubiquitous; they exhibit many fascinating and exploitable behaviors that underlie numerous industrial processes. These processes produce lithium-ion batteries,[6] solar and fuel cells,[25] drug-delivery devices,[3] and many other products where desired functionality requires that the films have controlled thickness and species concentration distributions.

Advanced applications often require that coated films consist of numerous layers with varying components. These films are deposited through a number of

*Reprinted with permission from Physical Review Fluids 2021, 6, 3, 034004. Copyright 2021 American Physical Society.[24]

processes such as slot coating, curtain coating, and spray coating. However, small perturbations from vibrations, imperfect mixing, and other sources can cause variations in film height and component concentration with potentially disastrous effects on coating quality. While variations in the film height generate capillary flows that level the film, variations in component concentration can cause surface-tension gradients and thus Marangoni flow. Sufficiently strong Marangoni flow leads to film rupture (dewetting) and is catastrophic to coating quality. However, even minor instabilities that result in small nonuniformities may cause a significant quality degradation, so it is crucial to understand the evolution of nonuniformities in thin liquid films.

The growth of nonuniformities in liquid films from Marangoni flow has been extensively studied in one-layer systems.[10,26] The characteristic case of a binary (two-component) film has received considerable attention because it forms a foundation from which we may understand more complex systems. Serpetsi and Yiantsios[27] studied the stability of an evaporating one-layer binary film through linear stability analysis and nonlinear simulations, finding modes of instability similar to those investigated by Pearson[28] and Scriven and Sternling.[29,30] Including a variable viscosity, Yiantsios et al.[31] examined the nonlinear evolution of film-height and concentration nonuniformities in drying polymer films. Furthermore, the influence of substrate geometry[14,32], soluble and insoluble surfactants[4,13,14], evaporation rate[14,27,33,34], and colloidal particles[14,34,35] has been extensively explored in one-layer systems.

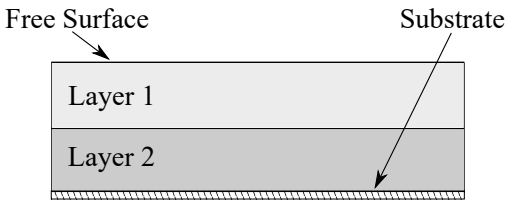

Figure 2.1: Schematic of a two-layer liquid film resting on a solid substrate. If the liquid layers are miscible, there is no distinct interface between them.

However, coated films are often comprised of multiple liquid layers to provide advanced functionality.[36–39] Horiuchi et al.[12] experimentally demonstrated dewetting of two-layer miscible films resting on solid substrates, but current theoretical understanding is largely limited to the case of immiscible liquids.[40–45]. Figure 2.1 shows a simple schematic of a two-layer film resting on a substrate with a deformable liquid-air interface (free surface). While the liquid-liquid interface between layers is depicted sharp in figure 2.1, it may be diffuse or even nonexistent if the layers are miscible. Through two-layer slot coating, Horiuchi et al.[12] coated two-layer films with an alcohol-based bottom layer and water-based top layer and examined the influence of liquid properties and film thickness ratios on dewetting. Because these layers are miscible, the only distinct fluid-fluid interface is the free surface depicted in figure 2.1.

When modeling species concentration in multicomponent films, many previous studies have employed a rapid-vertical-diffusion approximation.[13,14,46–48] To leading order, this approximation assumes species concentration is uniform through the film depth. This hinges on the assumptions that initial vertical concentration gradients are negligible and that vertical diffusion is rapid in comparison to other process time scales. Consequently, this approximation is not useful for studying

two-layer films where there may be a significant difference in species concentration between layers resulting in large vertical gradients. Although some previous work on the stability of liquid films has accounted for the presence of vertical concentration gradients,[4,27,31,32] there is limited understanding of their role in miscible multilayer films where large vertical gradients may be present initially. Fundamental understanding of the stability of miscible multilayer films is important in numerous coating applications,[12] but to the best of our knowledge a systematic theoretical investigation of the evolution of miscible multilayer films has yet to be reported.

In this work, we study the model problem of a nonvolatile two-layer binary film that approximates the conditions studied by Horiuchi et al.[12] (figure 1). The primary goal of this paper is to understand the mechanisms that generate film-height nonuniformities in two-layer miscible films, rather than to attempt a quantitative comparison with the experiments of Horiuchi et al.[12] To focus on the effects of solutal Marangoni flow, we choose to neglect evaporation and thermal Marangoni flows in this study. The rest of the paper is organized as follows. In §II, we present the mathematical model. In §III, we identify regions of the problem parameter space with qualitatively different dynamics. We also develop analytical expressions that provide insight into the underlying physical mechanisms. In §IV, we present a parametric study to highlight the key factors influencing film uniformity. Conclusions are given in §V.

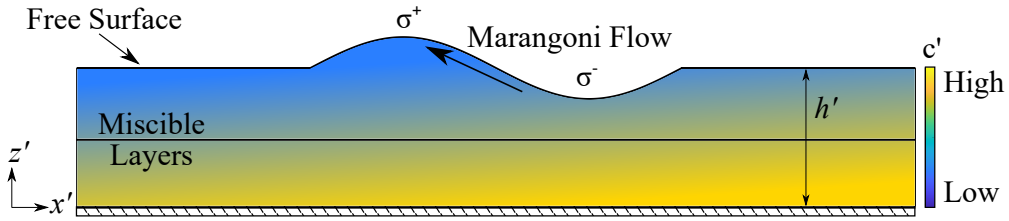

Figure 2.2: Schematic of the model geometry of two miscible liquid layers resting on a solid substrate. One liquid is considered the "solvent" and the other the "solute". Yellow indicates a higher concentration of solute, and σ^+ denotes a locally high surface tension while σ^- denotes a locally low surface tension that arise from solute concentration gradients. The resulting surface-tension gradient causes formation of a film-height nonuniformity, through Marangoni flow, from an initially flat interface (see figure 2.1).

II Mathematical Model

We model the evolution of film height and species concentration in a thin liquid film resting on a solid substrate as shown in figure 2.2. Film height $h' = h'(t', x')$ and solute concentration $c' = c'(t', x', z')$ vary with time t' and the spatial variables x' and z'. The liquid is comprised of two miscible liquids, one of which is labeled the "solvent" and the other the "solute". When the solvent and solute surface tensions differ, solute concentration gradients create Marangoni stresses that drive Marangoni flow at the liquid-air interface (free surface) as depicted in figure 2.2. We enforce periodic conditions in x', assuming edge effects are negligible, and neglect evaporation and thermal Marangoni flows to focus on the effects of solutal Marangoni flow.

A Hydrodynamics

The liquid film is assumed Newtonian with constant viscosity μ and density ρ. Surface tension σ' is scaled by the solvent surface tension σ_0, and the solute concentration c' by an initial concentration c_0. The vertical coordinate z' is scaled

by the initial film height H, while the lateral coordinate x' is scaled by the length scale L obtained from balancing viscous and Marangoni stresses at the interface:

$$\mu \frac{\sigma_0 H^2}{\mu L^3} \sim \frac{\Delta\sigma\omega_0}{L} \quad \Rightarrow \quad L \sim \frac{H}{\sqrt{Ma}}. \tag{2.1}$$

The viscous scale used in this balance is based on a capillary velocity and arises from considering mass and x-momentum balances. The Marangoni number $Ma = \Delta\sigma\omega_0/\sigma_0$, where $\Delta\sigma$ is the solvent and solute surface-tension difference (assumed positive), and ω_0 is the initial mass or mole fraction of solute. The film is assumed thin so that the ratio of the characteristic lengths $\epsilon = H/L \ll 1$ allowing the application of lubrication theory. This assumption is simply that of a small Marangoni number $\sqrt{Ma} = \epsilon \ll 1$ and has been used in previous work.[27]

The liquid velocities, v_x' and v_z', and pressure p' are governed by the Navier-Stokes equations with no-slip and no-penetration at the substrate and stress balances at the liquid-air interface. The film height h' deforms in response to flow in the film and is governed by the kinematic condition. A normal stress balance at the interface reveals that an appropriate scale for the pressure is $p^* = \sigma_0\epsilon^2/H$, and an x-momentum balance coupled with the kinematic condition gives the x-velocity scale $v_x^* = \epsilon^3\sigma_0/\mu$ and time scale $t^* = H/v_x^*\epsilon$. Finally, bulk mass conservation gives the z-velocity scale $v_z^* = \epsilon v_x^*$ (see the appendix for a derivation of these scales). Thus, we introduce the dimensionless variables (indicated without a prime super-

script):

$$x' = \epsilon^{-1} H x, \qquad z' = H z, \qquad h' = H h, \qquad \sigma' = \sigma_0 \sigma, \qquad c' = c_0 c,$$

$$v_x' = v_x^* v_x, \qquad v_z' = \epsilon v_x^* v_z, \qquad p' = p^* p, \qquad t' = t^* t. \tag{2.2}$$

The surface tension σ is assumed to vary linearly with the solute concentration c at the interface according to

$$\sigma = 1 - Ma\, c|_{z=h}. \tag{2.3}$$

This assumes a dilute solute ($\omega_0 \ll 1$) and has been used in many previous studies (e.g., Refs. 27, 14, and 49). Retaining only leading-order terms in the Navier-Stokes equations yields the lubrication equations governing the liquid velocity and pressure:

$$\frac{\partial^2 v_x}{\partial z^2} = \frac{\partial p}{\partial x}, \tag{2.4}$$

$$\frac{\partial p}{\partial z} = 0, \tag{2.5}$$

$$\frac{\partial v_x}{\partial x} + \frac{\partial v_z}{\partial z} = 0. \tag{2.6}$$

In dimensionless form, the no-slip, no-penetration, normal stress balance, and tangential stress balance give the boundary conditions

$$v_x|_{z=0} = v_z|_{z=0} = 0, \tag{2.7}$$

$$p|_{z=h} = -\frac{\partial^2 h}{\partial x^2}, \tag{2.8}$$

$$\left.\frac{\partial v_x}{\partial z}\right|_{z=h} = -\frac{\partial c|_{z=h}}{\partial x}. \tag{2.9}$$

Note that due to the choice of the lateral domain size $L = H/\sqrt{Ma}$, the Marangoni number Ma does not appear in tangential stress balance (2.9). Solving equations (2.4), (2.5), and (2.6) subject to these conditions gives explicit expressions for the liquid velocities:

$$v_x = -\left(\frac{1}{2}z^2 - hz\right)\frac{\partial^3 h}{\partial x^3} - \frac{\partial c|_{z=h}}{\partial x}z, \tag{2.10}$$

$$v_z = \left(\frac{1}{6}z^3 - \frac{1}{2}hz^2\right)\frac{\partial^4 h}{\partial x^4} + \frac{1}{2}\left(\frac{\partial^2 c|_{z=h}}{\partial x^2} - \frac{\partial h}{\partial x}\frac{\partial^3 h}{\partial x^3}\right)z^2. \tag{2.11}$$

Mass conservation at the interface $z = h$ requires the kinematic condition

$$v_z = \frac{\partial h}{\partial t} + v_x\frac{\partial h}{\partial x}, \tag{2.12}$$

and inserting velocities (2.10) and (2.11) yields the thin-film equation

$$\frac{\partial h}{\partial t} = \underbrace{-\frac{1}{3}\frac{\partial}{\partial x}\left[h^3\frac{\partial^3 h}{\partial x^3}\right]}_{\text{Capillary Flow}} + \underbrace{\frac{1}{2}\frac{\partial}{\partial x}\left[h^2\frac{\partial c|_{z=h}}{\partial x}\right]}_{\text{Marangoni Flow}}. \tag{2.13}$$

This equation describes the change in film height h over time in terms of contributions from capillary flow and Marangoni flow. It is coupled to the evolution of solute concentration c through Marangoni flow and subject to the initial condition $h_0 = 1$.

B Solute Concentration and Initial Condition

The solute is assumed to have constant diffusivity D in the solvent and is governed by the dimensionless convection-diffusion equation

$$\frac{\partial c}{\partial t} + v_x \frac{\partial c}{\partial x} + v_z \frac{\partial c}{\partial z} = \frac{1}{Pe}\frac{\partial^2 c}{\partial x^2} + \frac{1}{\epsilon^2 Pe}\frac{\partial^2 c}{\partial z^2}. \tag{2.14}$$

Here, the Péclet number $Pe = Hv_x^*/D\epsilon$ gives the ratio between the lateral diffusive and convective time scales. Similarly, $\epsilon^2 Pe$ gives the ratio between the vertical diffusive and convective time scales. Note that equation (2.14) assumes Fickian diffusion in the liquid film.

Previous studies often use one of two approximations to simplify equation (2.14). If the vertical diffusion time is small ($\epsilon^2 Pe \ll 1$), one may solve for a leading-order, vertically uniform concentration profile.[13,14,46] However, vertical gradients are large in the system we seek to investigate, so this approximation is not applicable. Studies that include vertical gradients argue that lateral diffusion is negligible, since $\epsilon^2 Pe \ll Pe$, and neglect its contribution in equation (2.14) (e.g., Refs. 4 and 27). We do not neglect lateral diffusion in this work; as will be seen in §III and §IV, lateral diffusion plays a key role in the behavior we observe. Therefore, we retain all terms in equation (2.14) and apply no-flux conditions:

$$\left.\frac{\partial c}{\partial z}\right|_{z=0} = 0, \qquad \left.\frac{\partial c}{\partial z}\right|_{z=h} - \epsilon^2 \left.\frac{\partial h}{\partial x}\,\frac{\partial c}{\partial x}\right|_{z=h} = 0. \tag{2.15}$$

In the experiments of Horiuchi et al.,[12] a solid substrate was coated with two-

layer films consisting of an ethanol-rich bottom layer and ethanol-depleted top layer. To approximate this two-layer structure, the initial concentration profile has a solute-rich bottom layer and a solute-depleted top layer, achieved by the transition function

$$T(z;\, h_b, s) = \begin{cases} 1 & w \le 0 \\ \frac{\exp\left(-\frac{1}{1-w}\right)}{\exp\left(-\frac{1}{1-w}\right)+\exp\left(-\frac{1}{w}\right)} & 0 < w < 1 \\ 0 & 1 \le w \end{cases} \quad \text{where} \quad w = \frac{z-(h_b-1/s)}{2/s}. \tag{2.16}$$

Here, h_b is the dimensionless bottom-layer thickness and s is the slope of the transition between layers. There are numerous other functions that could be used, such as an inverse or hyperbolic tangent function or the Heaviside step function (obtained when $s \to \infty$). However, the inverse and hyperbolic tangent functions do not satisfy boundary conditions (2.15) analytically because their derivatives never vanish. Furthermore, a step function is numerically undesirable because it leads to the Gibbs phenomenon when numerical solutions are attempted. In contrast, transition function (2.16) analytically satisfies no-flux boundary conditions while preserving the spectral accuracy of the numerical method presented in §C.

The initial condition c_0 is constructed to model a two-layer film with a lateral perturbation to the concentration profile that is initially localized to the diffuse region between layers:

$$c_0(x, z; h_b, s, c_p, \alpha, \upsilon) = T(z; h_b, s)\left(1 + c_p \cos(\alpha x) e^{-\frac{(z-h_b)^2}{2\upsilon^2}}\right). \tag{2.17}$$

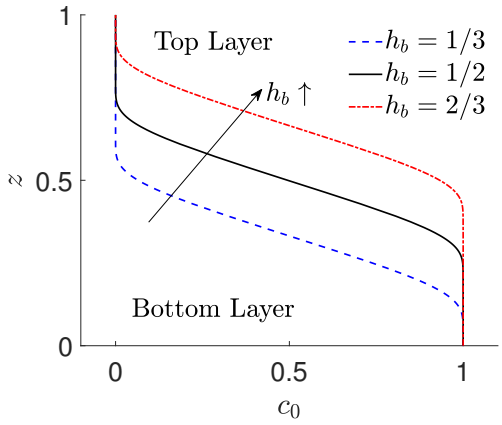

Figure 2.3: Cross-sections of the initial condition $c_0(x, z)$ for three bottom layer thicknesses h_b at $x = \pi/\alpha$. The top layer corresponds to layer 1 and the bottom layer to layer 2 in figure 2.1. As the bottom layer thickness h_b increases, the transition between layers occurs at larger z (layer 2 is thicker and layer 1 thinner in figure 2.1). The perturbation centered at $z = h_b$ cannot be seen due to its small amplitude.

Plots of c_0 that are used in §III and §IV are shown in figure 2.3. The parameters c_p and α are, respectively, the magnitude and wavenumber of the lateral perturbation while υ is the standard deviation of the Gaussian that localizes the perturbation to the diffuse region between layers. This work takes $s = 3$ and $\upsilon = 0.1$, and the influence of h_b, c_p, and α is investigated in §IV. The parameter s is fixed at the largest value that is numerically practical, while υ is fixed at a value that strongly localizes the perturbation to the diffuse region. This localization is important when analyzing the effects of h_b as will be shown in §C. For the parameters used in this work, the perturbation described in equation (2.17) cannot be seen in figure 2.3 due to its small amplitude but leads to a wealth of interesting behavior.

Actual coating processes are subject to small, effectively random perturbations that arise from vibrations, imperfect mixing, and other sources. Initial condition (2.17) is a model perturbation that allows us to probe fundamental mechanisms,

whereas random noise would involve a distribution of Fourier modes. Thus, for the results presented in §III, accompanying simulations were run where the sinusoidal perturbation in equation (2.17) was replaced with a finite sum of Fourier modes over a uniformly distributed set of wavenumbers and amplitudes to approximate random noise. Only small quantitative shifts were observed in the results using random noise, so those results are not shown.

C Parameter Values and Numerical Methods

There are two dimensionless groups that appear in convection-diffusion equation (2.14). The first is the Péclet number Pe, which gives the ratio of the lateral diffusive and convective time scales. The second is the Marangoni number $Ma = \epsilon^2$, which gives the ratio of Marangoni forces to capillary forces but also defines the lateral length scale $L = H/\sqrt{Ma}$. The Marangoni number appears in the lumped parameter $\epsilon^2 Pe = MaPe$ that gives the ratio of the vertical diffusive and convective time scales. Typical values of dimensional and dimensionless parameters are given in tables 2.1 and 2.2, respectively. The effects of varying Pe and Ma are investigated in §III and §D respectively.

As formulated in §B, convection-diffusion equation (2.14) is subject to no-flux boundary condition (2.15) at the moving boundary $z = h(t, x)$. To circumvent numerically solving a moving-boundary problem, the coordinate transformation $(x, z, t) \mapsto (\zeta, \eta, \tau)$ is performed through the relations[4]

$$\eta = \frac{z}{h}, \qquad \frac{\partial \zeta}{\partial x} = 1, \qquad \frac{\partial \tau}{\partial t} = 1. \tag{2.18}$$

Table 2.1: Important dimensional parameters and typical values. Note that, typically, $\Delta\sigma \sim \sigma_0$.[12]

Parameter	Definition	Typical Values
H (m)	film thickness	10^{-5}-10^{-4}
μ (Pa s)	solvent viscosity	10^{-4}-10^{-3}
σ_0 (N/m)	solvent surface tension	10^{-2}-10^{-1}
$\Delta\sigma$ (N/m)	solvent/solute surface-tension difference	10^{-2}-10^{-1}
D (m^2/s)	solute diffusivity	10^{-9}
ω_0	solute mass/mole fraction	10^{-2}-10^{-1}

Here, η is a scaled vertical coordinate, ζ is the lateral coordinate, and τ is the time coordinate. In this new coordinate system, the boundary at $\eta = 1$ is constant in time and space. However, the governing equations become appreciably more complex with the corresponding derivative transformations

$$\frac{\partial}{\partial x} = \frac{\partial}{\partial \zeta} - \frac{\eta}{h}\frac{\partial h}{\partial \zeta}\frac{\partial}{\partial \eta}, \qquad \frac{\partial}{\partial z} = \frac{1}{h}\frac{\partial}{\partial \eta}, \qquad \frac{\partial}{\partial t} = \frac{\partial}{\partial \tau} - \frac{\eta}{h}\frac{\partial h}{\partial \tau}\frac{\partial}{\partial \eta}. \tag{2.19}$$

After applying transformation (2.18) to equations (2.13) and (2.14), a psuedospectral method is employed to solve the resulting set of coupled fourth-order nonlinear partial differential equations on the constant domain $\zeta \in (0, 2\pi/\alpha)$ and $\eta \in (0, 1)$.[4,50,51] Periodic conditions in ζ warrant an expansion in Fourier modes, while the finite domain in η warrants an expansion in Chebyshev polynomials. Therefore, the film height h is expanded in a basis of Fourier modes and the solute concentration c in a tensor-product basis of Fourier modes and Chebyshev polynomials with 20 Fourier modes and 140 Chebyshev polynomials. Furthermore, because the clustering of Chebyshev nodes is poor at resolving features in

Table 2.2: Important dimensionless parameters and typical values.

Parameter	Definition	Physical Meaning	Typical Values
ϵ	$H/L, \sqrt{Ma}$	vertical length/lateral length	10^{-2}-10^{-1}
Ma	$\Delta\sigma\omega_0/\sigma_0$	Marangoni forces/surface-tension forces	10^{-3}-10^{-1}
Pe	$H\sigma_0\epsilon^2/D\mu$	diffusion time/convection time	$1 - 10^6$

the center of the domain, the grid is stretched by applying an inverse sine transformation.[50,52,53] Finally, time integration is performed via MATLAB's built-in solver `ode15i` which is a variable-step, variable-order solver utilizing backward differentiation. The model and numerical method have been verified by reproducing results for pure film leveling and simple cases of one-layer binary films.[10,27]

III Nonuniformities in Miscible Two-Layer Films

We wish to study the mechanisms that may initiate dewetting, so we first discuss the mechanisms through which film-height nonuniformities are generated. With a solute-depleted top layer given by initial condition (2.17), there is initially no solute present at the interface $z = h$ (see figure 2.3). The lateral concentration defect localized to $z = h_b$ (equation (2.17)) lowers the concentration at $x = \pi/\alpha$ (the lateral center of the film). Thus, there is a smaller vertical concentration gradient driving diffusion toward the interface $z = h$ where $c = 0$. Vertical diffusion is therefore slower near the lateral center of the film, resulting in laterally nonuniform vertical diffusion of solute toward the interface.

Over time, a nonuniform concentration profile that mirrors the imposed defect will develop at the interface. This defect is a depletion of solute in the center of the film, causing a locally high surface tension and Marangoni stresses that drive flow toward the center of the film. As liquid accumulates, a crest in the film height will grow as depicted in figure 2.2. The crest represents a negative curvature of the interface and generates a positive capillary pressure that drives flow to level the crest. In this manner, Marangoni and capillary stresses compete as film-height nonuniformities grow.

Constrained by conservation of mass, the magnitude of concentration gradients and Marangoni stresses is limited and will be matched by capillary stresses if the film does not dewet. Once capillary stresses balance Marangoni stresses, growth of the crest stops and the film reaches its maximally deformed state. Subsequently, lateral diffusion relaxes concentration gradients to return the film to a uniform state. Film height evolution for $Pe = 10^4$ is shown in figure 2.4 (a), where the maximally deformed state (black line) has $\Delta h \approx 4 \times 10^{-2}$ (4% of the film thickness). As evolution continues, the film slowly returns to a uniform state as shown by the profile at $t = 10^4$ (red dashed line). To illustrate the concentration gradients that drive film-height deformation, a maximally deformed state at a larger Péclet number $Pe = 1.67 \times 10^5$ is given in figure 2.4 (b) with the solute concentration contour. Because diffusion is relatively slow, there are significant concentration gradients in both the lateral and vertical directions. As will be discussed in §B, the vertical gradients can actually contribute to the steepening of the lateral gradients shown in figure 2.4 (b). This is the primary driving force for

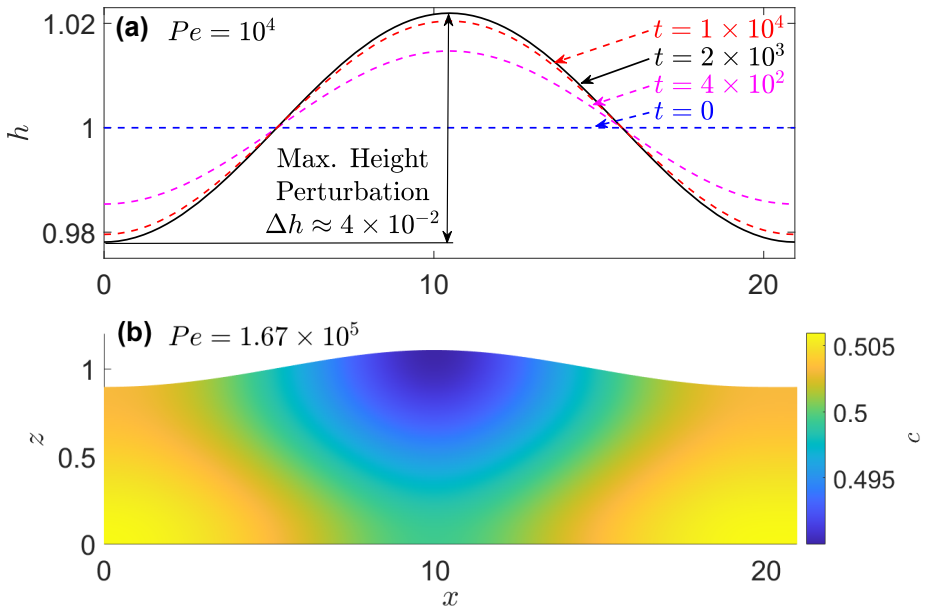

Figure 2.4: (a) Time evolution of the film height for $Pe = 10^4$. The maximum height perturbation Δh occurs at $t_{max} \approx 2 \times 10^3$ where the film-height profile is given by the solid black line. The perturbation slowly decays beyond this time as shown by the profile at $t = 10^4$. (b) Maximally deformed state for $Pe = 1.67 \times 10^5$ with solute concentration contour. This state occurs at $t \approx 9 \times 10^2$ after which the perturbation slowly decays through lateral diffusion. The remaining parameter values are $c_p = 10^{-2}$, $\alpha = 0.3$, $\epsilon = 0.1$, and $h_b = 0.5$.

the height perturbation $\Delta h \approx 2 \times 10^{-1}$ (20% of the film thickness) which is nearly an order of magnitude larger than that obtained for $Pe = 10^4$ in figure 2.4 (a).

Figure 2.4 shows that the value of Pe has a pronounced effect on film evolution. Parameters that play a role include the Péclet number Pe, the Marangoni number Ma, and the bottom-layer thickness h_b. The effects of varying these parameters are investigated in this section (§III), §D, and §C respectively. Two important parameters that appear in initial condition (2.17) are the perturbation magnitude c_p and wavenumber α, investigated in §A and §B. To characterize film nonuniformity and stability as these parameters vary, one may look to the maximum size of the height perturbation Δh and the time required to achieve it t_{max}. Larger Δh and smaller t_{max} represent larger nonuniformities that develop more rapidly and thus

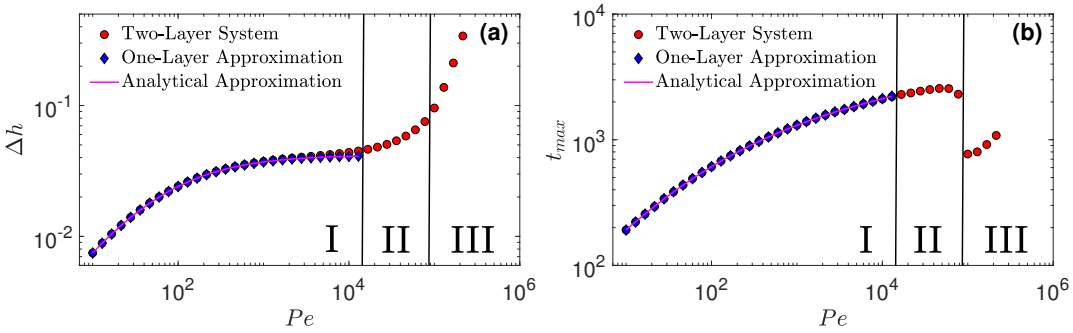

Figure 2.5: Plots of (a) the maximum height perturbation Δh and (b) the time to achieve it t_{max} at varying Pe. The plots are divided into three regions labeled I, II, and III. The blue diamond data points are predicted values from the one-layer approximation discussed in §A, and the solid magenta line is an analytical approximation for region I derived in §A.

indicate a less stable film.

For $\epsilon = 0.1$, $\alpha = 0.3$, $c_p = 10^{-2}$, and $h_b = 0.5$, figure 2.5 shows (a) Δh and (b) t_{max} over a wide range of Pe (red circles) where the labels I, II, and III indicate three distinct parameter regimes. Figure 2.5 (a) shows that Δh increases monotonically through all regions, while figure 2.5 (b) shows that t_{max} has a sharp drop at a critical Péclet number $Pe_{crit} \approx 10^5$ that indicates the transition into region III. The trends in figure 2.5 result from both the horizontal (Pe) and vertical ($\epsilon^2 Pe$) diffusive time scales increasing as Pe increases and are discussed by region in §A (rapid vertical diffusion), §B (transition region), and §C (convective steepening).

A Region I - Rapid Vertical Diffusion

In region I of figure 2.5, both the maximum height perturbation Δh and the time to achieve it t_{max} increase monotonically. In comparison to regions II and III, region I is at relatively low Pe so diffusion is relatively rapid. If rapid enough,

vertical diffusion will quickly smooth out any vertical concentration gradients and the system will behave as if it is vertically uniform. Therefore, we introduce a one-layer approximation where any initial vertical gradients are averaged out of initial condition (2.17) (this is what rapid vertical diffusion would achieve):

$$\overline{c_0}(x) = \int_0^1 c_0(x,z)\,dz = \underbrace{\int_0^1 T(z;h_b,s)\,dz}_{\text{Base State } c_b} + \underbrace{c_p \int_0^1 T(z;h_b,s) e^{-\frac{(z-h_b)^2}{2\upsilon^2}}\,dz}_{\text{Perturbation Magnitude } \overline{c_p}} \cos(\alpha x). \tag{2.20}$$

Equation (2.20) has contributions from a uniform base state c_b and a lateral sinusoidal perturbation with magnitude $\overline{c_p}$. Governing equations (2.13) and (2.14) are numerically solved from the initial condition $\overline{c_0}$ (rather than c_0) to yield the one-layer approximation shown in region I of figure 2.5 (blue diamonds). There is excellent agreement with the two-layer system, indicating that, in region I, vertical diffusion is sufficiently rapid to smooth out vertical gradients before the film begins to deform appreciably. This corresponds to the condition $\epsilon^2 Pe \ll t_{max}$, which is valid throughout region I as shown by the values of t_{max} in figure 2.5 (b) (recall that $\epsilon = 0.1$).

Having established that vertical diffusion is rapid in region I of figure 2.5, we address the trends in Δh and t_{max}. Increasing Pe corresponds to increasing the lateral diffusion time scale. Consequently, lateral concentration gradients decay less over a given time, resulting in larger Marangoni stresses and thus larger film-height perturbations. This mechanism can be described by a simple scaling relation, derived by considering thin-film equation (2.13) when growth of the crest

has stopped ($\partial h/\partial t = 0$). At this time, capillary stresses balance Marangoni stresses and thin-film equation (2.13) reduces to

$$h\frac{\partial^3 h}{\partial x^3} = \frac{3}{2}\frac{\partial c|_{z=h}}{\partial x}. \tag{2.21}$$

With rapid diffusion, the concentration perturbation magnitude is well-approximated by decay of the initial magnitude $\overline{c_p}$ through diffusion by the factor $\exp(-\alpha^2 t_{max}/Pe)$. This factor can be obtained by considering purely lateral diffusion. Noting that $h \sim 1$ and $\partial/\partial x \sim \alpha$ (due to periodicity), we have the relation

$$\Delta h \sim \alpha^{-2}\overline{c_p}\exp\big(-\alpha^2 t_{max}/Pe\big). \tag{2.22}$$

Relation (2.22) predicts an increase in Δh with increasing Pe due to slowing diffusion, and shows a scaling with α^{-2} that arises from the ratio of capillary stresses $\sim \alpha^4$ and Marangoni stresses $\sim \alpha^2$ in height-evolution equation (2.13). Furthermore, relation (2.22) reveals that the height perturbation Δh scales linearly with the concentration perturbation magnitude $\overline{c_p}$. Therefore, with $\overline{c_p} \ll 1$, a perturbation expansion in powers of $\overline{c_p}$ for both the film height h and solute concentration c may yield useful insight. We expand both unknowns as

$$h = 1 + \overline{c_p}h_1(t,x) + O(\overline{c_p}^2), \quad c = c_b + \overline{c_p}c_1(t,x) + O(\overline{c_p}^2), \tag{2.23}$$

where c_b is the base state indicated in equation (2.20). Because vertical diffusion is rapid, we have assumed that c is uniform in z for simplicity. However, one could

instead employ the rapid-vertical-diffusion approximation proposed by Jensen and Grotberg[13] without affecting the results of this analysis.

Substituting equations (2.23) into equations (2.13) and (2.14) gives the $O(\overline{c_p})$ problem

$$\frac{\partial h_1}{\partial t} = -\frac{1}{3}\frac{\partial^4 h_1}{\partial x^4} + \frac{1}{2}\frac{\partial^2 c_1}{\partial x^2}, \quad \frac{\partial c_1}{\partial t} = \frac{1}{Pe}\frac{\partial^2 c_1}{\partial x^2} \tag{2.24}$$

with initial conditions $h_1 = 0$ and $c_1 = \cos(\alpha x)$. The latter of equations (2.24) has solution

$$c_1 = \cos(\alpha x)\exp\left(-\frac{\alpha^2}{Pe}t\right) \tag{2.25}$$

which shows that c_1 is simply the initial perturbation decaying over time due to lateral diffusion. Substituting this form for c_1 into the former of equations (2.24) gives the fourth-order, linear, inhomogeneous PDE governing h_1:

$$\frac{\partial h_1}{\partial t} = -\frac{1}{3}\frac{\partial^4 h_1}{\partial x^4} - \frac{\alpha^2}{2}\cos(\alpha x)\exp\left(-\frac{\alpha^2}{Pe}t\right). \tag{2.26}$$

Given the nonconstant forcing term in equation (2.26), as well as the eigenfunctions of the fourth-derivative operator, it is sensible to expect the x-dependence of h_1 to be a cosine wave. Thus, we assume $h_1 = \cos(\alpha x)g(t)$ with $g(0) = 0$, and equation (2.26) has solution

$$h_1(t,x) = \frac{\alpha^2/2}{\alpha^4/3 - \alpha^2/Pe}\cos(\alpha x)\left(\exp\left(-\frac{\alpha^4}{3}t\right) - \exp\left(-\frac{\alpha^2}{Pe}t\right)\right). \tag{2.27}$$

The constant coefficient in solution (2.27) is proportional to the magnitude

of Marangoni stresses $\alpha^2/2$ and inversely related to those of capillary flow $\alpha^4/3$ and lateral diffusion α^2/Pe. This agrees with intuition, since stronger Marangoni stresses (larger $\alpha^2/2$) result in larger $g(t)$ and thus larger height perturbations. Similarly, considering also the transient part of equation (2.27) suggests that stronger capillary stresses or faster diffusion result in smaller height perturbations. Summarizing, the expressions for the height h and concentration c to $O(\overline{c_p}^2)$ are

$$c = c_b + \overline{c_p}\cos(\alpha x)\exp\left(-\frac{\alpha^2}{Pe}t\right) + O(\overline{c_p}^2), \tag{2.28}$$

$$h = 1+\overline{c_p}\frac{\alpha^2/2}{\alpha^4/3-\alpha^2/Pe}\cos(\alpha x)\left(\exp\left(-\frac{\alpha^4}{3}t\right)-\exp\left(-\frac{\alpha^2}{Pe}t\right)\right)+O(\overline{c_p}^2), \tag{2.29}$$

which describe the film dynamics in region I of figure 2.5. From these solutions, we can obtain explicit expressions for Δh and t_{max}; the amplitude of h gives the size of the height perturbation over time and exhibits a unique maximum at time

$$t_{max} = \frac{\log(\alpha^4/3)-\log(\alpha^2/Pe)}{\alpha^4/3-\alpha^2/Pe} + O(\overline{c_p}). \tag{2.30}$$

Equation (2.30) is the inverse of the log-mean difference of the magnitudes of capillary stresses $\alpha^4/3$ and lateral diffusion α^2/Pe, where an increase in either results in a decrease in t_{max}. Intuitively, stronger capillary stresses more quickly counteract Marangoni stresses, and stronger lateral diffusion more quickly levels lateral concentration gradients. However, the log-mean difference also suggests a form of nonlinear physical "exchange" (notably arising in heat exchangers).[54] Indeed, faster lateral diffusion leads to smaller capillary stresses because it more

quickly levels concentration gradients. This causes smaller Marangoni stresses and thus smaller height perturbations which create smaller capillary stresses. In contrast, larger capillary stresses more quickly counteract Marangoni stresses and allow less time for lateral diffusion, reducing its importance. Therefore, an increase in either capillary stresses ($\alpha^4/3$) or lateral diffusion (α^2/Pe) reduces the importance of the other. This exchange through the medium of Marangoni stresses is encapsulated in equation (2.30). Capillary stresses, Marangoni stresses, and solute diffusion are interdependent in this manner.

Concluding this analysis, we substitute equation (2.30) for t_{max} into equation (2.29) for h and solve for the amplitude to obtain an explicit expression for the maximum height perturbation Δh:

$$\Delta h = 3\overline{c_p}\alpha^{-2}\exp\left(-\frac{\alpha^2}{Pe}t_{max}\right) + O(\overline{c_p}^2). \tag{2.31}$$

This matches scaling relation (2.22) derived by considering the magnitude of capillary and Marangoni stresses. Equations (2.30) and (2.31) are plotted in region I of figure 2.5 (magenta line) where there is excellent agreement between the two-layer system (red circles), one-layer approximation (blue diamonds), and analytical approximation (magenta line). Therefore, the two-layer system quantitatively behaves as a one-layer film at low Pe (in region I) due to rapid vertical diffusion with dynamics well-described by equations (2.28) and (2.29). Discussion of the dependence on c_p and α is left to §A and §B.

We have established simple mechanisms and analytical expressions for the

trends in both Δh and t_{max} in region I of figure 2.5. Through a one-layer approximation, we established that the two-layer system quantitatively behaves as a one-layer film. Consequently, the maximum film-height perturbation Δh increases with Pe according to equation (2.31) because lateral diffusion slows. Similarly, equation (2.30) shows that t_{max} increases with Pe according the inverse of the log-mean difference of the magnitudes of capillary flow $\alpha^4/3$ and lateral diffusion α^2/Pe.

B Region II - Transition Region

The boundary between region I and region II of figure 2.5 is taken to be the smallest Pe for which Δh for the two-layer system deviates from the one-layer-approximation value by more than 10%. Notably, the one-layer approximation plateaus at $\Delta h \approx 3\overline{c_p}\alpha^{-2}$ (as $Pe \to \infty$ in equation (2.31)) while Δh for the two-layer system continues to increase. While the 10% criterion is arbitrary, it provides a consistent and quantitative distinction between regions I and II. In region II, both the maximum height perturbation Δh and the time to achieve it t_{max} increase monotonically until a critical Péclet number $Pe_{crit} \approx 10^5$ where t_{max} drops precipitously and the system is considered to be in region III. We will see that region II contains the transition from the diffusion-dominated, low-Pe region I to the convection-dominated, high-Pe region III.

As Pe increases and the system enters region II of figure 2.5, deviation from the one-layer approximation suggests that the rapid-vertical-diffusion assumption is failing; vertical diffusion becomes sufficiently slow that vertical solute concen-

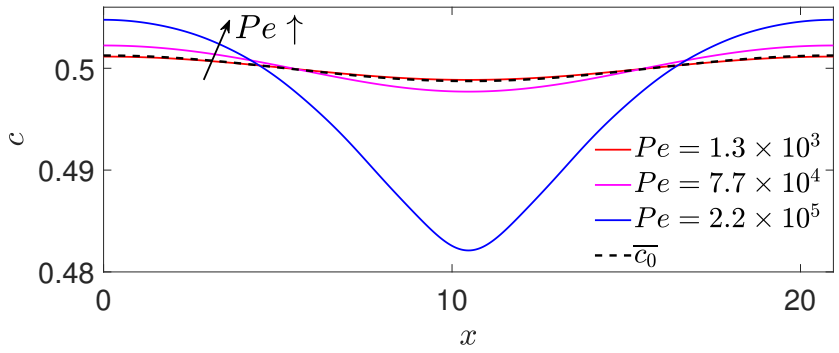

Figure 2.6: Concentration profiles at the interface $z = h$ and $t = t_{max}$ for three different Pe and the vertically-averaged initial condition $\overline{c_0}$ (equation (2.20). Under pure diffusion, $\overline{c_0}$ gives the maximum possible lateral perturbation at the interface. The red line for $Pe = 1.3 \times 10^3$ is data taken from region I of figure 2.5. Similarly, the magenta line for $Pe = 7.7 \times 10^4$ and the blue line for $Pe = 2.2 \times 10^5$ are data taken from regions II and III, respectively, of figure 2.5.

tration gradients begin to influence film evolution. The increase in Δh in region II shows that Marangoni stresses become larger over a relatively small range of Pe (compared to region I). Furthermore, a precipitous drop in t_{max} at $Pe_{crit} \approx 10^5$ indicates a significant shift in the evolution dynamics. To uncover the role of vertical gradients in these phenomena, we examine the solute concentration profiles that drive film-height deformation. Figure 2.6 shows concentration profiles evaluated at the interface $z = h$ at $t = t_{max}$ for three different Pe as well as the vertically-averaged initial condition $\overline{c_0}$ defined by equation (2.20). Examining these profiles, we see that the concentration perturbation at the interface drastically increases in magnitude as Pe increases.

As discussed in §A, vertical diffusion is laterally nonuniform and causes lateral concentration gradients to develop at the interface. Starting from initial condition c_0 (equation (2.17)), vertical diffusion brings the system to a vertically uniform state that coincides with its vertical average, $\overline{c_0}$ (equation (2.20)). Thus, $\overline{c_0}$ gives

the largest lateral gradient that will develop at the interface solely from nonuniform vertical diffusion and is plotted in figure 2.6 (dashed black line). The lateral perturbation in $\overline{c_0}$ gives a limiting value for Marangoni stresses in the one-layer approximation used for region I of figure 2.5, resulting in the plateau $\Delta h \approx 3\overline{c_p}\alpha^{-2}$ (as $Pe \to \infty$ in equation (2.31)). Indeed, for $Pe = 1.3 \times 10^3$ (red line), which is in region I, figure 2.6 shows that the concentration profile has not exceeded this limit. However, for $Pe = 7.7 \times 10^4$ (magenta line), which is in region II, figure 2.6 shows that the concentration perturbation exceeds the diffusion-dominated profile $\overline{c_0}$. Furthermore, for $Pe = 2.2 \times 10^5$ (blue line), which is in region III, figure 2.6 shows that the concentration profile significantly deviates from the diffusion-dominated profile $\overline{c_0}$ with a notably deep trough. The sharpening of concentration gradients for larger Pe shows that we have departed from the one-layer approximation and thus diffusion cannot be the mechanism that is sharpening gradients. Therefore, it must be that convection is sharpening gradients since it is the only other process through which solute is transported in the film.

To understand the role of solute convection, we examine the liquid velocity profiles. Figure 2.7 shows velocity profiles (black arrows) plotted over solute concentration contours at two different times. At early times (figure 2.7 (a)), Marangoni stresses drive flow from the troughs (edges) to the crest (center) resulting in a lateral velocity v_x that is positive on the left ($x < \pi/\alpha$) and negative on the right ($x > \pi/\alpha$). The corresponding vertical velocity v_z is positive in the center ($|x - \pi/\alpha| < \pi/2\alpha$) and negative on the edges. Note that the velocities do not change sign through the film depth. At later times, the film has deformed

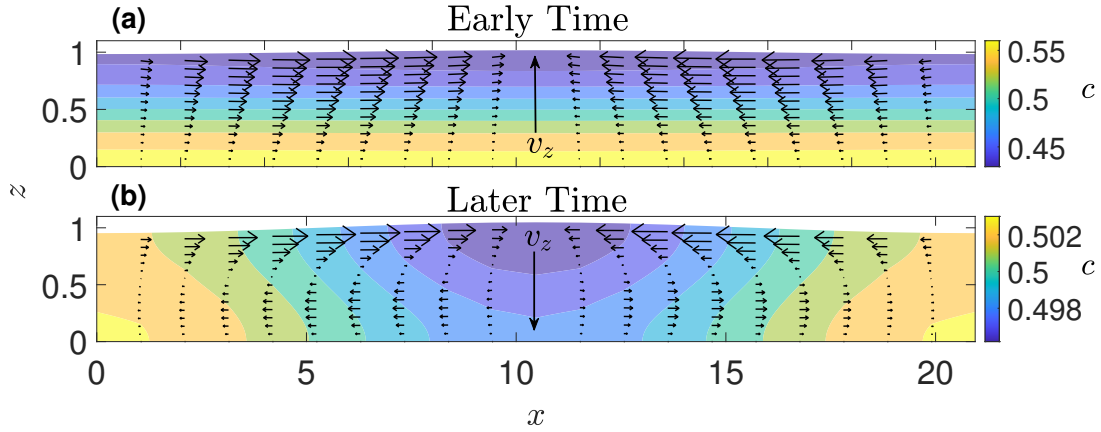

Figure 2.7: Velocity contours (black arrows) plotted over solute concentration contours (a) before ($t \approx 2.23 \times 10^2$) and (b) after ($t \approx 6.85 \times 10^2$) the development of circulatory flow for $Pe = 10^5$. The vertical velocity v_z is generally an order of magnitude smaller than the horizontal velocity v_x and is difficult to discern. As a visual aid, the arrows labeled "v_z" indicate the direction of the vertical velocity at the center of the film ($x = \pi/\alpha$) but are not to scale. At early times, there is bulk flow from the troughs to the crest. Later, circulatory flow develops while the troughs and crest continue to grow.

appreciably ($\approx 10\%$ of the film thickness) and capillary stresses become significant. Figure 2.7 (b) shows that the velocity profiles become circulatory with v_x now changing sign about halfway through the film depth. However, the vertical velocity does not change sign through the film depth, and is now negative in the center and positive on the edges. These velocity profiles are reminiscent of cellular structures observed in previous work,[27–30] and while a few of these works studied thermal Marangoni flow, analogous phenomena are seen in solutal Marangoni flow. However, we observe unique phenomena due to large vertical concentration gradients from the two-layer geometry.

Due to large vertical concentration gradients, vertical convection can move a significant quantity of solute to or from the interface $z = h$. Keeping in mind that vertical concentration gradients are negative ($\partial c/\partial z < 0$), figure 2.7 (a) shows

that, at early times, vertical convection increases the solute concentration at the crest (center where $v_z > 0$) and decreases it at the troughs (edges where $v_z < 0$). This effectively counteracts the imposed perturbation which is a depletion of solute in the center (equation (2.17)). However, at later times shown in figure 2.7 (b), vertical convection acts to increase concentration at the troughs (where $v_z > 0$) and decrease it at the crest (where $v_z < 0$). This steepens the imposed concentration perturbation, causing larger Marangoni stresses and thus larger height perturbations. Convective steepening of lateral concentration gradients causes the sharpening of the concentration profiles shown in figure 2.6 and thus the deviation from the one-layer approximation in figure 2.5 as Pe increases. Large vertical concentration gradients are critical to this phenomenon, since the regions of high concentration near $z = 0$ in figure 2.7 are convected up to the interface $z = h$ by the vertical velocity v_z.

The steepening of lateral concentration gradients from vertical convection is not unique to this system; it can be observed in an analytical solution for solute undergoing pure convection from a laterally-uniform initial condition:

$$\frac{\partial c}{\partial t} + u_x(x,z)\frac{\partial c}{\partial x} + u_z(x,z)\frac{\partial c}{\partial z} = 0, \qquad c_0^*(z) = T\left(z;\, h_b = 1/2, s = 3\right). \tag{2.32}$$

The laterally uniform initial condition c_0^* is analogous to c_0 given by equation (2.17), except that it lacks a lateral perturbation. The velocities, u_x and u_z, are

chosen to approximate those shown in figure 2.7 (b) with

$$u_x(x,z) = u_m z \sin(x), \quad u_z(x,z) = \frac{u_m}{2} z^2 \cos(x). \tag{2.33}$$

Here, u_x does not change sign through the film depth, which misses the recirculation shown in figure 2.7, and the approximation (2.33) does not conserve mass. However, the important phenomenon is vertical convection and the approximation u_z is qualitatively correct with $u_z < 0$ near the center ($x = \pi$) and $u_z > 0$ near the edges. The parameter u_m controls the maximum value of the velocity, which we take as $u_m = 9 \times 10^{-4}$ to approximate values observed in the numerical model.

On the constant domain $x \in (0, \pi)$ and $z \in (0, \infty)$, we solve equation (2.32) by the method of characteristics to obtain

$$z(t) = z_0 \sqrt{\frac{\sin(x(t))}{\sin(x_0)}}, \qquad x(t) = f^{-1}\left(f(x_0) + u_m \frac{z_0}{\sqrt{\sin(x_0)}} t \right). \tag{2.34}$$

The function f, along with a full derivation of these characteristics, is provided in the appendix. These characteristics are numerically inverted to obtain values for $z_0(t, x, z)$ with which the solution to equation (2.32) is

$$c(t,x,z) = c_0^*(z_0(t,x,z)). \tag{2.35}$$

Solution (2.35) is plotted for $z = 1$ as a function of x and three different times in figure 2.8. Although the initial profile c_0^* (equation (2.32)) is laterally uniform, the x-dependence of the vertical velocity u_z (equation (2.33)) couples with vertical

concentration gradients to create lateral concentration gradients.

The velocities shown in figure 2.7 (b) that are approximated by equations (2.33) require that the interface has deformed appreciably so that capillary stresses are significant. Recalling there is initially no solute at the interface (see figure 2.3), some degree of vertical diffusion must have already occurred to develop lateral concentration gradients and Marangoni stresses that deform the interface. As Pe increases and vertical diffusion slows, larger vertical concentration gradients are present in the system at any given time, and particularly when the liquid velocities become circulatory as shown in figure 2.7 (b). Thus, vertical convection will more rapidly steepen lateral concentration gradients resulting in the increasing Δh we observe in region II of figure 2.5 (a). One can observe how rapid convective steepening is in the analytical example plotted in figure 2.8, where concentration gradients that are orders of magnitude larger than those shown in figure 2.6 have developed on time scales similar to values observed for t_{max} in figure 2.5 (b). Once Pe is large enough that the lateral gradients rapidly created by convective steepening significantly exceed those from nonuniform vertical diffusion, we observe the precipitous drop in t_{max} at $Pe_{crit} \approx 10^5$. Beyond this drop, convective steepening is the dominant mechanism causing film-height deformation. Thus, region II represents the transition from the diffusion-dominated region I to the convection-dominated region III.

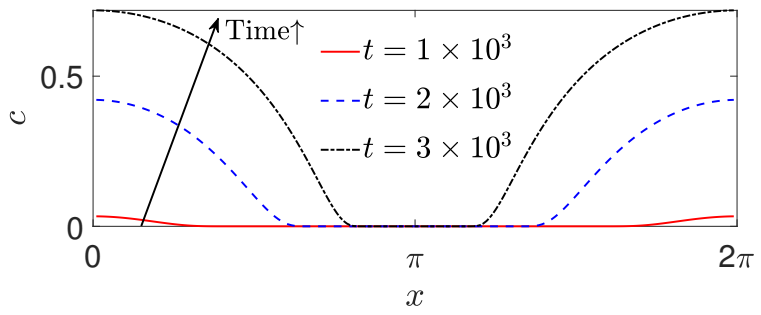

Figure 2.8: Solution (2.35) of convection equation (2.32) evaluated at $z = 1$ and three different times. Laterally nonuniform vertical convection causes the rapid formation of a laterally nonuniform concentration profile, even though the initial condition is laterally uniform with $c_0^*(z = 1) = 0$.

C Region III - Convective Steepening

In region III of figure 2.5, convective steepening of lateral concentration gradients is the primary mechanism for film-height deformation as discussed in §B. Throughout region III of figure 2.5, the vertical diffusion time scale $\epsilon^2 Pe$ is comparable to, or greater than, the deformation time t_{max}, so significant vertical gradients are present for all times $t \leq t_{max}$. Therefore, convective steepening creates increasingly large and sharp lateral concentration gradients as shown by the profile at $Pe = 2.2 \times 10^5$ in figure 2.6 (blue line). The increase in the height perturbation Δh in region III of figure 2.5 accelerates as Pe increases because of these increasingly sharp concentration gradients.

After the initial precipitous drop at $Pe_{crit} \approx 10^5$ in figure 2.5, t_{max} begins to increase. This is partially due to increasing vertical diffusion times, that scale as $\epsilon^2 Pe$, since there is an initial diffusion time required to develop a lateral gradient at the interface. However, this is not the scaling we observe in region III of figure 2.5 (b) (a linear fit gives a power-law exponent $\approx .74$) because there is an additional

contribution from capillary stresses. As was discussed in §A and demonstrated in equation (2.30), larger height perturbations create larger capillary stresses that inhibit growth and increase t_{max}. Coupled with longer vertical diffusion times, this gives the increase in t_{max} we see in figure 2.5 (b). Note that equation (2.30) was derived for region I and thus does not predict t_{max} in regions II or III. However, the physical mechanisms of capillary flow and diffusion that it embodies are present in all regions.

With an understanding of all three regions of figure 2.5, it is worthwhile to discuss their relation to an actual coating process. Films are solidified for many applications, so there is a solidification time t_{solid} that may be from evaporation, curing, or other methods. (Note that solidification is not considered in this work and could introduce additional phenomena, e.g., film deformation due to development of stresses in the solid.) In the solidified film, it is likely desirable that the two layers remain uniform and distinct to impart different functionality to each layer.[12,55] Thus, solidification should be more rapid than vertical diffusion and the formation of nonuniformities ($t_{solid} \ll \epsilon^2 Pe$ and $t_{solid} \ll t_{max}$). Figure 2.9 shows schematics of possible solidified film geometries for values of Pe in the three regions of 2.5. Despite small height perturbations, it is unlikely that region I is favorable because any distinction between layers is quickly erased by diffusion, resulting in one uniform layer as shown in figure 2.9 (a); the restriction $t_{solid} \ll \epsilon^2 Pe$ requires extremely rapid solidification that could introduce additional instabilities.[27] Thus, region II or III is more desirable because slower diffusion allows one to achieve stratified layers as depicted in figures 2.9 (b) and

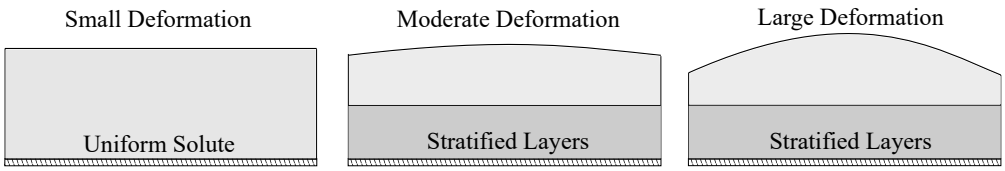

Figure 2.9: Schematics depicting possible geometries of a solidified film for values of the Péclet number Pe in (a) region I, (b) region II, and (c) region III of figure 2.5.

(c). However, film-height nonuniformities are significantly larger in region III than those in regions I and II due to convective steepening. Furthermore, t_{max} drops precipitously at Pe_{crit} as shown in figure 2.5 (b), so the restriction $t_{solid} \ll t_{max}$ is more difficult to achieve in region III. Therefore, region II may be the optimal region for a two-layer coating process, since height perturbations are small relative to region III (see figure 2.5 (a)) and Pe and t_{max} are large enough that the restrictions $t_{solid} \ll \epsilon^2 Pe$ and $t_{solid} \ll t_{max}$ are not too strict.

IV Effects of System Parameters

In this section we conduct a parametric study to understand the influence of system parameters on film evolution. In a two-layer coating, there are a number of physical parameters that affect film dynamics. Physical properties of the liquid are encapsulated in the two dimensionless groups Pe and Ma. The dependence on the Péclet number Pe was explored in §III, and the dependence on the Marangoni number Ma will be investigated in §D. The system geometry is controlled by the dimensionless bottom-layer thickness h_b and is explored in §C. The two parameters that control the perturbation imposed in initial condition (2.17) are the magnitude c_p and wavenumber α, investigated in §A and §B respectively. The remaining

parameters, $s = 3$ and $\upsilon = 0.1$, are fixed as discussed in §B.

A Perturbation Magnitude

The perturbation magnitude c_p controls the magnitude of the imposed lateral perturbation in initial condition (2.17). While difficult to control in a coating process, it is important to understand how the size of perturbations affects film stability. In §III, the perturbation magnitude was taken to be $c_p = 10^{-2}$ which is 1% of the base-state concentration. While numerical limitations (due to steep concentration gradients) prevent us from generating meaningful data at larger c_p, we can uncover the basic trends by examining film evolution at smaller c_p. Results for $c_p = 10^{-2}$ are given again in figures 2.10 (a) and (b) along with results using two smaller values, $c_p = 10^{-3}$ and $c_p = 10^{-4}$. Figure 2.10 (a) shows that the magnitude of the height perturbation Δh increases monotonically as c_p increases. In contrast, figure 2.10 shows that, remarkably, the t_{max} for all three values of c_p are visually indistinguishable, suggesting that the size of the initial concentration perturbation does not appreciably affect the time scales for film evolution.

To understand this behavior, we return to equations (2.30) and (2.31). In region I (rapid vertical diffusion; see §A), equation (2.31) reveals that the maximum height perturbation Δh scales linearly with the initial concentration perturbation c_p, while equation (2.30) shows that t_{max} is independent of c_p. Linear fits of Δh at each Pe show a linear scaling with c_p for all Pe investigated in this work. Selected values of Pe are shown in figure 2.10 (c), where the largest value is taken in region III. Remarkably, we see the linear scaling with c_p that was derived for

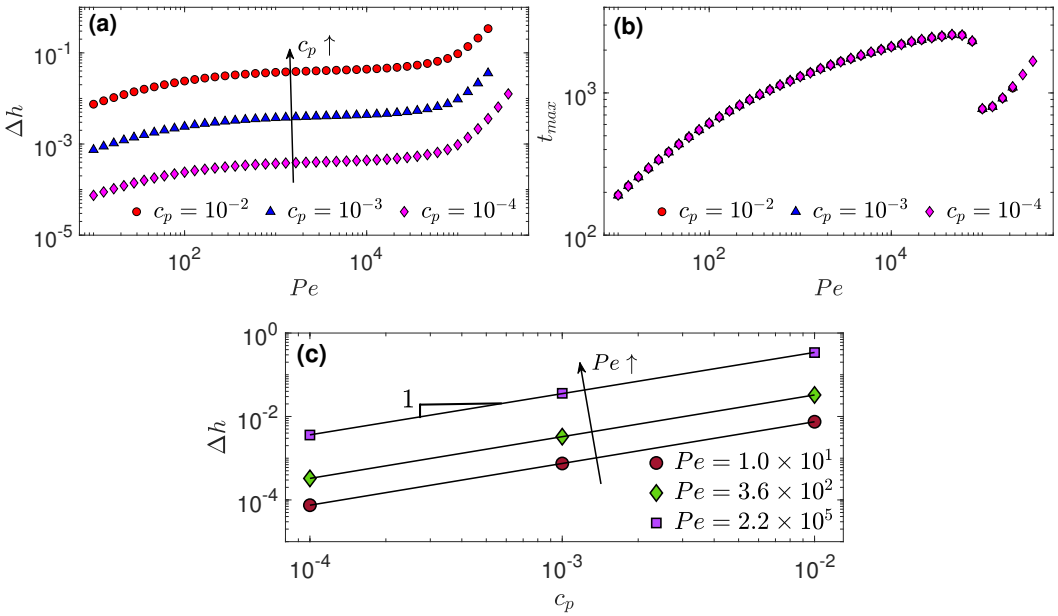

Figure 2.10: (a) The maximum height perturbation Δh and (b) the time to achieve it t_{max} at varying Pe and three perturbation magnitudes c_p. There are only quantitative shifts in Δh, and the values of t_{max} are nearly identical for all three values of c_p. (c) Linear fits of the maximum height perturbation Δh versus perturbation magnitude c_p at three different Pe. All lines have a slope of approximately unity, indicating a linear scaling with c_p. The largest value of $Pe = 2.2 \times 10^5$ is taken from region III where an analytical scaling relation has not been derived.

region I holds through regions II and III, suggesting that the lateral concentration gradients that result from convective steepening (see §B) scale linearly with c_p. Furthermore, figure 2.10 (b) shows that t_{max} is independent of c_p for all regions, even though equation (2.30) only holds in region I. We note that we were unable to obtain analytical relations for regions II and III due to the complexity of convective steepening of concentration gradients. Nevertheless, figure 2.10 shows that while the maximum deformation achieved Δh scales linearly with the perturbation magnitude c_p, so does the rate at which the film deforms, resulting in a deformation time t_{max} that is effectively independent of c_p for all Pe investigated in this work.

This analysis has revealed that the perturbation magnitude c_p has a direct effect on film stability. If a coating process tends to introduce larger perturbations into a coated film, the resulting film-height nonuniformities will be larger, scaling linearly with the perturbation magnitude c_p. Furthermore, even though the maximum film-height nonuniformities are larger, the times to achieve them are unchanged; this is a surprising result that can understood from the analysis in §A. Larger height perturbations bring the film to a more nonuniform state, and thus larger c_p is destabilizing. One should strive to minimize the magnitude of lateral concentration perturbations in two-layer coatings for optimal uniformity.

B Perturbation Wavenumber

The perturbation wavenumber α controls the period of the imposed lateral perturbation in initial condition (2.17). Due to periodicity, the dimensionless lateral domain is $x \in (0, 2\pi/\alpha)$, and thus α controls the dimensionless lateral length scale $2\pi/\alpha$. There are numerous lateral derivatives that appear in equations (2.13) and (2.14), so the effect of varying α is difficult to predict *a priori*. As shown in figures 2.11 (a) and (b), varying α has a pronounced effect on both the maximum height perturbation Δh and the time to achieve it t_{max}.

In region I (rapid vertical diffusion; see §A), the decrease in Δh and t_{max} with increasing α is quantitatively predicted by equations (2.30) and (2.31). Equation (2.31) may be rewritten in the form

$$\log \alpha^2 \Delta h \sim -\frac{\alpha^2 t_{max}}{Pe}. \tag{2.36}$$

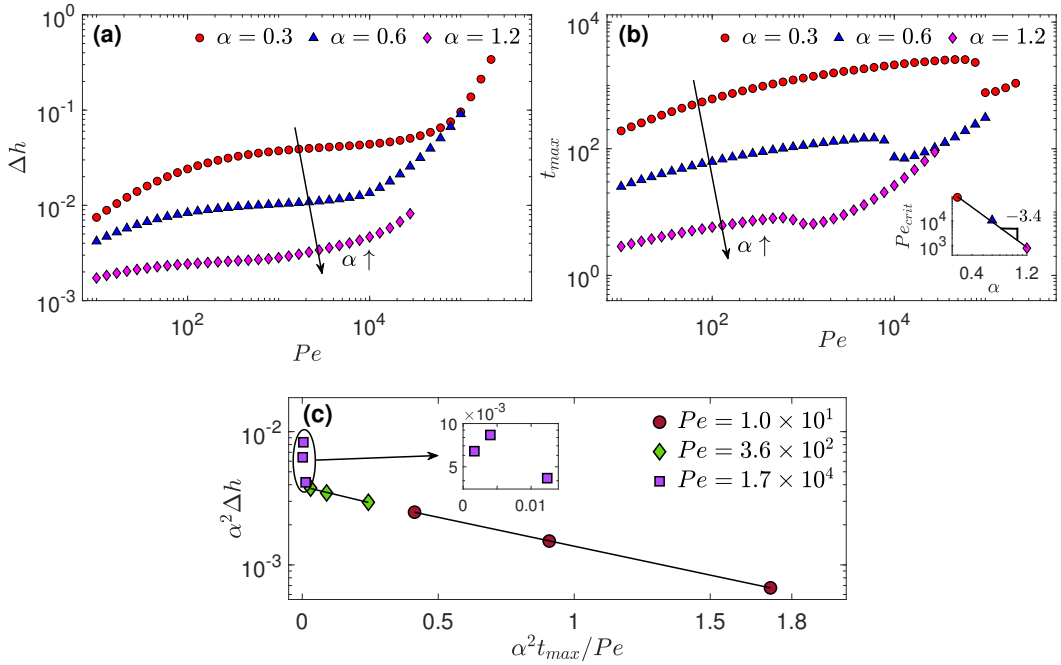

Figure 2.11: (a) The maximum height perturbation Δh and (b) the time to achieve it t_{max} at different Pe and three perturbation wavenumbers α. (c) Linear fits of the scaled height perturbation $\alpha^2 \Delta h$ versus the scaled time $\alpha^2 t_{max}/Pe$. Data points for $Pe = 1.7 \times 10^4$ in regions II and III are repeated in the zoomed-in subplot to illustrate that the scaling relation does not hold outside of region I.

Linear fits of the data from figures 2.11 (a) and (b) for three different Pe are shown in figure 2.11 (c) where we see that equation (2.36) captures the trends in Δh and t_{max} as α varies in region I (red circles and green diamonds) but not in regions II and III (purple squares) where convective steepening becomes important. As α is increased in region I, lateral diffusion more quickly levels the higher-wavenumber concentration gradients resulting in reduced Marangoni stresses. Furthermore, higher wavenumber disturbances result in a larger interfacial curvature and thus stronger capillary stresses which more quickly counteract Marangoni stresses. Together, these effects result in the decrease of Δh and t_{max} in region I of figures 2.10 (a) and (b) that is described by equations (2.30) and (2.31). The evolution is more complicated in regions II and III, however, where we see non-monotonic trends

arising in both Δh and t_{max} at large Pe. To understand this, we first investigate the dependence of Pe_{crit} on α and then establish a qualitative understanding of the trends in regions II and III.

In figure 2.11 (b), we observe that Pe_{crit} (at which t_{max} drops) decreases as α increases. As discussed in §B, the drop in t_{max} at Pe_{crit} occurs when vertical diffusion is sufficiently slow that convective steepening is the dominant mechanism creating lateral concentration gradients at the interface. Considering the center of the film where $v_x = 0$ ($x = \pi/\alpha$ in figure 2.7), we can isolate relevant terms in equation (2.14):

$$v_z \frac{\partial c}{\partial z} \sim \frac{1}{\epsilon^2 Pe_{crit}} \frac{\partial^2 c}{\partial z^2}. \tag{2.37}$$

To back out a useful relation from equation (2.37), we assume that vertical derivatives are independent of α because α does not affect the vertical length scale. We then rewrite equation (2.11) as

$$v_z = \underbrace{\frac{1}{6}\left(\eta^3 - 3\eta^2\right) \frac{\partial}{\partial \zeta}\left[h^3 \frac{\partial^3 h}{\partial \zeta^3}\right]}_{\text{Capillary Flow}} + \underbrace{\frac{1}{2}\eta^2 \frac{\partial}{\partial \zeta}\left[h^2 \left.\frac{\partial c}{\partial \zeta}\right|_{z=1}\right]}_{\text{Marangoni Flow}} + \eta \frac{\partial h}{\partial \zeta} v_x. \tag{2.38}$$

Recalling that $v_x = 0$ in the center of the film, v_z (equation (2.38)) has clear contributions from capillary flow and Marangoni flow. The contribution from capillary flow is negative due to the crest in the film height, while the contribution from Marangoni flow is positive because the solute concentration is minimum in the center of the film. Figure 2.7 (b) shows that $v_z < 0$ in the center of the film at later times, so capillary flow must be dominant. Furthermore, the capillary-flow

term term scales as α^4, and thus $v_z \sim \alpha^4$. Inserting this into relation (2.37) reveals

$$Pe_{crit} \sim \epsilon^{-2}\alpha^{-4}. \tag{2.39}$$

This approximates the relation shown in a subplot in figure 2.11 (b), where linear regression reveals the scaling $Pe_{crit} \sim \alpha^{-3.4}$. The discrepancy in the power-law exponent of relation (2.39) is likely due to the assumption that the vertical derivatives are independent of α; the relation $v_z \sim \alpha^4$ requires that the qualitative shift in the velocities shown in figure 2.7 has occurred, which in turn requires that some time has passed. This time is tied to the growth of the height disturbance, which must become sufficiently large so that capillary flow overcomes Marangoni flow in equation (2.38). Over this time, which is dependent on α, vertical gradients will relax through diffusion. Thus, the size of vertical gradients depends on α in a way that is difficult to capture through scaling relations. However, the data in figure 2.11 (b) shows that this dependence is somewhat weak, resulting in the small discrepancy in the exponents of the predicted scaling $Pe_{crit} \sim \alpha^{-4}$ and observed scaling $Pe_{crit} \sim \alpha^{-3.4}$ for the range of α investigated here.

Now, we examine the trends in region II (transition between regions I and III; see §B) and region III (after the drop in t_{max}; see §C) of figures 2.11 (a) and (b). The increase in Δh with Pe is monotonic, with Δh steeply increasing at lower Pe as α is increased. This is due to an earlier transition into region III described by relation (2.39) - in this region, convection is stronger and thus more rapidly steepens concentration gradients. These steepened gradients result

in larger Marangoni stresses and thus larger Δh. This is especially pronounced at $Pe = 10^5$, where Δh for $\alpha = 0.6$ (blue triangle) has begun to exceed that for $\alpha = 0.3$ (red circle). Thus, the trend in Δh with α is not necessarily monotonic at large Pe due to the complexity of convective steepening.

The accompanying trend in Δt can be understood with similar reasoning, where faster diffusion and stronger capillary stresses at larger α reduce t_{max} according to equation (2.30). The quantity t_{max} more rapidly increases at larger α due to capillary stresses in equation (2.13) which scale as $\alpha^4 \Delta h$. Because the size of the height perturbation Δh rapidly increases with Pe (as shown in figure 2.11 (a)), the damping of growth rates ($\partial h / \partial t$) by capillary stresses also rapidly increases with Pe. Furthermore, this damping scales as α^4, and is thus even more pronounced at larger α. These effects becomes so prominent that the trend in t_{max} with α is not necessarily monotonic at large Pe, with t_{max} in figure 2.11 (b) at $Pe = 2.8 \times 10^4$ being nearly equal for $\alpha = 0.6$ (blue triangle) and $\alpha = 1.2$ (magenta diamond).

This analysis has shown that the effect of α on film stability is complex. In region I where Pe is small, we see that an increase in α decreases both Δh and t_{max} according to equations (2.30) and (2.31). While a decrease in Δh is stabilizing, a decrease in t_{max} is destabilizing. Furthermore, the situation is more complicated at large Pe where we find that the trend in both Δh and t_{max} is not monotonic with α. The role of perturbation wavelengths in film stability is thus strongly dependent on the value of the Péclet number Pe. In a physical coating process, small, effectively

random perturbations result in a distribution of wavenumbers where the width of the coated film controls smallest wavenumber α that can be expressed in the perturbation. A smaller coated width will generally result in larger wavenumbers giving larger height deformations Δh as well as larger deformation times t_{max}. However, at very large Pe, these relationships may reverse, with an increase in α giving a decrease in Δh or t_{max} depending on the value of Pe. One must thus be cognizant of the value of the Péclet number when considering the effects of film width and perturbation wavenumbers on film stability.

C Layer Thickness

Initial condition (2.17) approximates the conditions studied by Horiuchi et al.[12] as a binary miscible two-layer film with a diffuse boundary between layers. The parameter h_b gives an effective bottom-layer thickness and is an important parameter in two-layer coating that influences many aspects of the coating process.[12,56] Here we focus on how h_b influences the maximum height perturbation Δh and the time to achieve it t_{max}; values of Δh and t_{max} at three different bottom-layer thicknesses h_b are given in figure 2.12. Notably, both Δh and t_{max} at different h_b are indistinguishable in region I, but begin to diverge from each other slightly in region II and noticeably in region III (see §III for a discussion of each region).

The lack of dependence on h_b in region I is due to the form of initial condition (2.17), where the perturbation is localized to the diffuse region between layers. Marangoni flow is the result of concentration gradients, so it is not affected by the base state value c_b in equation (2.20). Furthermore, the Gaussian in the

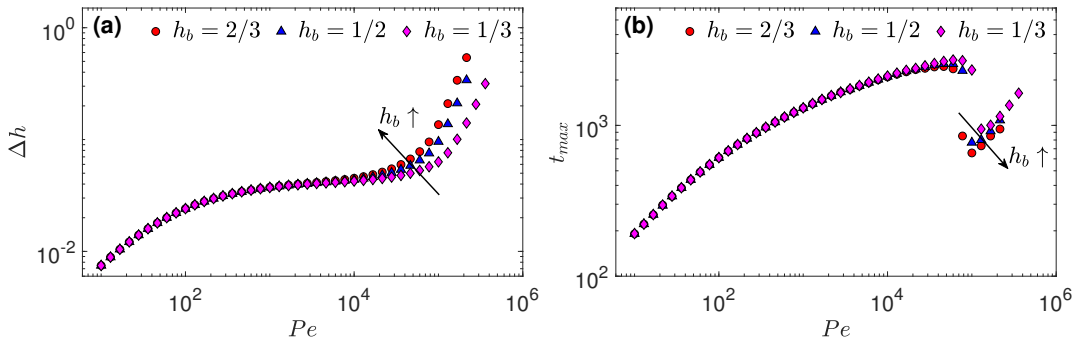

Figure 2.12: Plots of (a) the maximum height perturbation Δh and (b) the time to achieve it t_{max} at different Pe and three layer thicknesses h_b. There are only small quantitative shifts in both Δh and t_{max}.

perturbation magnitude $\overline{c_p}$ integrand decays sufficiently fast that the integrand is near zero outside of the diffuse region. The diffuse region has radius $1/s$, so with $\upsilon = 0.1$ and $s = 3$ we have $1/s \approx 3\upsilon$; approximately 99.8% of the Gaussian distribution lies within three standard deviations of the mean, so the perturbation magnitude integrand in equation (2.20) decays to essentially zero outside of the diffuse region. It is thus expected that h_b has no appreciable effect on region I of figure 2.12 because it has a negligible effect on the perturbation magnitude. While this may seem to be an artifact of the form chosen for c_0, it is actually a decoupling of the parameters h_b and c_p that aids this parametric study.

As Pe increases into regions II and III, the convective steepening mechanism described in §B become important and a dependence on h_b emerges. Steepening of lateral concentration gradients requires vertical concentration gradients that can be nonuniformly convected to the interface $z = h$. The largest vertical gradients are precisely at $z = h_b$, so decreasing h_b moves the largest vertical gradients farther from the interface and closer to the substrate where vertical convection is weaker due to the no-penetration condition. Thus, convective steepening is weaker and

steepens lateral concentration gradients less. This is reflected in figure 2.12 where we see Δh for $h_b = 1/3$ (magenta diamonds) falls below $h_b = 1/2$ (blue triangles), which in turn falls below $h_b = 2/3$ (red circles). However, t_{max} shows the opposite ordering in region III, because a smaller bottom layer necessitates more time for vertical concentration gradients to be nonuniformly convected up to the interface.

It is clear that decreasing the bottom-layer thickness h_b has a stabilizing effect on the film. While changing h_b has little effect in region I, there is a noticeable effect in region III. When h_b is reduced, the maximum height perturbation Δh decreases and the time to achieve it t_{max} increases. Both of these effects are stabilizing, so reducing the bottom layer thickness h_b has a small but stabilizing effect. This stabilizing effect is primarily due to vertical concentration gradients being positioned farther from the interface and closer to the substrate where convection is weaker. If the perturbation in initial condition (2.17) was not localized to the diffuse region between layers, decreasing h_b would also reduce the averaged perturbation magnitude $\overline{c_p}$ (equation (2.20)) because it reduces the amount of perturbed liquid. One may return to the analyses in §A and §A to see that decreasing the perturbation magnitude results in smaller Δh.

While there are a number of differences between the model developed in this work and the experiments of Horiuchi et al.,[12] we can make some qualitative comparisons. Horiuchi et al.[12] found that decreasing the bottom layer thickness of their films inhibited dewetting. In this work, we have found a similar trend, where decreasing h_b improves film stability by reducing the film-height perturba-

tion Δh and increasing the time to achieve it t_{max}. Our work thus suggests that the improved stability observed by Horiuchi et al.[12] may be caused by vertical concentration gradients being positioned farther from the liquid-air interface.

D Marangoni Number

The Marangoni number $Ma = \epsilon^2$ gives the ratio of Marangoni forces to capillary forces. While this quantity is crucial to the scaling of physical variables used in equations (2.2) and defines the lateral length scale $L = H/\sqrt{Ma}$, it only appears once in the final governing equations as the lumped parameter $\epsilon^2 Pe$ in equation (2.14). This controls the vertical diffusion time scale, and thus reducing Ma has the sole effect of reducing the vertical diffusion time. Figure 2.13 shows results for Δh and t_{max} for three different $\epsilon = \sqrt{Ma}$ and varying Pe. We see that at $\epsilon = 10^{-2}$ the film remains in region I and II until $Pe_{crit} \approx 10^7$, whereas for $\epsilon = 10^{-1}$ the transition occurs at $Pe_{crit} \approx 10^5$. Recalling scaling relation (2.39) that predicts $Pe_{crit} \sim \epsilon^{-2}$, this is precisely the trend we see in figure 2.13 (b) where an inset plot shows a linear fit of Pe_{crit} to ϵ. Because reducing Ma simply reduces the vertical diffusion time scale, a larger Pe is required for vertical diffusion to be sufficiently slow for the convective steepening mechanism discussed in §B to become important.

Caution should be taken in interpreting these results from a stability standpoint. Decreasing Ma has the direct effect of decreasing Pe_{crit}, which may be considered destabilizing since convective steepening becomes significant at lower Pe. In addition, the parameter $\epsilon = \sqrt{Ma}$ appears numerous times in physical

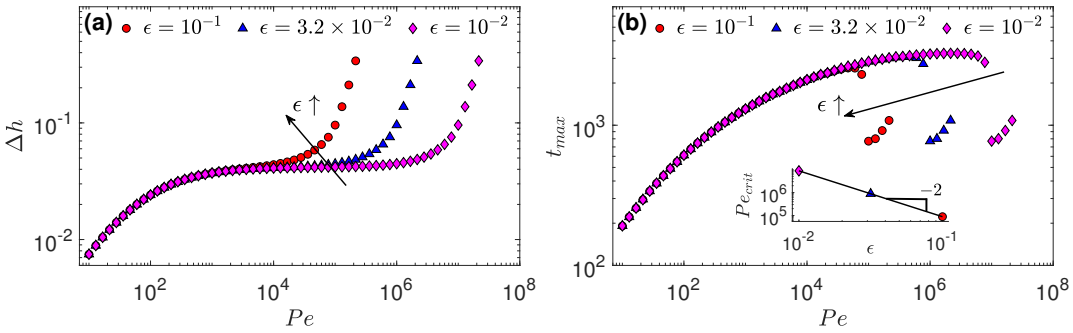

Figure 2.13: Plots of (a) the maximum height perturbation and (b) the time to achieve it at varying Péclet number Pe and three different Marangoni numbers $Ma = \epsilon^2$. There are only quantitative shifts in where region transitions occur. The inset plot in (b) shows the scaling $Pe_{crit} \sim \epsilon^{-2}$.

scales (2.2), and namely in the time scale $t^* = H/v_x^*\epsilon \sim \epsilon^{-4}$. Therefore, decreasing ϵ increases the physical time scale, so while the dimensionless times presented in figure 2.13 may be similar, the corresponding dimensional times are not. Namely, t_{max} for smaller Ma are actually larger and thus, coupled with the shift in Pe_{crit}, decreasing Ma is stabilizing. This is perhaps unsurprising, since smaller Ma indicates weaker Marangoni forces which should be stabilizing. Therefore, multilayer coatings comprised of liquids with similar surface tensions will exhibit smaller film-height nonuniformities than those comprised of liquids with significantly different surface tensions.

We again compare our results to those reported by Horiuchi et al.,[12] where it was found that decreasing the Marangoni number Ma inhibited dewetting. We have found a similar trend, where decreasing $\epsilon = \sqrt{Ma}$ improves film stability by shifting Pe_{crit} to higher values. Thus, our model suggests that the improved stability observed by Horiuchi et al.[12] may be due to a transition into a more stable region (e.g., region III to region II) with smaller film-height perturbations

Δh as Pe_{crit} increases.

V Conclusions

In this work, we characterized the evolution of film-height nonuniformities in non-volatile miscible two-layer binary films. From momentum and mass conservation, we derived a set of evolution equations that predict the time evolution of film height and solute concentration. These equations assume the liquid has constant viscosity and density, that the solute is sufficiently dilute ($\omega_0 \ll 1$), and that the Marangoni number is sufficiently small. Because the liquid layers are miscible, there is no liquid-liquid interface and the two-layer system is captured through an initial condition for the concentration that changes value sharply between layers.

Rather than attempting a quantitative comparison with the motivating experiments of Horiuchi et al.,[12] we developed fundamental understanding of the mechanisms that generate film-height nonuniformities in two-layer miscible films. Capturing the effects of large vertical concentration gradients absent in previous work, we found that a disparity in initial solute concentration between the film layers drives flows that lead to significant film-height nonuniformities. Subsequently, through a parametric study, we examined how system parameters influence this behavior and developed scaling relations that shed light on the physical mechanisms underlying the observations of Horiuchi et al.[12]

It was found that three distinct parameter regimes arise when the Péclet number Pe is varied. In region I where Pe is small, vertical diffusion is rapid and the

evolution of the two-layer film is quantitatively that of a one-layer film. Using this fact, analytical relations were derived that predict the evolution of film height nonuniformities in region I. In region II at moderate Pe, diffusion time scales are sufficiently large that circulatory velocities, reminiscent of those observed in previous work,[27–30] cause a rapid steepening of lateral concentration gradients. This phenomenon is unique to the two-layer system, as it is not observed in region I (one-layer films). Finally, in region III at large Pe, convective steepening only becomes more pronounced as diffusion slows and leads to significant film-height nonuniformities. It was determined that region II is likely the optimal region for a two-layer coating process, since height perturbations are small and develop slowly and vertical diffusion is slow enough that solidification need not be too rapid to retain stratified layers.

With an understanding of the dependence on Pe, a parametric study was conducted for the remaining system parameters. It was found that the magnitude of the initial concentration perturbation c_p has a direct effect on film stability; a larger perturbation results in larger film-height nonuniformities and thus a less stable film. The effect of the perturbation wavenumber α is complex since intricate dependencies between capillary and Marangoni stresses lead to trends that are strongly dependent on the value of Pe. It was then found that decreasing the bottom layer thickness h_b has a stabilizing effect because it hinders convective steepening of the concentration profiles. Finally, it was found that the Marangoni number $Ma = \epsilon^2$ directly controls the critical Péclet number Pe_{crit} at which the system transitions into region III. Furthermore, decreasing Ma has a stabilizing

effect on the film, increasing Pe_{crit} and the times required to develop film-height nonuniformities. Predictions of the model appear to be in qualitative agreement with the experiments of Horiuchi et al.[12]

There are several promising extensions of this work. First, it is possible that the solute and solvent have widely separated viscosities.[12] Concentration gradients will then lead to significant viscosity gradients, the effects of which are difficult to predict and warrant a numerical investigation.[4,31,57] Second, in deriving the mathematical model, we neglected the influence of evaporation and thermal Marangoni flows. However, evaporation has been shown to have a wide range of effects on film dynamics.[27,33,34] Extending the model to drying films is a necessary extension of this work because industrial coatings often undergo drying. Drying films also often contain polymers or colloidal particles that allow the film to solidify, so including the influence of a polymer solute or colloidal particles is a third promising extension of this work that may introduce a number of complex phenomena.[34,35]

Chapter 3

A Quantitative Analysis of the Vertical-Averaging Approximation for Evaporating Thin Liquid Films*

I Introduction

Thin liquid films play a key role in numerous industrial processes including the application of paint[9,16,28] and the creation of flexible electronics[2]. Optimization of these processes requires fundamental understanding of film behavior, which is also useful for gaining insight into many natural processes.[10,12,26,55,59] Theoretical models are desirable for developing this understanding because they allow one to systematically explore the influence of various phenomena such as capillary and Marangoni flow, solute transport, and evaporation. However, theoretical models

*Reprinted with permission from Physical Review Fluids 2022, 7, 9, 094002. Copyright 2022 American Physical Society.[58]

quickly become cumbersome as the number of phenomena considered increases, so it is extremely useful to make well-justified simplifications.

It is often desired that thin liquid films have controlled thicknesses and species distributions so that they exhibit desired functionality. To model species transport in a binary film with a solvent and solute, one usually takes the solute concentration to be governed by a convection-diffusion equation. A general formulation considers solute transport through the film depth as well as across the film width, which significantly increases the computational cost of a numerical solution. However, when solute diffusion is sufficiently rapid, one may approximate vertical diffusion as a quasi-steady-state process and consider only solute transport across the film width. This drastically reduces model complexity and is the basis of the vertical-averaging (VA) approximation introduced by Jensen and Grotberg.[13] However, the formal assumptions underlying this approximation are strict for physical systems and the limits of its validity have not been systematically explored under evaporation.[24] Still, the VA approximation (or assumption of vertical uniformity) is popular due to the simplicity it provides.[14–22]

For industrial applications, liquid films are often solidified through evaporation, curing, or other mechanisms. With evaporation, solvent evaporates from the film, leaving behind a solute-rich, solidified film. The process of evaporation consists of two main steps. First, solvent molecules escape from the liquid phase into the gas phase (the phase-change step). Second, the gaseous solvent molecules diffuse away from the liquid-air interface (the diffusion step). To include evaporation in a

theoretical model, one must use an equation to express evaporative fluxes in terms of known quantities such as the film height and solute concentration.

Evaporation models have been developed in previous work, typically assuming a different portion of the evaporative process is limiting. The one-sided evaporation model assumes evaporation is limited by the phase-change step,[33,60] whereas the diffusion-limited model assumes evaporation is limited by the diffusion step. Another common approach is to simply assume evaporation is uniform and constant. As will be discussed below, previous studies on the evolution of evaporating thin films and droplets have employed various combinations of evaporation models and the VA approximation. We will show in §III that the choice of evaporation model, as well as use of the VA approximation, leads to significant qualitative differences in model predictions.

Constant Evaporation: Constant evaporation is a simple, convenient approximation that assumes the evaporation rate is uniform and constant, making it useful for probing fundamental mechanisms. Considering constant evaporation, Serpetsi and Yiantsios[27] examined the stability of a drying binary film and Yiantsios and Higgins[34,61] studied the influence of soluble surfactants and colloidal particles on the evolution of drying films. Yiantsios et al.[31] studied the evolution of a drying polymer film, finding strong dependence on the formation of vertical concentration gradients. Because of its simplicity, constant evaporation has also been used in other studies where the problem is already complex due to factors such as the problem geometry or the presence of colloidal particles.[2,22,32,35,62]

One-Sided Evaporation: The evolution of drying films and droplets consisting of a pure volatile liquid has been extensively studied under one-sided evaporation.[10,26,33,60,63,64] Pham et al.[14] studied the evolution of multicomponent thin films on substrates with topography using this evaporation model. The distribution of colloidal particles in evaporating droplets has also been studied.[15,21,65–67] Many of these studies employ a VA approximation or an assumption of vertical uniformity to ease model complexity. However, Maki and Kumar[66] did not use the VA approximation and were able to capture skin formation (buildup of colloidal particles at the liquid-air interface), which has been shown to inhibit evaporation[68] and significantly affect evolution dynamics.[69]

Diffusion-Limited Evaporation: Diffusion-limited evaporation is commonly used for evaporating droplets, but has also been used for evaporating films.[59,70–72] Deegan et al.[73,74] provided an analytical solution for the evaporative flux of a spherical-cap droplet. Other studies have examined the influence of contact angles,[75] species concentration,[76,77] and many other important quantities on droplet evolution under diffusion-limited evaporation.[17,18,78–80] To ease computational complexity, many of these studies assumed vertical uniformity of any species in the droplets. However, Diddens et al.[76] have demonstrated that vertically nonuniform temperature and solute concentration in binary droplets can have significant effects on droplet evolution. In §III, we will examine the effects of nonuniform solute concentration on diffusion-limited evaporation in thin films.

Previous studies have examined the accuracy of the one-sided and diffusion-

limited evaporation models under various experimental conditions, but are largely limited to evaporating droplets. Sodtke et al.[63] demonstrated excellent agreement between theory and experiment using the one-sided evaporation model for evaporating droplets on heated substrates. Assuming spherical-cap droplets, Deegan et al.[74] highlight agreement between theory and experiment using diffusion-limited evaporation. Hu and Larson[75] built on this work, also showing excellent agreement between theory and experiment with diffusion-limited evaporation. Many other studies have reported experimental data regarding evaporation that has found agreement with subsequent theoretical studies using the one-sided or diffusion-limited evaporation models.[17,18,71,81,82]

Few studies have directly addressed the differences between the common evaporation models,[71,82] and to the best of our knowledge, none have addressed the performance of the VA approximation in the presence of evaporation.[24] The importance of phenomena driven by vertical concentration gradients (and thus the validity of the VA approximation) strongly depends on the rate of diffusion; rapid vertical diffusion will quickly smooth out gradients in species concentration. However, precisely what is considered "rapid" diffusion has not been well established. The VA approximation offers a desirable simplicity, but its influence on the predicted interface shape and species distribution remains unexplored. Therefore, this work presents an analysis of the VA approximation under evaporation for the foundational case of a two-dimensional binary film with volatile solvent and nonvolatile solute. In §II, we derive a two-dimensional (2D) description of the film height and solute concentration in the film which is then simplified using the

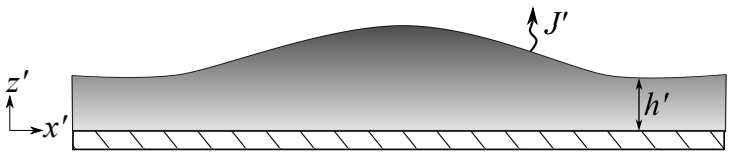

Figure 3.1: Schematic of an evaporating film containing a nonvolatile solute. Shading depicts solute buildup at the liquid-air interface due to solvent evaporation.

VA approximation. To focus on solutal Marangoni flow, we neglect any thermal Marangoni flow induced by evaporation of solvent (discussed further in §D). In §III, we compare results from the 2D description and VA approximation for different evaporation models to gauge the performance of the VA approximation. We then develop scaling relations to gain physical insight into the mechanisms that the VA approximation fails to capture. Conclusions are given in §IV.

II Mathematical Model

We seek to model the film height and species concentration in an evaporating binary thin film as depicted in figure 3.1. The liquid consists of a solvent and solute such that solute concentration gradients create Marangoni stresses that drive Marangoni flow, which in turn creates film-height nonuniformities as shown in figure 3.1. Film height $h'(t', x')$ and solute concentration $c'(t', x', z')$ vary with time t' and the spatial variables x' and z'. The evaporative solvent mass flux $J'(t', x')$ is expressed as a function of h' and c' through evaporation models. We assume periodic boundary conditions in the x'-direction.

A Hydrodynamics

The liquid is assumed Newtonian with constant density ρ and viscosity μ. Surface tension σ' is scaled by the pure solvent surface tension σ_0 and solute concentration c' is scaled by an initial concentration c_0. It is assumed that the ratio of the vertical and lateral characteristic lengths $\epsilon = H/L \ll 1$, allowing the application of lubrication theory. Here, H is the initial film height and L is obtained by balancing viscous and Marangoni stresses at the interface:

$$\mu \frac{\sigma_0 H^2}{\mu L^3} \sim \frac{\omega_0 c_0}{L} \frac{\partial \sigma'}{\partial c'} \quad \Rightarrow \quad L \sim \frac{H}{\sqrt{Ma}}, \tag{3.1}$$

where ω_0 is the initial mass/mole fraction of solute. The viscous scale used in this balance is based on a capillary velocity found by considering mass and momentum balances.[24] Relation (3.1) shows that $\epsilon \sim \sqrt{Ma}$, and thus lubrication theory requires that $\sqrt{Ma} \ll 1$. The Marangoni number Ma is the dimensionless change in surface tension with solute concentration, $Ma = -(\omega_0 c_0/\sigma_0)\, \partial\sigma'/\partial c' \,|_{c'=0}$. It is assumed that the solute lowers the surface tension of the liquid so that $Ma > 0$. The case of $Ma < 0$ can also occur in practice[14] but is not investigated here for the sake of brevity.

The liquid motion is described by the Navier-Stokes equations supplemented with no-slip and no-penetration conditions at the substrate and stress balances at the liquid-air interface. Pressure p' is scaled by $p^* = \sigma_0 \epsilon^2/H$, x-velocity v_x' by $v_x^* = \epsilon^3 \sigma_0/\mu$, z-velocity v_z' by $v_z^* = \epsilon v_x^*$, and time t' by $t^* = H/v_x^* \epsilon$. These scales are derived by balancing the relevant terms in the mass and momentum balances.[24]

Finally, we use the scale J^* for the evaporative mass flux J' that will be given in §C. For the remainder of this work, we use dimensionless variables (indicated without a prime superscript):

$$x' = \epsilon^{-1} H x, \qquad z' = H z, \qquad h' = H h, \qquad \sigma' = \sigma_0 \sigma, \qquad c' = c_0 c,$$

$$v_x' = v_x^* v_x, \qquad v_z' = \epsilon v_x^* v_z, \qquad p' = p^* p, \qquad t' = t^* t, \qquad J' = J^* J. \tag{3.2}$$

The surface tension σ varies linearly with solute concentration c at the interface $z = h$,

$$\sigma = 1 - Ma\, c|_{z=h}. \tag{3.3}$$

This assumes a dilute solute ($\omega_0 \ll 1$) and has been used in previous studies (e.g., Refs. 14 and 27). Here we neglect thermal Marangoni flow to focus on solutal Marangoni flow, but we will revisit thermal effects in §D after deriving expressions for the evaporative flux under each evaporation model. Applying lubrication theory, we retain only leading-order terms in the Navier-Stokes equations to obtain

$$\frac{\partial^2 v_x}{\partial z^2} = \frac{\partial p}{\partial x}, \tag{3.4}$$

$$\frac{\partial p}{\partial z} = 0, \tag{3.5}$$

$$\frac{\partial v_x}{\partial x} + \frac{\partial v_z}{\partial z} = 0. \tag{3.6}$$

No-slip, no-penetration, and stress balance conditions yield the boundary con-

ditions

$$v_x|_{z=0} = v_z|_{z=0} = 0, \tag{3.7}$$

$$p|_{z=h} = -\frac{\partial^2 h}{\partial x^2}, \tag{3.8}$$

$$\left.\frac{\partial v_x}{\partial z}\right|_{z=h} = -\frac{\partial c|_{z=h}}{\partial x}. \tag{3.9}$$

Note that due to the choice of lateral length scale $L = H/\sqrt{Ma}$, the Marangoni number Ma does not appear in tangential stress balance (3.9). Solving these equations for the liquid velocities yields[10]

$$v_x = -\left(\frac{1}{2}z^2 - hz\right)\frac{\partial^3 h}{\partial x^3} - \frac{\partial c|_{z=h}}{\partial x}z, \tag{3.10}$$

$$v_z = \left(\frac{1}{6}z^3 - \frac{1}{2}hz^2\right)\frac{\partial^4 h}{\partial x^4} + \frac{1}{2}\left(\frac{\partial^2 c|_{z=h}}{\partial x^2} - \frac{\partial h}{\partial x}\frac{\partial^3 h}{\partial x^3}\right)z^2. \tag{3.11}$$

Mass conservation at the interface $z = h$ leads to the kinematic condition

$$v_z = \frac{\partial h}{\partial t} + v_x\frac{\partial h}{\partial x} + EJ, \tag{3.12}$$

where the evaporative number $E = J^*/\rho v_x^* \epsilon$ (ratio of evaporative flux to convective flux) and mass flux J arise from solvent evaporation. The definitions of J and J^* depend on the evaporation model and are discussed in §C. Substituting equations (3.10) and (3.11) into equation (3.12) yields the thin-film equation

$$\frac{\partial h}{\partial t} = \underbrace{-\frac{1}{3}\frac{\partial}{\partial x}\left[h^3\frac{\partial^3 h}{\partial x^3}\right]}_{\text{Capillary Flow}} + \underbrace{\frac{1}{2}\frac{\partial}{\partial x}\left[h^2\frac{\partial c|_{z=h}}{\partial x}\right]}_{\text{Marangoni Flow}} - \underbrace{EJ}_{\text{Evaporation}}. \tag{3.13}$$

Thus, the evolution of film height h is coupled to that of solute concentration c through Marangoni flow and evaporation.

B Solute Concentration

The vertical-averaging (VA) approximation simplifies the convection-diffusion equation under the assumption of rapid vertical diffusion. We begin by deriving a 2D description that does not employ the VA approximation in §1 and then give a derivation of the VA approximation in §2. To gauge the performance of the VA approximation, we compare results from the VA approximation to those from the 2D description in §III.

1 2D Description

The solute is assumed to have constant diffusivity D in the solvent and is governed by the dimensionless convection-diffusion equation

$$\frac{\partial c}{\partial t} + v_x \frac{\partial c}{\partial x} + v_z \frac{\partial c}{\partial z} = \frac{1}{Pe}\frac{\partial^2 c}{\partial x^2} + \frac{1}{\epsilon^2 Pe}\frac{\partial^2 c}{\partial z^2}. \tag{3.14}$$

Here, the Péclet number $Pe = Hv_x^*/D\epsilon$ gives the ratio of the lateral diffusive and convective time scales. Similarly, $\epsilon^2 Pe$ gives the ratio of the vertical diffusive and convective time scales. Equation (3.14) is subject to a no-flux condition at the substrate $z = 0$ and a mass-conservation condition at the interface $z = h$:

$$\left.\frac{\partial c}{\partial z}\right|_{z=0} = 0, \qquad \left.\frac{\partial c}{\partial z}\right|_{z=h} - \epsilon^2 \frac{\partial h}{\partial x}\left.\frac{\partial c}{\partial x}\right|_{z=h} = \epsilon^2 PeEJc|_{z=h}. \tag{3.15}$$

Specific forms of the mass flux J and its scale J^* (which determines E) are given in §C. The 2D description is defined as thin-film equation (3.13) coupled with equation (3.14) to describe the film height and full 2D concentration field.

2 Vertical-Averaging (VA) Approximation

When $\epsilon^2 Pe \ll 1$, vertical diffusion is rapid and convection-diffusion equation (3.14) may be transformed to describe an approximate, vertically uniform concentration field.[13] To begin, we expand the concentration c as a perturbation series in powers of $\epsilon^2 Pe$:

$$c(t,x,z) = c_0(t,x,z) + \epsilon^2 Pe\, c_1(t,x,z) + O\left(\left(\epsilon^2 Pe\right)^2\right). \tag{3.16}$$

Substituting equation (3.16) into equation (3.14) gives the $O(1)$ problem

$$\frac{\partial^2 c_0}{\partial z^2} = 0, \tag{3.17}$$

where we have neglected lateral diffusion because it is an $O(\epsilon^2)$ effect. Equation (3.17) is subject to the $O(1)$ no-flux boundary conditions

$$\left.\frac{\partial c_0}{\partial z}\right|_{z=0} = \left.\frac{\partial c_0}{\partial z}\right|_{z=h} = 0. \tag{3.18}$$

Equation (3.17) also requires that $\epsilon^2 PeE \ll 1$, but given that typically, $E \ll 1$, this assumption is valid even if $\epsilon^2 Pe \sim 1$. Equation (3.17) with boundary conditions (3.18) reveals that c_0 is independent of z; the system is under pseudo-steady-state diffusion at leading order.

The $O(\epsilon^2 Pe)$ problem is

$$\frac{\partial c_0}{\partial t} + v_{x,0}\frac{\partial c_0}{\partial x} = \frac{1}{Pe}\frac{\partial^2 c_0}{\partial x^2} + \frac{\partial^2 c_1}{\partial z^2}, \tag{3.19}$$

where $v_{x,0}$ is the $O(1)$ component of the lateral velocity given by

$$v_{x,0} = -\left(\frac{1}{2}z^2 - hz\right)\frac{\partial^3 h}{\partial x^3} - \frac{\partial c_0}{\partial x}z. \tag{3.20}$$

Equation (3.19) is subject to the $O(\epsilon^2 Pe)$ no-flux and mass-conservation conditions

$$\left.\frac{\partial c_1}{\partial z}\right|_{z=0} = 0, \qquad \left.\frac{\partial c_1}{\partial z}\right|_{z=h} - \frac{1}{Pe}\frac{\partial h}{\partial x}\frac{\partial c_0}{\partial x} = EJc_0. \tag{3.21}$$

Applying the averaging-operator $\frac{1}{h}\int_0^h \mathrm{d}z$ to equation (3.19) and using conditions (3.21) allows one to eliminate c_1 and obtain the governing equation

$$\frac{\partial c_0}{\partial t} + \overline{v_x}\frac{\partial c_0}{\partial x} = \frac{1}{h}\frac{1}{Pe}\left(h\frac{\partial c_0}{\partial x}\right) + \frac{1}{h}c_0 EJ \tag{3.22}$$

for c_0. Here, $\overline{v_x}$ is the vertically averaged $O(1)$ lateral velocity given by

$$\overline{v_x} = \frac{1}{h}\int_0^h v_{x,0}\,\mathrm{d}z = \frac{1}{3}h^2\frac{\partial^3 h}{\partial x^3} - \frac{1}{2}h\frac{\partial c_0}{\partial x}. \tag{3.23}$$

Equation (3.22) governs the vertically uniform $O(1)$ profile c_0 and thus contains no dependence on the vertical coordinate z. The vertical-averaging (VA) approximation couples thin-film equation (3.13) with equation (3.22) to predict the

film-height and 1D (vertically uniform) concentration profile. Note that $\epsilon^2 Pe \ll 1$ is only a formal assumption to allow asymptotic expansion (3.16), so it possible that the VA approximation is accurate even outside of this regime (as will be discussed in §III).

C Evaporation

As discussed in §I, there are several commonly used evaporation models, three of which we examine in this work. Constant evaporation has the advantage of simplicity and allows one to more easily probe fundamental mechanisms without choosing constitutive models. The one-sided model is also popular for its relative simplicity (compared to the diffusion-limited model) since one only needs to consider transport in the liquid phase. Diffusion-limited evaporation is the most complicated of the three; since gaseous solvent molecules affect the evaporation rate, one must solve coupled transport equations in the liquid and gas phases. In the following sections, we present a brief derivation of each evaporation model and the resulting expressions for the scale J^* and mass flux J that appear in equations (3.13), (3.15), and (3.22).

1 Constant Evaporation

Constant evaporation is a convenient approximation that is useful for exploring fundamental mechanisms. Under constant evaporation, we simply take the dimensionless mass flux to be $J = 1$ and J^* is left arbitrary. Thus, the magnitude of the evaporative term EJ in equations (3.13), (3.15), and (3.22) is controlled entirely

by the constant parameter E.

2 One-Sided Evaporation

The one-sided evaporation model gives a constitutive equation for the dimensional mass flux J' which is derived from kinetic theory and has been modified to account for capillary pressures:[33,64]

$$\frac{\sqrt{2\pi RT_{sat}}}{\rho_v} J' = \frac{1}{\rho} p'|_{z'=h'} + \frac{L_m}{T_{sat}} (T'|_{z'=h'} - T_{sat}). \tag{3.24}$$

Here, R is the ideal gas constant, T_{sat} is the saturation temperature of the solvent, ρ_v is the density of the gaseous solvent, and L_m is the latent heat of vaporization of the solvent. The dimensional capillary pressure p' is (after applying scalings (3.2) to equation (3.8))

$$p' = -\sigma_0 \frac{\partial^2 h'}{\partial x'^2}. \tag{3.25}$$

The unknown T' is the dimensional temperature of the liquid which can be determined analytically under the lubrication approximation.

We introduce the dimensionless temperature $T = (T' - T_{sat})/\Delta T$ where $\Delta T = (T_b - T_{sat})$. The quantity T_b is the substrate temperature so that we enforce $T' = T_b$ at $z = 0$. We take T to be governed by an energy conservation equation (similar to equation (3.14)), which at leading order is

$$\frac{\partial^2 T}{\partial z^2} = 0. \tag{3.26}$$

This is subject to the boundary conditions

$$T|_{z=0} = 1, \qquad -\left.\frac{\partial T}{\partial z}\right|_{z=h} = J, \tag{3.27}$$

where the latter assumes the air above the film has negligible thermal conductivity and that the evaporative mass flux J is scaled by $J^* = \Delta T k / L_m H$. In dimensionless form, equation (3.24) reads

$$KJ = \delta p|_{z=h} + T|_{z=h}, \tag{3.28}$$

where

$$K = \frac{\sqrt{2\pi R T_{sat}^3}k}{\rho_v L_m^2 H}, \qquad \delta = \frac{p^* T_{sat}}{\rho L_m \Delta T}. \tag{3.29}$$

Equation (3.26) is readily solved subject to boundary conditions (3.27), giving

$$T = 1 - Jz. \tag{3.30}$$

Substituting equations (3.8) and (3.30) into equation (3.28) gives an explicit expression for J,

$$J = \frac{1 - \delta\frac{\partial^2 h}{\partial x^2}}{K + h}, \tag{3.31}$$

in terms of only the film height h. Because we assume a dilute solute, we have used the solvent properties in this derivation and there is no dependence on the solute concentration c. In this work, we take $K = 3.2 \times 10^{-4}$ and $\delta = 5.9 \times 10^{-7}$, which are representative of water with a temperature difference of $\Delta T \approx 3\,\mathrm{K}$. Note that

evaporation is generally more rapid at smaller film heights ($J \sim 1/h$) due to the heated substrate.

3 Diffusion-Limited Evaporation

To derive an explicit expression for the mass flux J under diffusion-limited evaporation, we must solve for the solvent concentration in the gas phase c_g'. We define the dimensionless concentration $c_g = c_g'/c_v$, where c_v is the equilibrium vapor pressure of the solvent. Previous studies have shown through scaling arguments that transient terms in the gas-phase convection-diffusion equation are negligible,[71] and neglecting convective transport gives Laplace's equation governing c_g:

$$\frac{\partial^2 c_g}{\partial x^2} + \frac{\partial^2 c_g}{\partial z^2} = 0. \tag{3.32}$$

One may wish to consider a semi-infinite domain bounded below by the liquid film. A natural boundary condition is then $c_g \to 0$ as $z \to \infty$, assuming the ambient vapor pressure is negligible. Unfortunately, such a boundary condition is ill-posed for Laplace's equation in 2D.[71] Instead, we must consider a finite domain[70] of height $\mathscr{L}$ and apply the boundary condition

$$c_g|_{z=\mathscr{L}} = 0. \tag{3.33}$$

Appropriate values for the evaporation length parameter $\mathscr{L}$ are unclear, but we will see that it has little effect on the qualitative behavior of this model. Because the liquid film is thin, its thickness and curvature are $O(\epsilon)$ effects in the gas phase

and we apply Raoult's law at $z = 0$:

$$c_g|_{z=0} = f(c) = 1 - \omega_0 c|_{z=h} \tag{3.34}$$

where $f(c) = 1 - \omega_0 c|_{z=h}$ is the mole fraction of solvent in the liquid at the interface. Note that the concentration c is defined in the liquid phase where the film-thickness is $O(1)$, and thus is evaluated at the liquid-air interface $z = h$. The simple form of equation (3.34) is a result of assuming a dilute solute ($\omega_0 \ll 1$) so that we may approximate the liquid's properties as those of the solvent. In this work, we fix $\omega_0 = 0.1$ since changes in it do not qualitatively affect the results presented in §III. To compute the evaporative mass flux, we note that Fick's law gives

$$J = - \left. \frac{\partial c_g}{\partial z} \right|_{z=0} \tag{3.35}$$

where the mass flux is scaled by $J^* = c_v D_g \epsilon / \mathscr{L}$. Here, D_g is the diffusivity of the gaseous solvent in air.

Equation (3.32) subject to boundary conditions (3.33) and (3.34) can be solved on the domain $x \in (0, 2\pi/\alpha)$ and $z \in (0, \mathscr{L})$ by separation of variables to obtain the flux

$$J = \frac{\overline{f}}{\mathscr{L}} + \sum_{k \neq 0} \tilde{f}_k e^{-\alpha k i x} \alpha k \coth(\alpha k \mathscr{L}), \tag{3.36}$$

where $\overline{f} = \tilde{f}_0$ is the spatial average of f, $\tilde{f}_k$ is the k-th Fourier coefficient of f, and α is the wavenumber of the perturbation described in §III. A detailed derivation of this expression is given in the appendix. We see that the evaporative

flux J contains a laterally uniform component $\overline{f}/\mathscr{L}$ that scales linearly with the solvent mole fraction at the interface and inversely with the evaporation length $\mathscr{L}$. This term is like constant evaporation, except that it decreases with time as solute builds up and $\overline{f}$ decreases. We will see in §III that the additional terms in equation (3.36) are self-inhibiting and thus J is essentially laterally uniform. Therefore, the parameter $\mathscr{L}$ only affects the magnitude of the evaporative flux and has little effect on its qualitative behavior. In this work, we fix $\mathscr{L} = 5$, but results for different $\mathscr{L}$ are given in the appendix for reference.

D Thermal Marangoni Effects

While we have neglected thermal Marangoni effects in the derivation of this model (see §A), they warrant a brief discussion because solvent evaporation will induce temperature variations. To account for thermal Marangoni flow in the film, we must solve for the lateral temperature gradient at the interface $z = h$. However, the constant and diffusion-limited evaporation models do not include a temperature profile in their derivations, so the temperature profile is not uniquely defined and depends on how one handles heat transfer at the solid substrate.[82–84] This is beyond the scope of this work, so we will not discuss thermal Marangoni effects for constant or diffusion-limited evaporation, though they can be appreciable.[29,34,64,72,83–85] However, for one-sided evaporation, the temperature profile at the interface is given by equation (3.30),

$$T|_{z=h} = 1 - Jh \approx \frac{K}{K+h} \approx \frac{K}{h} \quad \Rightarrow \quad \frac{\partial\, T|_{z=h}}{\partial x} \approx -\frac{K}{h^2}\frac{\partial h}{\partial x}, \tag{3.37}$$

where we have neglected the contribution from capillary pressure since $\delta \ll 1$. Equation (3.37) shows that temperature gradients form over the same $O(1)$ length scale as film-height gradients. Furthermore, $K \ll 1$ as discussed in §2, so the dimensionless temperature gradient $\partial T/\partial x \sim K \ll 1$ is negligible and we do not expect thermal Marangoni effects to be important under one-sided evaporation.

E Numerical Method and Parameter Values

There are three dimensionless groups that appear in governing equations (3.13), (3.14), and (3.22). The first is the Péclet number Pe, which gives the ratio of the lateral diffusive and convective time scales. The second is the Marangoni number $Ma = \epsilon^2$, which gives the ratio of Marangoni forces to capillary forces but also defines the lateral length scale $L = H/\sqrt{Ma}$. The Marangoni number appears in the lumped parameter $\epsilon^2 Pe = MaPe$ that gives the ratio of the vertical diffusive and convective time scales. Note that $\epsilon^2 Pe$ does not appear in equation (3.22) because vertical diffusion is quasi-steady under the VA approximation. The third is the evaporative number E which controls the magnitude of the evaporative-flux term EJ. Typical values of dimensional and dimensionless parameters are given in tables 3.1 and 3.2, respectively. The effects of varying these parameters are explored in §III.

For the 2D description (see §1), equation (3.14) is subject to mass-conservation condition (3.15) at the moving boundary $z = h(t, x)$. To circumvent numerically solving a moving-boundary problem, a coordinate transformation $(x, z, t) \mapsto$

Table 3.1: Table of important dimensional parameters and their typical values.

Parameter	Definition	Typical Values
H (m)	film thickness	10^{-5}-10^{-4}
μ (Pa s)	solvent viscosity	10^{-4}-10^{-3}
σ_0 (N/m)	solvent surface tension	10^{-2}-10^{-1}
D (m^2/s)	solute diffusivity	10^{-9}
ω_0	solute mass/mole fraction	10^{-2}-10^{-1}
T_{sat} (K)	saturation temperature	3×10^2
k (W/m K)	thermal conductivity	$10^{-1} - 10^0$
ρ (kg/m^3)	liquid density	$10^2 - 10^3$
ρ_v (kg/m^3)	vapor density	$10^{-1} - 10^0$
L_m (J/kg)	latent heat of vaporization	$10^5 - 10^6$

(ζ, η, τ) is performed with the relations[4]

$$\eta = \frac{z}{h}, \qquad \frac{\partial \zeta}{\partial x} = 1, \qquad \frac{\partial \tau}{\partial t} = 1. \tag{3.38}$$

Here, η is a scaled vertical coordinate, ζ is the lateral coordinate, and τ is the time coordinate. The interface at $\eta = 1$ is now constant, but the governing equations become significantly more complex with the derivative transformations

$$\frac{\partial}{\partial x} = \frac{\partial}{\partial \zeta} - \frac{\eta}{h}\frac{\partial h}{\partial \zeta}\frac{\partial}{\partial \eta}, \qquad \frac{\partial}{\partial z} = \frac{1}{h}\frac{\partial}{\partial \eta}, \qquad \frac{\partial}{\partial t} = \frac{\partial}{\partial \tau} - \frac{\eta}{h}\frac{\partial h}{\partial \tau}\frac{\partial}{\partial \eta}. \tag{3.39}$$

After applying transformation (3.38) to equations (3.13) and (3.14), a psuedospectral method is employed to solve the resulting set of coupled fourth-order nonlinear partial differential equations on the constant domain $\zeta \in (0, 2\pi/\alpha)$ and $\eta \in (0, 1)$.[4,50,51] To enforce periodicity, the lateral domain is discretized into 64

Table 3.2: Important dimensionless parameters and typical values.

Parameter	Definition	Physical Meaning	Typical Values
ϵ	$H/L, \sqrt{Ma}$	vertical length/lateral length	10^{-2}-10^{-1}
Ma	$\Delta\sigma\omega_0/\sigma_0$	Marangoni forces/surface-tension forces	10^{-3}-10^{-1}
E	$J^*\mu/\rho\sigma_0\epsilon^4$	evaporative flux/convective flux	$10^{-4} - 10^{-2}$
Pe	$H\sigma_0\epsilon^2/D\mu$	diffusion time/convection time	$1 - 10^6$

Fourier modes, while the vertical domain is discretized into 20 Chebyshev polynomials. The equations for the VA approximation contain no dependence on the vertical coordinate, so transformation (3.38) is not used and the expansion is in Fourier modes only. Note that this is a significant simplification that results in 20 times fewer computational nodes. Time stepping is performed via MATLAB's solver `ode15i` which is a variable-step, variable-order solver employing backward differentiation. The model and numerical method have been verified by reproducing results for pure film leveling and simple cases of evaporating binary films.[10,24,27] We have also verified that the 2D description and VA approximation are in quantitative agreement at low Pe (fast vertical diffusion) in §III.

III Results and Discussion

While the vertical-averaging (VA) approximation formally assumes $\epsilon^2 Pe \ll 1$ (see §2), the actual limits of validity under evaporation have not been established. To examine the performance of the VA approximation, we compare predictions to those from the 2D description (see §1) as the Péclet number Pe varies. We begin by establishing a metric to compare the VA approximation and 2D description.

The initial conditions

$$h(t=0)=1, \qquad c(t=0)=1+c_p\cos(\alpha x) \tag{3.40}$$

represent an initially uniform film thickness and a concentration field with a small lateral perturbation of magnitude c_p. For all presented results, we take $c_p = 10^{-2}$ and $\alpha = 0.3$ since changes to these parameters do not qualitatively influence the results.

Simulations are stopped at time $t = t_{max}$, when the thinnest point of the film reaches $h_{min} = 0.1$, for three reasons. First, we do not include a disjoining pressure in this work that would be required to describe ultra-thin films. Second, the transformation described by equation (3.38) becomes stiff, making numerical integration difficult. Third, the diffusion-limited evaporative flux in equation (3.36) decreases in magnitude as solute builds up, reaching 0 when $c|_{z=h} = \omega_0^{-1}$. Consequently, with $\omega_0 = 0.1$, it can be shown that a spatially uniform film under diffusion-limited evaporation will not decrease below $h = \omega_0 = 0.1$.

The perturbation imposed in equation (3.40) causes the film to deform in response to Marangoni flow toward the lateral center of the film ($x = \pi/\alpha$); the perturbation is a depletion of solute in the center of the film, causing a locally high surface tension and Marangoni stresses that drive flow toward the center of the film to form a crest in the film height. However, evaporation of solvent is simultaneously acting to decrease the film height and causes a buildup of solute at the interface. The effects of evaporation on the film height depend on the

evaporation model, and the buildup of solute depends on the vertical diffusion time scale $\epsilon^2 Pe$ (assumed negligible in the VA approximation). Figure 3.2 shows concentration contours from the 2D description and VA approximation under each evaporation model near parameter values where we first observe discrepancies between the 2D description and VA approximation ($Pe = 1.7 \times 10^4$, $E = 3 \times 10^{-3}$, and $\epsilon = 0.1$). Note the differences in the film-height and solute-concentration profiles between the predictions from each approach.

Figures 3.2 (a) and (b) show that under constant evaporation, the 2D description predicts a significantly smaller film-height perturbation than the VA approximation. This is due to sharp vertical concentration gradients that form as solute builds up at the interface from solvent evaporation; this will be discussed in §A. Figures 3.2 (c) and (d) show a different trend under one-sided evaporation, where the 2D description predicts a larger film-height perturbation due to the sensitivity of one-sided evaporation to changes in the film height, which will be discussed in §B. The results under the diffusion-limited evaporation model, depicted in figures 3.2 (e) and (f), are similar to the case of constant evaporation in figures 3.2 (a) and (b). This is because the diffusion-limited evaporation model behaves qualitatively like constant evaporation, as will be discussed in §C. (Figures at larger Pe are provided in the appendix where these differences are accentuated.) Figure 3.2 shows that the size of the film-height perturbation is a useful metric for comparing predictions from the various approaches. At $t = t_{max}$, we denote the peak-to-trough height of the film as Δh.

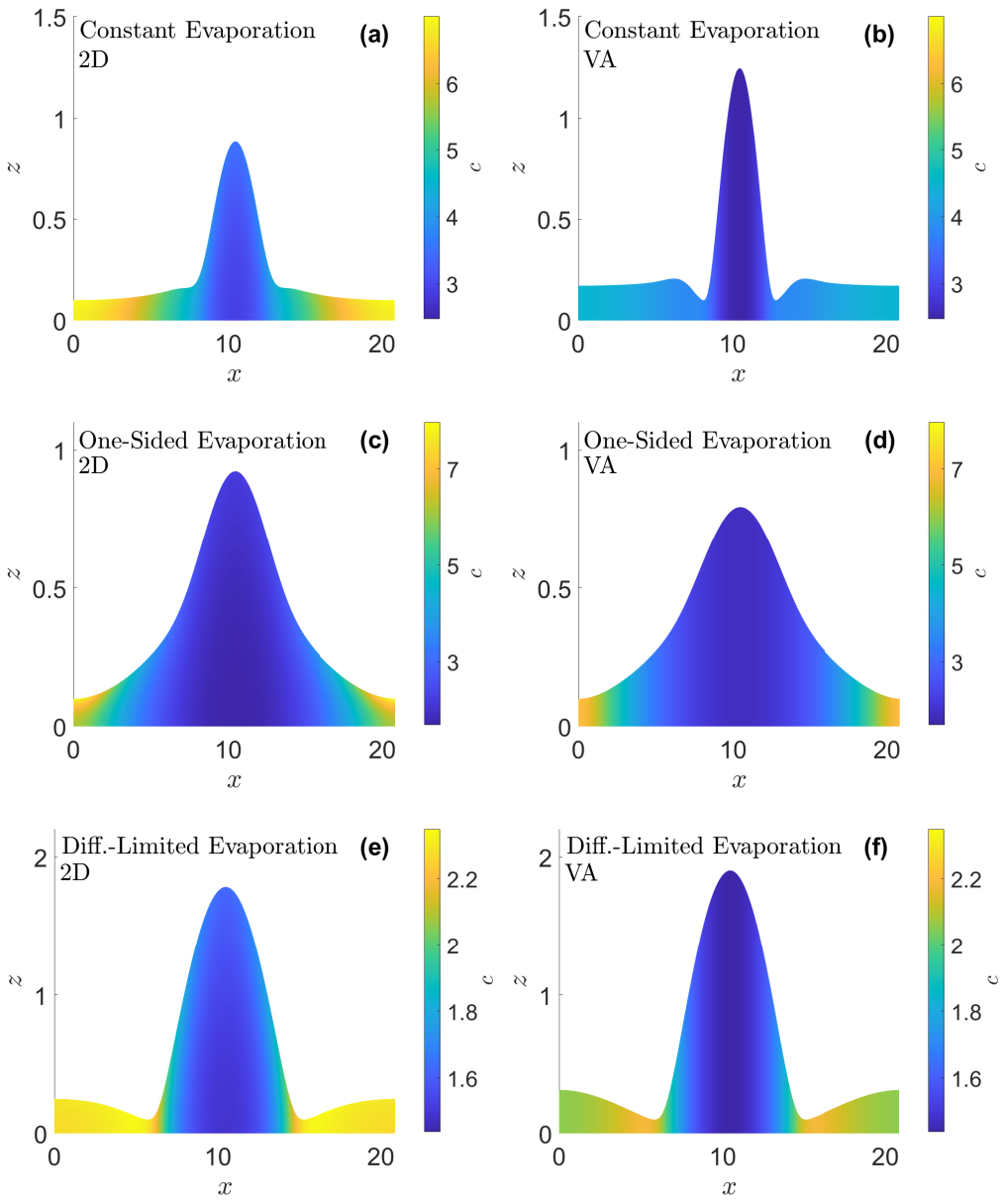

Figure 3.2: Concentration contours for $Pe = 1.7 \times 10^4$, $E = 3 \times 10^{-3}$, and $\epsilon = 0.1$ at $t = t_{max}$. Note the qualitative differences in both the film-height and solute concentration profiles. The value of Pe chosen is near the value where differences between each approach become visible. The corresponding times are (a) $t_{max} = 2.56 \times 10^2$, (b) $t_{max} = 2.35 \times 10^2$, (c) $t_{max} = 1.39 \times 10^2$, (d) $t_{max} = 1.41 \times 10^2$, (e) $t_{max} = 7.30 \times 10^2$, and (f) $t_{max} = 6.76 \times 10^2$. A side-by-side comparison of these profiles is shown in the appendix.

Figure 3.2 exemplifies the differences between each modeling approach. From figures 3.2 (a) and (c), it is clear that the evaporation model significantly affects the predicted film-height profile and solute distribution. Furthermore, figures 3.2 (a) and (b) show that the VA approximation can lead to drastically different predictions compared to the 2D description. In the following sections we consider each evaporation model in detail and discuss the mechanisms that give rise to the differences between the 2D description and VA approximation.

A Constant Evaporation

Figures 3.2 (a) and (b) show that under constant evaporation with $E = 3 \times 10^{-3}$, the 2D description predicts a significantly smaller film-height perturbation Δh than the VA approximation at large Pe. However, when Pe is small, one expects rapid vertical diffusion and thus the VA approximation to agree well with the 2D description. To confirm this, figure 3.3 (a) shows Δh for a range of Pe under constant evaporation with $E = 3 \times 10^{-3}$. Notably, the 2D description (red circles) and VA approximation (blue diamonds) agree well at small Pe, but the 2D description predicts a significantly smaller height perturbation Δh than the VA approximation at large Pe (consistent with figures 3.2 (a) and (b)). However, at a larger evaporative number $E = 9 \times 10^{-2}$ (figure 3.3 (c)), the opposite trend occurs, where the 2D description predicts a larger Δh. Consequently, there is a region at intermediate E where the 2D description transitions from predicting a smaller Δh to a larger Δh, as shown in figure 3.3 (b). To understand the trends in figure 3.3, we first explain the behavior at small Pe, then establish precisely

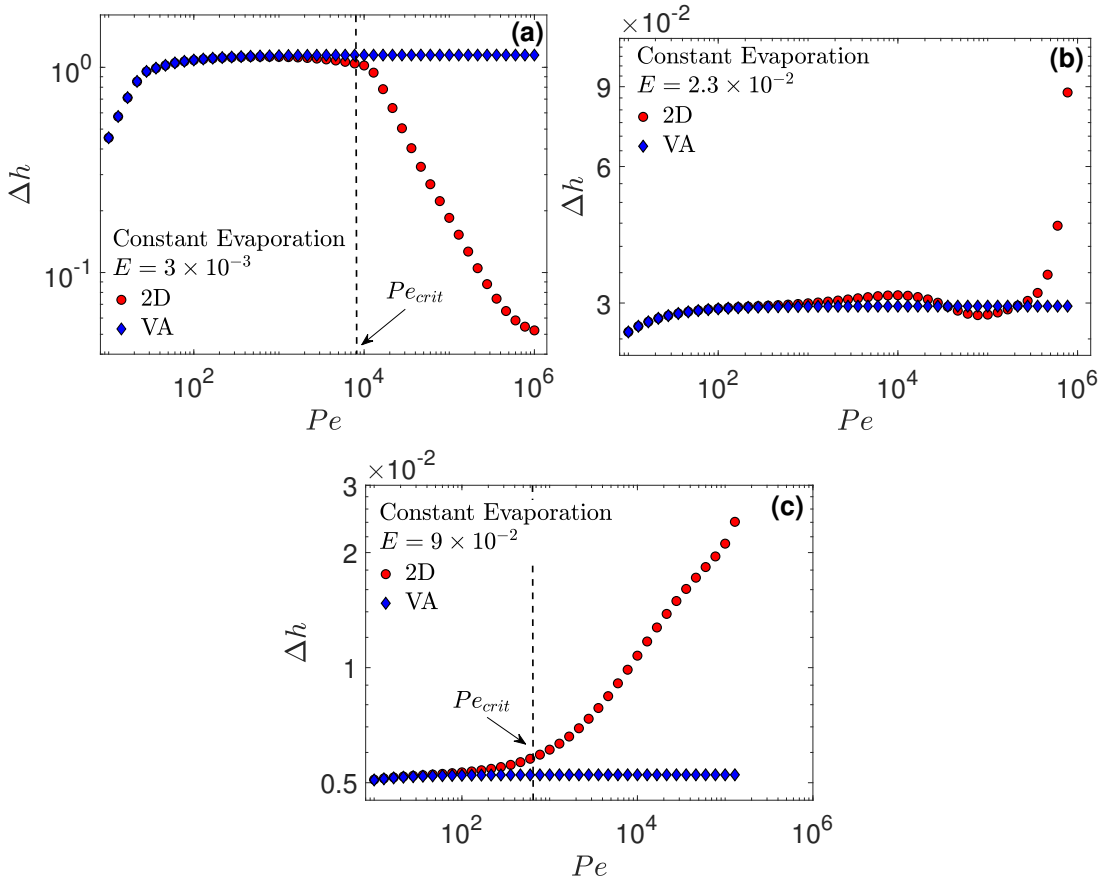

Figure 3.3: The height perturbation Δh for (a) $E = 3 \times 10^{-3}$, (b) $E = 2.3 \times 10^{-2}$, and (c) $E = 3 \times 10^{-2}$ for varying Pe and constant evaporation. Note that Δh predicted by the 2D description decreases at large Pe for small E, but increases at large Pe for larger E.

what is meant by small or large Pe, and finally elucidate the mechanisms that the VA approximation fails to capture at high Pe.

At sufficiently small Pe, figure 3.3 shows that the 2D description and VA approximation agree well and predict an increasing Δh as Pe increases. Since the evaporative term scales as c/h in the VA approximation (equation (3.22)), solute buildup from evaporation increases as the film thins. Thus, thinner parts of the film (edges) will develop higher solute concentration than thicker regions (center), exacerbating the perturbation imposed in equation (3.40). The strong Marangoni flows that result can even cause a double-peak film-height profile to

develop like that shown in figure 3.2 (b). As Pe increases, lateral diffusion slows, so solute concentration perturbations decay less over time and give larger Marangoni stresses and thus larger film-height perturbations for the VA approximation, as shown in figure 3.3.

At large enough Pe, the 2D description and VA approximation no longer agree well. To have a consistent metric for evaluating performance of the VA approximation, we consider the 2D description and VA approximation to not agree well when predictions for Δh differ by more than 10%. The value of Pe at which this first occurs is denoted the critical Péclet number Pe_{crit} and is marked in figures 3.3 (a) and (c). We have not marked Pe_{crit} on figure 3.3 (b) because the value changes erratically as the system transitions between the two regimes shown in figures 3.3 (a) and (c). For large Pe ($Pe > Pe_{crit}$) the 2D description and VA approximation do not agree well, with the 2D description predicting either a smaller or larger Δh depending on the value of E. Note that the values of Pe_{crit} shown in figures 3.3 (a) and (c), $Pe_{crit} \approx 10^4$ and $Pe_{crit} \approx 10^3$, respectively, are larger than the asymptotic assumption $\epsilon^2 Pe \ll 1$ would suggest ($Pe_{crit} \approx 10^2$), so the VA approximation is "overperforming".

The VA approximation is an asymptotic analysis that retains only the leading-order term $c_0(t, x)$ in equation (3.16). Thus, we may learn what mechanisms it fails to capture by examining the neglected first-order correction $c_1(t, x, z)$. By subtracting equation (3.22) from equation (3.19), we obtain a second-order ODE

for c_1 that can be integrated twice to obtain

$$c_1 - c_1|_{z=0} = \left[\int_0^z \int_0^{z'} v_{x,0} - \overline{v_x}\,\mathrm{d}z''\,\mathrm{d}z'\right] \frac{\partial c_0}{\partial x} + \frac{z^2}{2hPe}\frac{\partial h}{\partial x}\frac{\partial c_0}{\partial x} + \frac{z^2 c_0}{2h} EJ, \quad (3.41)$$

where z' and z'' are dummy integration variables and $c_1|_{z=0}$ is an unknown function of t and x. This term remains because boundary conditions (3.21) are insufficient to fully determine c_1; rigorously following the asymptotic analysis, we must go to $O\left((\epsilon^2 Pe)^2\right)$ to determine $c_1|_{z=0}$. However, we are only interested in the qualitative behavior of c_1, so we instead enforce the condition $\frac{1}{h}\int_0^h c_1\,\mathrm{d}z = 0$ which implies that c_0 is the vertical average of c and c_1 is a perturbation around this average. A derivation of c_1 is given in the appendix.

Figure 3.3 indicates that the evaporation rate is important in determining when the VA approximation breaks down (i.e., Pe_{crit}), suggesting that evaporation is likely the dominant term in equation (3.41). Thus, we substitute equation (3.41) for $c_1|_{z=0}$ and neglect all terms except evaporation to obtain

$$c_1(t,x,z) \approx \frac{EJhc_0}{2}\left(\left(\frac{z}{h}\right)^2 - \frac{1}{3}\right) \quad (3.42)$$

Note that c_1 is parabolic in z and decreases as we move away from the interface $z = h$. Therefore, c_1 represents vertical solute concentration gradients from evaporation that are not captured by the VA approximation. By examining the magnitude of these gradients, we can determine scaling relations for Pe_{crit}.

In the system investigated here, Marangoni flow is the only process through

which solute concentration affects film height. The strength of Marangoni flow is determined by the magnitude of the Marangoni stress

$$\frac{\partial c|_{z=h}}{\partial x} = \frac{\partial c_0}{\partial x} + \epsilon^2 Pe \frac{\partial c_1|_{z=h}}{\partial x} + O\left(\left(\epsilon^2 Pe\right)^2\right). \tag{3.43}$$

The first-order correction is not captured by the VA approximation, so when this is significant we expect to see film-height profile deviations between the 2D description and VA approximation. Noting that this occurs when $Pe \sim Pe_{crit}$, we expect that

$$\frac{\partial c_0}{\partial x} \approx \epsilon^2 Pe_{crit} \frac{\partial c_1|_{z=h}}{\partial x} \sim \epsilon^2 Pe_{crit} E \frac{\partial}{\partial x}\left(Jhc_0\right), \tag{3.44}$$

where we have used equation (3.42). Under constant evaporation, $J = 1$ and is constant, but in general $J = J(x)$ so we retain it in this derivation. Expanding the derivative in equation (3.44) gives

$$\frac{\partial c_0}{\partial x} \sim \epsilon^2 Pe_{crit} E \Bigg(\underbrace{Jc_0 \frac{\partial h}{\partial x}}_{\text{(a)}} + \underbrace{Jh \frac{\partial c_0}{\partial x}}_{\text{(b)}} + \underbrace{hc_0 \frac{\partial J}{\partial x}}_{\text{(c)}} \Bigg). \tag{3.45}$$

which contains contributions from (a) height gradients, (b) lateral concentration gradients, and (c) non-uniform evaporation rates.

By examining each term in equation (3.45), we can understand why the VA approximation breaks down, how Pe_{crit} scales with E, and if the 2D description will predict a larger or smaller Δh than the VA approximation. Term (a) in equation (3.45) represents a correction for vertical concentration gradients; using

boundary conditions (3.21),

$$EJc_0\frac{\partial h}{\partial x} \approx \left.\frac{\partial c_1}{\partial z}\right|_{z=h}\frac{\partial h}{\partial x}, \tag{3.46}$$

where we have neglected a small diffusive correction. Thus, term (a) in equation (3.45) represents vertical concentration gradients coupling with film-height gradients. Recalling that the solute lowers the surface tension of the liquid, the lateral height ($\partial h/\partial x$) and concentration ($\partial c_0/\partial x$) gradients are opposite in sign (this can be observed in figure 3.2). Since $\partial c_1/\partial z > 0$ due to evaporation, term (a) in equation (3.45) counteracts Marangoni stresses and if dominant, shows that the 2D description will predict a smaller Δh. Consider figure 3.2 (a); if the film were to deform more, the troughs would descend into regions of lower concentration, which would raise the surface tension. This will pull fluid away from the crests toward the troughs, tending to reverse the deformation. Through this mechanism, vertical concentration gradients can inhibit lateral Marangoni flow. Figure 3.3 (a) shows that the 2D description predicts smaller Δh at lower E, and thus we expect this mechanism to be dominant at low E (slow evaporation).

Term (b) in equation (3.45) is always the same sign as the leading-order Marangoni stress $\partial c_0/\partial x$ and will lead to larger Δh in the 2D description. This term represents a lateral concentration gradient that is localized to the interface. Note the latter of boundary conditions (3.15) that shows solute buildup at the interface from evaporation ($\partial c/\partial z$) is proportional to the value of the concentration at the interface. Due to the imposed perturbation, the concentration is higher

near the edges (troughs) and lower in the center (crest). Thus, concentration will build up locally at the interface faster in the troughs than at the crests, creating a lateral concentration gradient localized to the interface. Through this mechanism, vertical concentration gradients can exacerbate lateral Marangoni flow. Figure 3.3 (c) shows the 2D description predicting larger Δh, and thus we expect this mechanism to be dominant at higher E (fast evaporation). Term (c) in equation (3.45) is identically zero for constant evaporation but will be discussed in more detail in §B.

Figure 3.3 (a) shows that at low E, the 2D description predicts a smaller Δh at high Pe and thus we expect term (a) in equation (3.45) is dominant. From this, we can obtain a scaling relation for Pe_{crit} by determining how the film height and concentration scale with E. To obtain an order-of-magnitude estimate for c_0, consider the case of a laterally uniform, evaporating film; to conserve mass, we must have $c_0 = 1/h$ and so we can expect $c_0 \sim 1/h$ in a nonuniform system. To obtain an estimate for h, recall that at the end of the numerical simulations, the minimum value of h is $h_{min} = 0.1$ and thus the maximum value is $h_{max} = 0.1 + \Delta h$. The average of these two values gives

$$h \sim \frac{1}{2}\left(h_{min} + h_{max}\right) = 0.1 + \frac{1}{2}\Delta h \sim \begin{cases} \text{constant} & \Delta h \ll 0.1 \\ \\ \Delta h & \Delta h \gg 0.1 \end{cases}. \tag{3.47}$$

Observe in figures 3.3 (a) and (c) that $\Delta h \gg 0.1$ at low E and $\Delta h \ll 0.1$ at higher E. Intuitively, very fast evaporation (higher E) causes the film to dry out before

Marangoni flow can develop a large film-height perturbation, so Δh is smaller at higher E. Therefore,

$$c_0 \sim \frac{1}{h}, \quad h \sim \begin{cases} \text{constant} & \text{higher } E \\ \Delta h & \text{low E} \end{cases}. \tag{3.48}$$

Because we are only interested in the scaling with the evaporative number E and the lateral domain is constant, we take $\partial h/\partial x \sim \Delta h$ and $\partial c_0/\partial x \sim \Delta c$. From equation (3.45), we then have at low E (using term (a))

$$\Delta c \sim \epsilon^2 Pe_{crit} E \quad \Rightarrow \quad \epsilon^2 Pe_{crit} \sim \frac{\Delta c}{E}, \qquad \text{(low E)} \tag{3.49}$$

and at higher E (using term (b))

$$\Delta c \sim \epsilon^2 Pe_{crit} E \Delta c \quad \Rightarrow \quad \epsilon^2 Pe_{crit} \sim \frac{1}{E}. \qquad \text{(higher E)} \tag{3.50}$$

Relation (3.50) for higher E implies that the VA approximation breaks down when $\epsilon^2 PeE \sim$ constant. The grouping $\epsilon^2 PeE$ represents the relative strengths of vertical diffusion and evaporation, so it is intuitive that this grouping is indicative of the importance of vertical concentration gradients and breakdown of the VA approximation. This is true when evaporation is fast and film-height gradients are unimportant. But when evaporation is slow, there is a coupling between vertical concentration gradients and film-height gradients that leads to a different relation given by equation (3.49). To close relation (3.49), we must quantify the size of

lateral concentration gradients (Δc) by considering governing equations (3.13) and (3.22).

Note that at the maximum deformation, Marangoni and capillary flow must balance each other, and thus we expect that they scale similarly. From equations (3.13) and (3.48), this implies (for low E)

$$\Delta h^4 \sim \Delta h^2 \Delta c \quad \Rightarrow \quad \Delta c \sim \Delta h^2. \tag{3.51}$$

For this analysis, we assume that this relation holds at $t = t_{max}$ despite not obtaining the maximum deformation. Next, recall that the film-height perturbation develops over time due to Marangoni flow, and thus we balance the time derivative with Marangoni flow in equation (3.13) to obtain

$$\frac{\Delta h}{\Delta t} \sim \Delta h^2 \Delta c \quad \Rightarrow \quad \Delta t \sim \frac{1}{\Delta h \Delta c}. \tag{3.52}$$

Finally, the evolution of the concentration field is primarily due to evaporation, so we balance the time derivative with evaporation in equation (3.22) to obtain

$$\frac{\Delta c}{\Delta t} \sim \frac{E}{\Delta h^2} \quad \Rightarrow \quad \Delta t \sim \frac{\Delta h^2 \Delta c}{E}. \tag{3.53}$$

Combining these three relations with relations (3.49) and (3.50) gives

$$\epsilon^2 Pe_{crit} \sim \begin{cases} E^{-5/7} & \text{low E} \\ \\ E^{-1} & \text{higher E} \end{cases}. \tag{3.54}$$

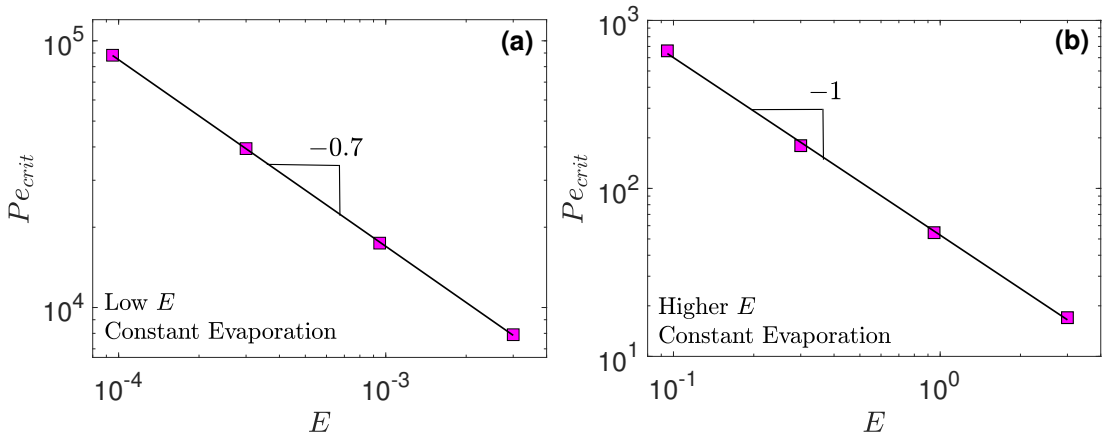

Figure 3.4: Pe_{crit} at various values of E under constant evaporation for (a) low E and (b) higher E. The system transitions between these two scaling regimes at intermediate E and Pe_{crit} appears erratic, so these values are not shown.

To verify equation (3.54), we plot Pe_{crit} for various values of the evaporative number E obtained from numerical simulations in figure 3.4. Figure 3.4 (a) shows a numerical scaling $Pe_{crit} \sim E^{-0.7}$ at low E which is close to the analytical scaling $Pe_{crit} \sim E^{-5/7}$ from equation (3.54). Figure 3.4 (b) shows a numerical scaling $Pe_{crit} \sim E^{-1}$ at higher E which is exactly the analytical scaling from equation (3.54). However, despite these scaling exponents being similar in magnitude to each other ($-5/7$ and -1), the type of disagreement between the 2D description and VA approximation is qualitatively different as shown in figures 3.3 (a) and (c) due to the mechanisms discussed above. The weaker scaling at low E ($Pe_{crit} \sim E^{-5/7}$) is a result of slower evaporation; there is more time for Marangoni flow to develop significant film-height perturbations which decreases the relative importance of evaporation in the system.

When deriving relations (3.54), we assumed that the vertical concentration gradients from evaporation (reflected in equation (3.42)) lead to the dominant

mechanisms that the VA approximation fails to capture. The agreement between relations (3.54) and the numerical results shown in figure 3.4 shows that the disagreement between the 2D description and VA approximation is indeed due to significant vertical concentration gradients that are important for film evolution. Equation (3.45) shows the three mechanisms through which vertical concentration gradients influence Marangoni stresses. Term (a) is dominant for slow evaporation and represents direct coupling of vertical concentration gradients with film-height gradients that acts to inhibit Marangoni stresses (see equation (3.46)). Term (b) is dominant for fast evaporation and represents lateral concentration gradients that develop locally at the interface and exacerbate Marangoni stresses. These two mechanisms cause the discrepancies between the 2D description and the VA approximation for $Pe > Pe_{crit}$ shown in figure 3.3 and lead to two different relations for Pe_{crit} given in equation (3.54).

B One-Sided Evaporation

Figures 3.2 (c) and (d) show that under one-sided evaporation with $E = 3 \times 10^{-3}$, the 2D description predicts a larger film-height perturbation Δh than the VA approximation. This is in contrast to what we observe under constant evaporation in figures 3.2 (a) and (b) at the same value of E. Figure 3.5 (a) shows Δh for a range of Pe and $E = 3 \times 10^{-3}$ under one-sided evaporation. Like the case of constant evaporation, we observe good agreement between the 2D description and VA approximation at low Pe ($Pe < Pe_{crit}$), but for $Pe > Pe_{crit}$ there is no longer good agreement because vertical concentration gradients become significant.

However, the deviation between the 2D description and VA approximation in figure 3.5 (a) is qualitatively different from that observed under constant evaporation in figure 3.3 (a); for all values of E investigated, the 2D description predicts larger Δh as Pe increases.

Figure 3.5 (b) shows numerically computed Pe_{crit} for a large range of E. At higher E, we see the same scaling $Pe_{crit} \sim E^{-1}$ as under constant evaporation in figure 3.4 (b), but the behavior is different at low E; the erratic transition discussed in §A is not present, and we instead see a smoother transition with the local slope increasing steadily (becoming less negative) as we decrease E. Unfortunately, numerical difficulties arising from the large height nonuniformities coupling with the nonuniform evaporation rate have prevented us from obtaining data at lower E than presented in figure 3.5 (b) ($E < 3 \times 10^{-3}$). Nevertheless, the behavior at lower values of E is qualitatively distinct from that observed under constant evaporation. To understand the mechanisms that cause this, we first briefly discuss the behavior for $Pe < Pe_{crit}$ and then revisit equation (3.45) to show how one-sided evaporation causes the 2D description to predict larger Δh even at low E.

Examining figure 3.5 (a), we see that Δh increases as Pe increases for $Pe < Pe_{crit}$. This is due to the same mechanisms as under constant evaporation; larger Pe allows larger concentration gradients to persist which causes stronger Marangoni flow and thus larger Δh (see §A). However, comparing figures 3.3 (a) and 3.5 (a), we see that Δh is generally smaller under one-sided evaporation than

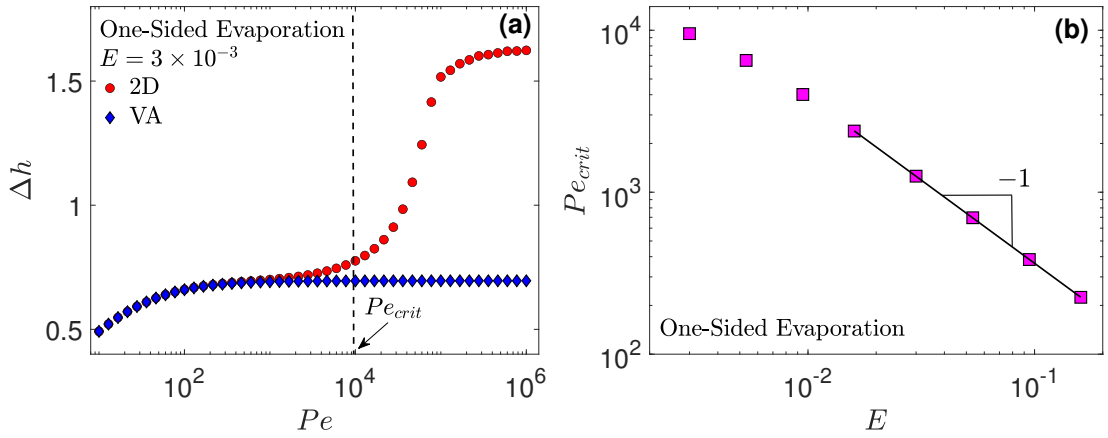

Figure 3.5: (a) The height perturbation Δh for $E = 3 \times 10^{-3}$ and varying Pe under one-sided evaporation. Note that Δh predicted by the 2D description increases at large Pe. (b) Pe_{crit} at various values of E.

under constant evaporation for $Pe < Pe_{crit}$. This is because the evaporative flux under one-sided evaporation $J \sim 1/h$ (equation (3.31)) is faster overall, reducing the time for film deformation and giving smaller Δh. This evaporative flux is also key to explaining the different trend in Pe_{crit} in figure 3.5 (b). With $J \sim 1/h$, evaporation is faster where the film is thinner, so term (c) in equation (3.45) may be significant. Noting that $\delta \ll 1$ (see §2), we may neglect pressure contributions in equation (3.31) to obtain

$$\frac{\partial J}{\partial x} \approx -\frac{1}{(K+h)^2}\frac{\partial h}{\partial x} \approx -J^2\frac{\partial h}{\partial x}. \tag{3.55}$$

One-sided evaporation causes solute to build up more rapidly on the edges of the film (where the film is thin) and more slowly in the center, exacerbating the imposed perturbation at the interface. This causes larger Marangoni stresses that are proportional to the height gradient $\partial h/\partial x$ as shown in equation (3.55).

Substituting equation (3.55) into relation (3.45) gives

$$\frac{\partial c_0}{\partial x} \sim \epsilon^2 Pe_{crit} E \Bigg(\underbrace{J c_0 \frac{\partial h}{\partial x}}_{\text{(a)}} + \underbrace{J h \frac{\partial c_0}{\partial x}}_{\text{(b)}} - \underbrace{c_0 h J^2 \frac{\partial h}{\partial x}}_{\text{(c)}} \Bigg). \tag{3.56}$$

Note that term (a), representing vertical concentration gradients coupling with film-height gradients, and term (c), representing nonuniform solute buildup from a nonuniform evaporative flux, are both proportional to the height gradient $\partial h/\partial x$ but opposite in sign; the nonuniform buildup of solute caused by nonuniform evaporation (term (c)) causes larger Marangoni stresses that directly counteract the inhibition of Marangoni stresses by vertical concentration gradients (term (a)). Furthermore, since $\delta \ll 1$,

$$1 - hJ = 1 - h\frac{1-\delta p}{K+h} \approx 1 - h\frac{1}{K+h} = \frac{K}{K+h} \approx KJ, \tag{3.57}$$

so equation (3.56) reduces to

$$\frac{\partial c_0}{\partial x} \sim \epsilon^2 Pe_{crit} E \Bigg(\underbrace{K J^2 c_0 \frac{\partial h}{\partial x}}_{\text{(a)}} + \underbrace{J h \frac{\partial c_0}{\partial x}}_{\text{(b)}} \Bigg). \tag{3.58}$$

As discussed in section A, the system will be in the low E regime (where the VA approximation overpredicts Δh) when film-height gradients are large enough for term (a) to be dominant. In contrast to the case of constant evaporation (figure 3.4), we do not observe a transition to the low E regime in figure 3.5 (b). This is because $K \ll 1$, so film-height gradients are not large enough to make term

(a) dominant and the system remains in the higher E regime where term (b), representing lateral concentration gradients that develop locally at the interface, is dominant. Nevertheless, we can still derive scaling relations in both the low E and higher E regimes.

Analogous to the case of constant evaporation in §A, term (b) in equation (3.58) is dominant at higher E since Δh is small and we expect $Pe_{crit} \sim E^{-1}$ as shown in figure 3.5 (b). However, the case for low E is different, and we must reconsider how h and c_0 scale with E. For mass conservation, we have $c_0 \sim 1/h$ and from equation (3.31), $J \sim 1/h$ since $K, \delta \ll 1$. Taking $\partial h/\partial x \sim \Delta h$ and $\partial c_0/\partial x \sim \Delta c$ as in §A, we have from equation (3.45)

$$\Delta c \sim \epsilon^2 Pe_{crit} \frac{E}{\Delta h^2} \quad \Rightarrow \quad \epsilon^2 Pe_{crit} \sim \frac{\Delta c \Delta h^2}{E}. \tag{3.59}$$

The scaling relation for h is given by equation (3.48), and relations (3.51) and (3.52) hold regardless of the evaporation model. However, the relation obtained from equation (3.22) is different due to a different scaling for J:

$$\frac{\Delta c}{\Delta t} \sim \frac{E}{\Delta h^3} \quad \Rightarrow \quad \Delta t \sim \frac{\Delta h^3 \Delta c}{E}. \tag{3.60}$$

Combining this with relations (3.51), (3.52) and (3.59) gives $\epsilon^2 Pe_{crit} \sim E^{-1/2}$. We

thus have the relations

$$\epsilon^2 Pe_{crit} \sim \begin{cases} E^{-1/2} & \text{low E} \\ \\ E^{-1} & \text{higher E} \end{cases} . \tag{3.61}$$

While we are unable to verify the scaling at low E numerically, it reveals that Pe_{crit} has an even weaker dependence on E under one-sided evaporation ($Pe_{crit} \sim E^{-1/2}$) than under constant evaporation ($Pe_{crit} \sim E^{-5/7}$). This is because, as discussed above, the nonuniform buildup of solute from one-sided evaporation counteracts the effects of vertical concentration gradients coupling with film-height gradients. Consequently, at very low E, we expect the VA approximation to perform well at higher Pe under one-sided evaporation ($Pe_{crit} \sim E^{-1/2}$) compared to constant evaporation ($Pe_{crit} \sim E^{-5/7}$). However, at higher E, the one-sided and constant evaporation models have the same dominant mechanism (lateral solute concentration gradients developing locally at the interface) and thus have identical scaling relations $Pe_{crit} \sim E^{-1}$.

C Diffusion-Limited Evaporation

Examining figures 3.2 (e) and (f), we note that the profiles predicted by both the 2D description and VA approximation under diffusion-limited evaporation are qualitatively similar to those under constant evaporation shown in figures 3.2 (a) and (b). However, diffusion-limited evaporation results in larger film-height perturbations. Figures 3.6 (a) and (b) show Δh for a range of Pe and two different

values of E under diffusion-limited evaporation. Comparing figure 3.6 (a) to figure 3.3 (a), we indeed see that the height perturbation Δh under diffusion-limited evaporation is larger than that under constant evaporation. This is because the evaporation rate EJ is generally slower under diffusion-limited evaporation; as solute builds up, the evaporative flux J decreases, giving a generally slower evaporation rate at a fixed value of E (compared to constant evaporation). Thus, Marangoni flow has more time to develop film-height nonuniformities which results in larger Δh.

Figures 3.6 (a) and (b) show that Δh has the same qualitative behavior as under constant evaporation shown in figure 3.3. Figures 3.6 (c) and (d) show Pe_{crit} as a function of E for the cases of low and higher E where we see that the numerical scaling relations are identical to the case of constant evaporation shown in figure 3.4. These similarities indicate that diffusion-limited evaporation qualitatively behaves like constant evaporation; observe that the evaporative flux given by equation (3.36) is smaller where the solute concentration is higher because less solvent is available at the interface. This inhibits nonuniform solute buildup because any regions of high solute concentration will experience slower evaporation, which inhibits further solute buildup. Comparing figures 3.2 (a) and (e), we indeed see that diffusion-limited evaporation results in a more uniform concentration profile (note the color bar scales). Thus, diffusion-limited evaporation given by equation (3.36) essentially becomes a spatially uniform evaporative flux $J \approx \overline{f}/\mathscr{L}$ that decreases with time as solute concentration increases.

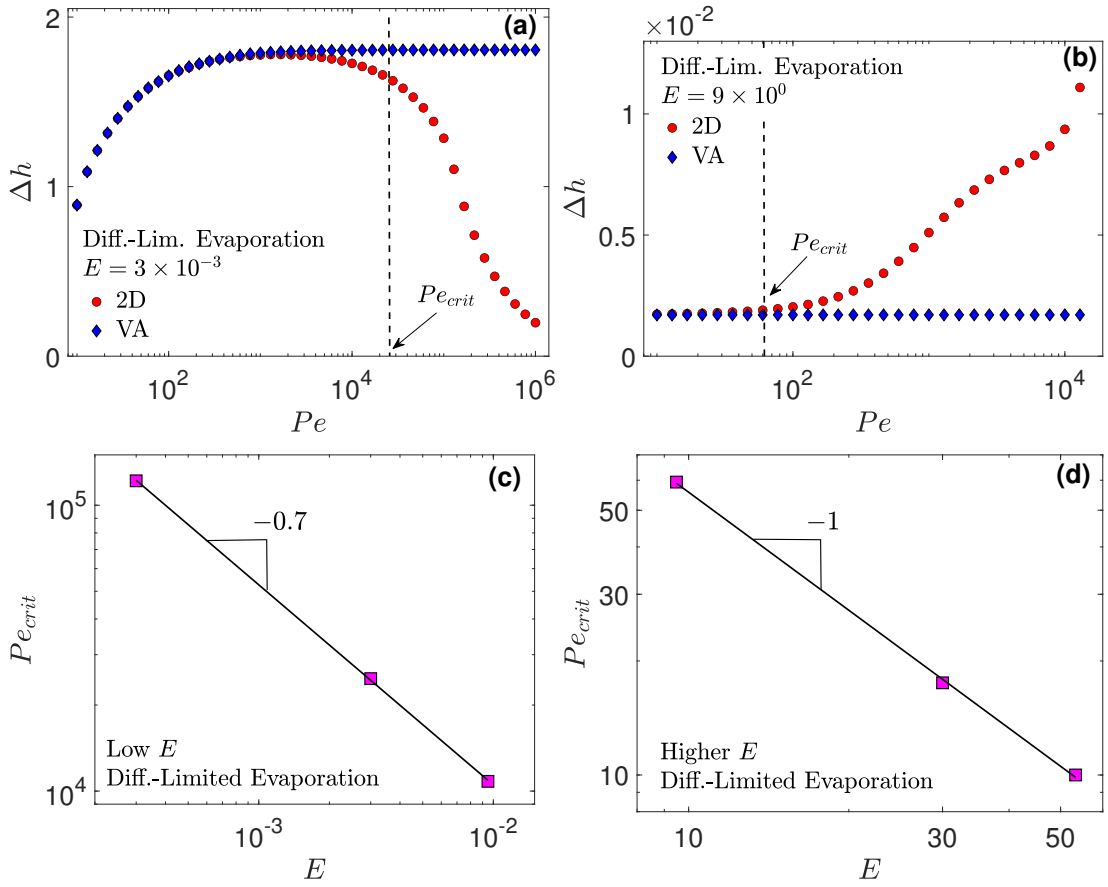

Figure 3.6: The height perturbation Δh for (a) $E = 3 \times 10^{-3}$ and (b) $E = 3 \times 10^{-2}$ for varying Pe, and Pe_{crit} at various values of E under diffusion-limited evaporation for (c) low E and (d) higher E. Note the similarities to constant evaporation in figures 3.3 and 3.4.

The time-dependence of this uniform evaporation rate does not affect the scaling relations for Pe_{crit}, since from equations (3.34) and (3.36), we have

$$\frac{\partial J}{\partial x} \approx \frac{1}{\mathscr{L}} \frac{\partial \overline{f}}{\partial x} = -\frac{\omega_0}{\mathscr{L}} \frac{\partial c|_{z=h}}{\partial x} \ll 1 \tag{3.62}$$

since $\omega_0 \ll 1$ and $c \sim O(1)$ (as shown in figure 3.2 (e)). Thus, under diffusion-limited evaporation, we expect the same scaling relations for Pe_{crit} that we saw for constant evaporation (given by equation (3.44)). However, note that the transition from low E (figure 3.6 (c)) to higher E (figure 3.6 (d)) occurs at a higher value of E than under constant evaporation (figures 3.4 (a) and (b)). This is because, as

discussed earlier, diffusion-limited evaporation results in a more uniform concentration profile. This inhibits the mechanisms that are dominant in the higher E regime since they rely on evaporation forming large lateral concentration gradients (see §A). Thus, the system remains in the low E regime, where the dominant mechanism instead depends on film-height gradients (see §A), for a larger range of E.

IV Conclusions

We have evaluated the performance of the vertical-averaging (VA) approximation under three common evaporation models — constant, one-sided, and diffusion-limited — for an evaporating, two-component thin liquid film. To focus on solutal Marangoni flow, we neglected any thermal effects induced by evaporation of solvent (discussed in §D). The model assumes the liquid is Newtonian with constant viscosity and density, that the solute is dilute, and that the Marangoni number is small. The VA approximation offers a desirable simplicity when modeling multicomponent systems that has led to its use in a wealth of previous studies. However, until this work, its limits of validity had not been systemically explored under evaporation. While the VA approximation is formally presented with the assumption $\epsilon^2 Pe \ll 1$ (for rapid vertical diffusion),[13] it was found that the necessary assumption is instead $Pe < Pe_{crit}$ where Pe_{crit} is a critical Péclet number reflecting the physical mechanisms underlying film evolution that the VA approximation fails to capture.

It was shown that Pe_{crit} depends on the evaporation model, and scaling relations were derived in §A and §B to elucidate how Pe_{crit} scales with the evaporative number E under each evaporation model. Notably, it was found that, often, $\epsilon^2 Pe_{crit} \gg 1$, and so the VA approximation "overperforms" its formal assumption $\epsilon^2 Pe \ll 1$ by several orders of magnitude. However, when $Pe > Pe_{crit}$, vertical concentration gradients from evaporation become important and it was found that the chosen evaporation model greatly influences system behavior. Vertical concentration gradients from evaporation directly inhibit film deformation if the film-height nonuniformity is large enough, but for sufficiently fast evaporation, large lateral concentration gradients form locally at the interface and cause larger film-height nonuniformities (see §A). These lateral concentration gradients near the interface become particularly pronounced under one-sided evaporation, exacerbating Marangoni stresses and causing larger film-height nonuniformities (see §B). In contrast, diffusion-limited evaporation was found to be qualitatively similar to the much simpler case of constant evaporation because any nonuniformity in the evaporative flux is self-inhibiting (see §C).

While the VA approximation overperforms relative to its formal assumptions, one must be cognizant of the value of $\epsilon^2 Pe$ when employing the VA approximation, and also how the chosen evaporation model may qualitatively influence results. If the VA approximation is used outside of its range of validity, film-height and solute-concentration contours should be interpreted with caution. For systems at large Pe, it is best to use a 2D description for species distribution and it is crucial to accurately characterize evaporation. Scaling relations (3.54) and (3.61) provide

guidelines for what a large value of Pe is.

Chapter 4

Comparison of One-Sided and Diffusion-Limited Evaporation Models for Thin Liquid Droplets*

I Introduction

The drying of sessile liquid droplets has applications in numerous industrial processes and natural phenomena. While the geometry of a droplet resting on a solid surface appears simple (figure 4.1), the coupling of contact-line dynamics to evaporation makes the problem difficult to study. Industrial applications include inkjet printing,[7] lab-on-a-chip devices, spray coating, and forensic analysis.[8] In nature, drying sessile droplets allow sweat to cool our bodies, but also lead to complex phenomena such as the coffee-ring effect.[11] Thus, the study of drying droplets is a large, multidisciplinary field that has been approached experimentally, theoret-

*This work has been submitted for publication.

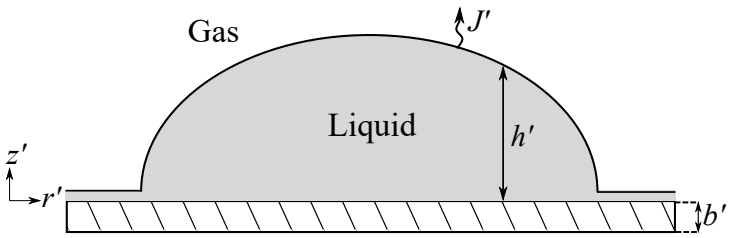

Figure 4.1: Schematic of an axisymmetric liquid droplet with thickness $h'(r', t')$ resting on a solid substrate with constant thickness b'. The solid is heated to a temperature T_b on its bottom face and the liquid evaporates with a spatially non-uniform evaporative flux J'. The substrate is assumed to be covered by a thin liquid precursor film.

ically, and numerically in order to develop fundamental understanding.

When modeling drying droplets, there are two fundamental complications that arise. The first complication is ameliorating motion of the three-phase contact-line with a no-slip condition at the solid substrate. There are several approaches to this,[86] and in the present work we will use a precursor-film approach where the solid substrate is covered by a thin liquid film as depicted in figure 4.1. This lifts the contact line up from the solid, allowing it to move while still enforcing no-slip conditions at the liquid-solid interface. The liquid pressure is modified to account for van der Waals forces that control droplet spreading and also prevent the precursor film from evaporating. Such films have been observed experimentally[87] and result in governing equations that are easier to solve than those obtained from alternative approaches.[88] The second complication is modeling the evaporation process, which proceeds through two main steps: Liquid first undergoes phase change into vapor and is then transported away from the liquid-gas interface into the surroundings.

Existing models for evaporation are largely distinguished by which of the two steps is assumed to be rate limiting. The two predominant evaporation models

are the one-sided model, which assumes phase-change is rate limiting, and the diffusion-limited model, which assumes diffusive transport of vapor is rate limiting. Both have been widely used in previous work, but have vastly different formulations as will be discussed in §A and §B. It is often unclear *a priori* which evaporation model is most appropriate for a physical system, and understanding of the fundamental differences between evaporation models is lacking. We seek to develop this understanding in the present work, so we begin with an overview of each evaporation model and their use in previous work.

A One-Sided Evaporation

The one-sided (or non-equilibrium one-sided (NEOS)) evaporation model assumes that evaporation is rate-limited by the phase change to vapor and that the liquid is evaporating into its own saturated vapor. One-sided evaporation is driven by deviations from saturated conditions and its description was pioneered by Schrage[89] using the kinetic theory of gases. The term "one-sided" is used because the transport problem in the liquid decouples from that in the gas and one obtains an analytical expression for the evaporative flux by considering only transport in the liquid (similar to that of a simple mass-transfer-coefficient model).[20] This is typically done in the context of lubrication theory (thin droplets), yielding an evolution equation without any other assumptions on the droplet shape. At its edge, the droplet merges onto a precursor film of constant thickness that does not evaporate away due to the inclusion of disjoining pressure.

Predictions from models using one-sided evaporation agree well with experi-

ments of droplets evaporating in saturated conditions,[63] and can fit experimental data even when the gas phase is not saturated vapor.[82] This agreement, along with its simplicity, has led to one-sided evaporation being used in a number of theoretical studies of evaporating droplets as well as films.[10,15,33,58,65–67,90–92]

B Diffusion-Limited Evaporation

The diffusion-limited evaporation model assumes that diffusive transport of vapor away from the liquid-air interface is the rate-limiting step. Furthermore, it assumes that the liquid is in equilibrium with the vapor directly above it, establishing a relation between the thermodynamic states of the liquid and the gas (e.g., the Kelvin equation). Consequently, one must solve transport problems for both the liquid and gas phases that are coupled by the equilibrium condition and evaporative flux at the liquid-air interface. While diffusion-limited evaporation is often implemented without a precursor film, one can be included. Distinct from one-sided evaporation, the precursor film under diffusion-limited evaporation has a thickness that decays to a nonzero value inversely with distance from the droplet contact line.[17]

If evaporation is slower than the relaxation time of the droplet, capillary pressure will bring the droplet to a spherical-cap shape. With a spherical-cap droplet, diffusion-limited evaporation yields simple expressions for the evaporative flux and time-evolution of the droplet radius (sometimes referred to as the "lens" evaporation model).[11,74,75,93] These expressions impart a great deal of physical insight that has been leveraged to develop fundamental understanding. For example, one

can fit experimental measurements of the droplet radius to simple analytical expressions to obtain estimates of the evaporative flux profile and total evaporation rate.[94] Furthermore, knowledge of the structure of the evaporative flux near the contact line allows one to understand and derive expressions for apparent contact angles and thermal gradients (and thus Marangoni flow) in terms of simple physical parameters.[83,95,96]

Diffusion-limited evaporation often well-approximates evaporation rates observed in simple drying-droplet experiments, so it is has been attractive for both experimental and theoretical studies (usually assuming a spherical-cap droplet)[17,18,76,81,83,94,96–104] and has also been used to model drying films.[58,59,70,72]

C Overview of Present Paper

While both one-sided and diffusion-limited evaporation have been widely used in previous studies, few have compared them.[22,71,82] Most notably, Murisic and Kondic[82] directly compared one-sided and diffusion-limited evaporation by fitting predictions to experimental data for evaporating sessile droplets. They found that agreement of each model with experiment depended on the physical system (e.g., water versus isopropanol droplets), attributing the differences to inaccurately predicted thermal Marangoni flow. However, it is difficult to extract understanding of the fundamental differences between the evaporation models because Murisic and Kondic[82] assume spherical-cap droplets, do not isolate thermal effects, and fit their model predictions to experimental data with widely varying droplet lifetimes. Thus, in this work we will develop a more general understanding of each evapo-

ration model and the fundamental differences between them for a given droplet lifetime. We will then show how these fundamental differences give rise to inaccurately predicted thermal gradients for some physical systems but not others (as observed by Murisic and Kondic[82]).

First, the mathematical model is presented in §II. Next, in §III we highlight a novel hybrid spectral-finite-difference method we have developed to solve the governing equations and the challenges it overcomes. Because the two models exhibit significant differences in evaporation behavior, we discuss the droplet-lifetime-matching procedure in §IV. Direct comparisons without thermal effects are given in §V. In §VI, we show that thermal Marangoni flow is always directed away from the contact line under one-sided evaporation, in contrast to diffusion-limited evaporation where it is known that the direction depends on the liquid/solid thermal conductivity ratio.[83] Conclusions are given in §VII.

II Mathematical Model

We consider a thin, axisymmetric droplet of pure solvent as depicted in figure 4.1. The droplet height is given by $h'(r', t')$ where r' is the radial coordinate and t' is time. The evaporative flux $J'(r', t')$, in general, also varies with space and time.

A Hydrodynamics

The liquid is Newtonian with density ρ, viscosity μ, and surface tension σ'. The ratio of the vertical and lateral characteristic length scales, given by the initial

height H and radius L of the droplet, $\epsilon = H/L \ll 1$, is assumed small so that lubrication theory may be leveraged. The liquid motion is subject to no-slip and no-penetration conditions at the solid substrate and stress balances at the liquid-gas interface.

We use the scale $p^* = \sigma_0\epsilon^2/H$ for the pressure p', $v_r^* = \epsilon^3\sigma_0/\mu$ for the r-velocity v_r', $v_z^* = \epsilon v_r^*$ for the z-velocity v_z', and $t^* = H/v_x^*\epsilon$ for the time t'. These scales are derived from balancing terms in the mass and momentum balances.[24] The quantity σ_0 is the surface tension at the saturation temperature T_s and is used to scale σ'. Finally, for the evaporative flux J', we use a general scale J^* (defined in §B) and nondimensionalize the temperature T' as $T = (T' - T_s)/(T_b - T_s)$ where $T_b > T_s$ is the temperature of the heated substrate. For the remainder of this work, we use dimensionless variables (indicated without a prime superscript):

$$r' = \epsilon^{-1}Hr, \qquad z' = Hz, \qquad h' = Hh, \qquad T' = (T_b - T_s)T + T_s,$$

$$v_x' = v_x^* v_x, \qquad v_z' = \epsilon v_x^* v_z, \qquad p' = p^* p, \qquad t' = t^* t, \qquad J' = J^* J. \tag{4.1}$$

Surface tension σ is assumed to vary linearly with the dimensionless interface temperature $T_I = T|_{z=h}$,

$$\sigma = 1 - \epsilon^2 Ma T_I, \tag{4.2}$$

where the Marangoni number $Ma = (\partial\sigma'/\partial T')\,(T_b - T_s)/\sigma_0\epsilon^2$.

Under the lubrication approximation, the Navier-Stokes equations become

$$\frac{\partial^2 v_r}{\partial z^2} = \frac{\partial p}{\partial r}, \tag{4.3}$$

$$\frac{\partial p}{\partial z} = 0, \tag{4.4}$$

$$\frac{1}{r}\frac{\partial}{\partial r}\left(r v_r\right) + \frac{\partial v_z}{\partial z} = 0, \tag{4.5}$$

with the boundary conditions $v_r = v_z = 0$ at $z = 0$ and

$$p = -\frac{1}{r}\frac{\partial}{\partial r}\left(r\frac{\partial h}{\partial r}\right) - \Pi, \tag{4.6}$$

$$\frac{\partial v_r}{\partial z} = -Ma\frac{\partial T_I}{\partial r}, \tag{4.7}$$

at $z = h$, where Π is the disjoining pressure.

As stated, the no-slip condition imposed at the substrate does not allow for contact-line motion. There are several approaches to ameliorating this, and in this work we use a precursor-film approach because the resulting equations are much easier to solve.[86,88] It is assumed that the substrate is covered with a thin precursor film and the liquid pressure is modified with a disjoining pressure to account for van der Waals interactions. As in previous work,[15,65,82,91,105,106] we use a two-term disjoining pressure that includes both attractive and repulsive interactions,

$$\Pi(h) = A_1\left(\left(\frac{A_2}{h}\right)^3 - \left(\frac{A_2}{h}\right)^2\right), \tag{4.8}$$

where A_1 is a dimensionless Hamaker constant and A_2 controls the thickness at which the disjoining pressure vanishes. The constants A_1 and A_2 also control the scaled equilibrium contact angle θ_{eq} through the relation[105]

$$\theta_{eq} \approx \sqrt{A_1 A_2}. \tag{4.9}$$

This is related to the lab-frame contact angle θ'_{eq} by $\theta'_{eq} \approx \epsilon\theta_{eq}$. The precursor-film thickness h_p is determined by the condition $J(h_p) = 0$ which will be discussed in §1 and §2. We have found that using a one-term attractive model for Π (corresponding to a perfectly wetting fluid) results in smaller apparent contact angles, but does not qualitatively change the findings presented in this work.[17,66,92,100]

Solving equations (4.3) and (4.4) subject to boundary conditions (4.6) and (4.7) yields the radial velocity

$$v_r = \left(\frac{1}{2}z^2 - hz\right)\frac{\partial p}{\partial r} - zMa\frac{\partial T_I}{\partial r}. \tag{4.10}$$

Finally, mass conservation at the interface $z = h$ coupled with continuity equation (4.5) gives the kinematic condition governing the film height

$$\frac{\partial h}{\partial t} = -\frac{1}{r}\frac{\partial}{\partial r}\int_0^h r v_r \,\mathrm{d}z - EJ = \frac{1}{3r}\frac{\partial}{\partial r}\left(rh^3\frac{\partial p}{\partial r}\right) + \frac{Ma}{2r}\frac{\partial}{\partial r}\left(rh^2\frac{\partial T_I}{\partial r}\right) - EJ, \tag{4.11}$$

where the pressure p is given by equation (4.6), the evaporative number $E = J^*/\epsilon\rho v_r^*$ (the ratio of evaporative and convective fluxes), and specific expressions for the evaporative flux J will be given in §C. This equation is subject to the sym-

metric boundary condition $h(r) = h(-r)$ as well as matching onto the precursor film $h \to h_p$ as $r \to \infty$.

B Energy Transport

The solid substrate is held at a constant dimensionless temperature $T = 1$ on its bottom face at $z = -b$, where $b = b'/H$ is the thickness of the solid substrate. The solid and liquid have thermal conductivities k_s and k_ℓ, respectively. Because the droplet is thin, the temperature is governed by

$$\frac{\partial^2 T}{\partial z^2} = 0 \tag{4.12}$$

in both phases and subject to the boundary conditions

$$T|_{z=-b} = 1, \qquad T|_{z=h^-} = T|_{z=h^+}\,, \tag{4.13}$$

$$\left.\frac{\partial T}{\partial z}\right|_{z=h^-} = \frac{\kappa}{b}\left.\frac{\partial T}{\partial z}\right|_{z=h^+}, \qquad -\left.\frac{\partial T}{\partial z}\right|_{z=h} = J, \tag{4.14}$$

where $\kappa = bk_\ell/k_s$ is a scaled thermal conductivity ratio and we use the evaporative flux scale $J^* = \Delta T' k_\ell / L_m H$, where L_m is the latent heat of vaporization.

Solving these equations yields the temperature field

$$T = \begin{cases} 1 - \kappa J\left(1 + \frac{z}{b}\right) & -b \le z < 0 \\ 1 - J\left(z + \kappa\right) & 0 \le z \le h \end{cases}. \tag{4.15}$$

Of chief concern is the temperature at the liquid-air interface,

$$T_I = T|_{z=h} = 1 - J(h + \kappa), \tag{4.16}$$

which depends on the evaporative flux J, the film height h, and the conductivity ratio κ.

C Evaporation

We now present expressions for the evaporative flux J that appears in equations (4.11) and (4.16) for both one-sided and diffusion-limited evaporation.

1 One-Sided Evaporation

The one-sided evaporation model gives a constitutive relation for the evaporative flux J, which is (in nondimensional form)[33,92]

$$KJ = \delta p + T_I, \tag{4.17}$$

where

$$K = \frac{k_\ell \sqrt{2\pi R_g T_s^3}}{\rho_v L_m^2 \alpha H}, \qquad \delta = \frac{p^* T_s}{\rho L_m \Delta T}. \tag{4.18}$$

Here, R_g is the ideal gas constant, ρ_v is the density of the vapor, and α is the accommodation coefficient. The parameter K gives a measure of kinetic effects and the volatility of the liquid, and can be interpreted as the inverse of an effective mass-transfer coefficient.[20,92] The parameter δ measures the effect of changes in

local pressure on the phase-change temperature.[92] Substituting equation (4.16) into equation (4.17) yields the one-sided evaporative flux

$$J = \frac{1 + \delta p}{K + h + \kappa} \tag{4.19}$$

which is an explicit, local function of the film height h.

The precursor-film thickness h_p is determined by the condition $J = 0$ for a flat film. With the pressure given by equation (4.6), equation (4.19) reduces to finding the roots of a cubic polynomial:

$$0 = 1 + \delta p = 1 - \delta\Pi(h_p) \quad \Rightarrow \quad 0 = h_p^3 + \delta A_1 A_2^2 h_p - \delta A_1 A_2^3. \tag{4.20}$$

The discriminant of this polynomial is negative, and thus the single real root is

$$h_p = 2A_2\sqrt{\frac{\delta A_1}{3}}\sinh\left[\frac{1}{3}\text{asinh}\left(\frac{3}{2}\sqrt{\frac{3}{\delta A_1}}\right)\right]. \tag{4.21}$$

This relation is used to determine the precursor-film thickness in the initial condition to the numerical method described in §III when using one-sided evaporation.

2 Diffusion-Limited Evaporation

Under diffusion-limited evaporation, the evaporative flux J is determined by the diffusive flux of vapor at the liquid-air interface $z = h$. It has been shown that in many scenarios, transient effects as well as convection are negligible in the gas phase,[18] so the transport problem reduces to pseudo-steady-state diffusion. The

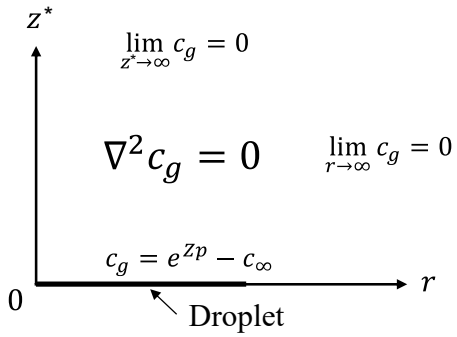

Figure 4.2: Schematic of the vapor concentration c_g problem in the semi-infinite domain $r \in (0, \infty)$ and $z^* \in (0, \infty)$. The thin liquid droplet (and precursor film) is in thermodynamic equilibrium with the vapor phase, so we use the Kelvin equation to describe c_g at $z^* = 0$.

droplet interface is assumed to be in thermodynamic equilibrium, allowing us to relate the thermodynamic states of the liquid and gas phases.

Figure 4.2 depicts the problem for the dimensionless gas-phase concentration c_g above the droplet. We use the vertical coordinate $z^* = z'/L$ since there is no apparent vertical scale (unlike inside the droplet) and c_g is defined on the semi-infinite domain $z^* \in (\epsilon h, \infty)$ and $r \in (0, \infty)$. Because the droplet is thin and $\epsilon h \ll 1$, we can neglect the droplet height and instead use the constant domain $z^* \in (0, \infty)$ (shown formally in the appendix). It is assumed that the vapor is at an ambient concentration c_∞ far from the droplet, so we nondimensionalize c_g' as $c_g = (c_g' - c_\infty')/c_s$ where c_s is the concentration of saturated vapor. We then have $c_g \to 0$ as $r \to \infty$ or $z^* \to \infty$ as shown in figure 4.2.

The governing equation for c_g is

$$0 = \boldsymbol{\nabla}^2 c_g = \frac{\partial^2 c_g}{\partial z^{*2}} + \frac{1}{r}\frac{\partial}{\partial r}\left(r\frac{\partial c_g}{\partial r}\right). \tag{4.22}$$

For boundary conditions in r, we have the symmetric boundary condition $c_g(r) =$

$c_g(-r)$ and matching to the ambient concentration $c_g \to 0$ as $r \to \infty$. In z^*, we also match to the ambient concentration as $z^* \to \infty$ and then enforce thermodynamic equilibrium with the liquid droplet at $z^* = 0$. For this, we use the Kelvin equation which accounts for the effect of interface curvature and disjoining pressure on thermodynamic equilibrium:[17]

$$c_g|_{z^*=0} = e^{Zp} - c_\infty, \tag{4.23}$$

where $c_\infty = c'_\infty/c_s < 1$, $Z = Mp^*/\rho R_g T$ is an effective compressibility factor, and M is the molecular weight of the liquid.

To obtain the evaporative flux J, we employ Fick's law so that

$$J = -\frac{J^*_D}{J^*} \left.\frac{\partial c_g}{\partial z^*}\right|_{z^*=0} \tag{4.24}$$

where $J^*_D = c_s D\epsilon/H$ is the evaporative-flux scale arising from diffusion (opposed to J^* from energetic considerations) and D is the diffusivity of the vapor. For the purpose of this work, we assume the ratio J^*_D/J^* to be near unity and neglect it, but in practice it may be absorbed into the evaporative number E without loss of generality. A noteworthy result is the analytical solution for J developed by Eggers and Pismen;[17] considering a problem analogous to that shown in figure 4.2, they showed that (in the current notation)

$$J(r) = -\int_0^\infty \mathcal{K}(r, r') \frac{\partial c_g|_{z^*=0}}{\partial r'} \, \mathrm{d}r' \,, \tag{4.25}$$

where the kernel $\mathcal{K}$ involves the complete elliptic integrals of the first and second kind. As will be discussed in §III, we have found numerical solution of equations (4.22) and (4.24) to be more stable in our nonlinear simulations, but the analytical results encapsulated in equation (4.25) offer valuable insight into the behavior of c_g and J and will be leveraged in §III. Furthermore, equation (4.25) demonstrates that J is a global function of h – distinct from the local function of h obtained under one-sided evaporation (equation (4.19)).

The precursor-film thickness h_p is determined by $J = 0$, which is equivalent to $c_g|_{z^*=0} = 0$ so that there is no driving force for vertical diffusion. Equation (4.23) then yields the cubic equation

$$0 = h_p^3 + \frac{ZA_1A_2^2}{-\ln c_\infty} h_p - \frac{ZA_1A_2^3}{-\ln_\infty} \tag{4.26}$$

which is equivalent to equation (4.20) with δ replaced by $Z/-\ln c_\infty$ (note that $c_\infty < 1$). Thus, through the same method employed to obtain equation (4.21), we obtain

$$h_p = 2A_2\sqrt{\frac{ZA_1}{-3\ln c_\infty}}\sinh\left[\frac{1}{3}\text{asinh}\left(\frac{3}{2}\sqrt{-\frac{3\ln c_\infty}{ZA_1}}\right)\right]. \tag{4.27}$$

This relation is used to determine the precursor-film thickness in the initial condition to the numerical method described in §III when using diffusion-limited evaporation.

Table 4.1: Important dimensionless parameters and typical values.

Parameter	Definition	Physical Meaning	Typical Values
Ma	$\Delta\sigma/\sigma_0\epsilon^2$	Marangoni forces/surface-tension forces	10^{-3}-10^{-1}
E	$J^*\mu/\rho\sigma_0\epsilon^4$	evaporative flux/convective flux	$10^{-4}-10^{-1}$
κ	$b'k_\ell/Hk_s$	liquid conductivity/solid conductivity	$0-1$

D Parameter Values

The effects of the key dimensionless groups shown in table 4.1 will be investigated in §V and §VI. The remaining parameters, A_1 and A_2 for the disjoining pressure, δ and K for one-sided evaporation, and Z and c_∞ for diffusion-limited evaporation, are fixed for the remainder of this work. The constants $A_1 = 10^2$ and $A_2 = 10^{-3}$ are chosen close to those used in previous work[65,107] and give a scaled equilibrium contact angle of $\theta_{eq} \approx 18^\circ$ (equation (4.9)). Following Murisic and Kondic,[82] we choose $K = 10$ and $\delta = 10^{-3}$ (determined by fitting predictions to experimental measurements of evaporating water droplets) giving $h_p \approx 3.9 \times 10^{-4}$. As will be discussed in §IV, we choose $Z = 7.69 \times 10^{-5}$ and $c_\infty = 9.26 \times 10^{-1}$ to match the total evaporation time as well as h_p under diffusion-limited evaporation.

III Numerical Method

Equations (4.11) and (4.22) are numerically solved from the initial condition

$$h(t=0,r) = \begin{cases} h_p + (h_0 - h_p)\left(1 - \left(\frac{r}{R_0}\right)^2\right) & r \leq R_0 \\ h_p & r > R_0 \end{cases}, \tag{4.28}$$

which represents an initially parabolic droplet with height h_0 and radius R_0. In this work, we fix $h_0 = 2$ and $R_0 = 1$ since the droplet rapidly relaxes to an equilibrium shape before significant evaporation occurs. For equation (4.11) (excepting the evaporative flux J), we use a second-order centered finite-difference method.[108] To compute J under each evaporation model, we use the methods described in §A and §B.

A One-Sided Evaporative Flux

Under one-sided evaporation, J given by equation (4.19) is an explicit, local function of the liquid thickness h and is thus easily computed alongside the finite-difference method used to solve equation (4.11). There are no additional numerics required.

B Diffusion-Limited Evaporative Flux

Under diffusion-limited evaporation, J is obtained from the solution of equation (4.22) and is thus an implicit, global function of h (see equation (4.25)). When approached numerically, equation (4.22) is commonly solved with a finite-element method,[76,101,102,109] but many analytical simplifications have been developed. Eggers and Pismen derived equation (4.25), which removes the necessity of solving a PDE at each time step. However, the kernel $\mathcal{K}$ is ill-conditioned and singular at $r' = r$, so computation of the integral is numerically complex and prone to error that can induce instability in the time-stepping algorithm. An alternative is to assume that the droplet is a spherical cap, in which case the evaporative flux is

given by

$$J = \frac{2}{\pi} \frac{1 - c_\infty}{\sqrt{R^2 - r^2}}, \tag{4.29}$$

which removes any numerical complications when computing the evaporative flux (note that a similar approximation can also used for non-thin droplets).[11] Equation (4.29) is simple and useful for gaining physical insight, so we will reference it when discussing our results. However, we seek to develop understanding for more general droplet shapes, so to compute J in our nonlinear simulations, we solve equation (4.22) using the novel hybrid spectral-finite-difference method detailed below.

Since the value of h is required in the equilibrium boundary condition for c_g (equation (4.23)), it is convenient to choose the same discretization for r for both equations (4.11) and (4.22) (second-order centered finite-differences). This necessitates a finite r domain despite the boundary conditions for equation (4.22) as $r \to \infty$. It has been shown that, away from the contact line, h decays to the precursor-film thickness as $1/r$,[17] so an r domain that is significantly larger than the droplet radius is required to properly resolve the evaporative flux. We choose $r \in (0, 100)$ because scaling relations,[17] as well as numerical results from our simulations, show that this is adequate to resolve the evaporative flux within numerical tolerances.

We must also discretize equation (4.22) in the z^* domain. It is possible to similarly choose a finite distance[70,109] and solve in a truncated z^* domain by finite-elements or finite-differences. However, unlike the r domain, the proper distance in the z^* domain is unclear. Furthermore, we are not restrained by boundary data

as in the r domain, so it is possible to use a different discretization that is capable of resolving semi-infinite domains. Thus, we use a spectral method in z^* with Laguerre basis functions on the domain $z^* \in (0, \infty)$. The Laguerre functions[50] $L_n(z^*)$ are a modification of the Laguerre polynomials[110] $\ell_n(z^*)$ to a semi-infinite domain:

$$L_n(z^*) = e^{-z^*/2}\ell_n(z^*). \tag{4.30}$$

We choose these basis functions over other candidates because they decay exponentially, which matches the exponential decay of c_g shown by Eggers and Pismen.[17]

This hybrid spectral-finite-difference method represents the gas-phase concentration as the expansion

$$c_g(r, z^*, t) \approx \sum_{n=0}^{M-1} a_n(r, t) L_n(z^*) \tag{4.31}$$

where the coefficients a_n depend on r and t. Inserting this into equation (4.22) and applying orthogonality of the Laguerre functions gives the PDE

$$a_n'' + \frac{1}{r}\frac{\partial}{\partial r}\left(r\frac{\partial a_n}{\partial r}\right) = 0, \tag{4.32}$$

for each n, where $a_n''(a_1, ..., a_n)$ gives the coefficients of the second z^*-derivative of c_g. This PDE can be further discretized in r with the same finite-difference method and solved for a_n alongside equation (4.11). The evaporative flux is then

obtained from the relation

$$J(r,t) = -\sum_{n=0}^{M-1} a_n'(r,t), \tag{4.33}$$

which follows from the identity $L_n(0) = 1$. Here, a_n' are the coefficients of the first z^*-derivative of c_g.

The end result of this numerical method is the reduction of equation (4.22) to an $NM \times NM$ banded system of equations with bandwidth $4M$, where M is the number of Laguerre functions and N is the number of finite-difference cells, that is efficiently solved by standard banded-system solvers. This requires similar computational time and memory to a full finite-difference/element method, but is capable of resolving the entire semi-infinite domain with spectral accuracy in z^*. To the best of our knowledge, this is the first numerical method to employ Laguerre functions in the context of evaporation. See the supplementary material for a detailed discussion of implementing this method.

For accuracy, we must have high resolution near the droplet contact line. However, this level of resolution is not necessary far from the droplet. Thus, near the droplet, we use cells with constant width, but those far from the droplet become wider. Formally, the cells at a radius less than a critical radius, $r < r_c$, have constant width, and each cell beyond r_c is a factor c wider than the previous. For a given number of nodes N, the number of nodes inside the critical radius N_i is given by

$$N_i = -\alpha + \frac{1}{\ln c}\mathrm{W}(\alpha c^{N+\alpha} \ln c), \tag{4.34}$$

where $\alpha = cr_c/(c-1)(d-r_c)$, d is the size of the r domain, and W is the principal branch of the Lambert-W function.[111] In this work, we use $r_c = 2$, $c = 1.05$, $d = 100$, and $N = 4000$ nodes, giving $N_i \approx 3807$. This approach covers the entire domain $r \in (0, 100)$ with only minor cell stretching while placing over 95% of the cells near or inside the droplet ($r < 2$).

This hybrid-spectral-finite-difference method also allows computation of the vapor field c_g above the droplet, whereas direct expressions for J such as equations (4.25) and (4.29) provide no information about c_g. Figure 4.3 shows c_g above a droplet with radius $R \approx 1.4$ (located at $z^* = 0$) where we present z^* on a logarithmic scale to show that the vapor concentration c_g decays exponentially. Vapor is concentrated near the droplet at $z^* = 0$ and approaches the scaled ambient value $c_g = 0$ as $z^* \to \infty$ or $r \to \infty$. Note that establishing this vapor field is critical to the diffusion-limited evaporation model; processes such as convection can interfere and cause the diffusion-limited model to become inaccurate.[94] As will be discussed in §V, one-sided evaporation may offer a more accurate description in such a scenario.

IV Evaporation Time Matching

In this section we develop expressions for the droplet lifetime under diffusion-limited and one-sided evaporation. By equating these expressions, we obtain relations between parameters that ensure a consistent droplet lifetime between the two evaporation models.

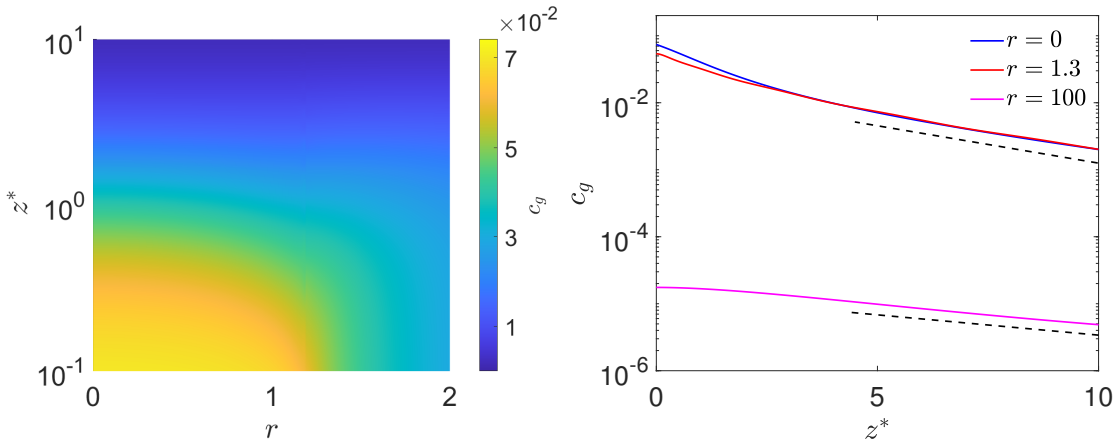

Figure 4.3: (a) Example of the vapor concentration c_g above the droplet (located at $z^* = 0$). (b) Plots of the vapor concentration c_g at fixed r. Straight dashed lines are provided for reference to show c_g decays exponentially ($\ln c_g \sim z^*$) for sufficiently large z^*.

To begin, we integrate equation (4.11) over the droplet radius to obtain

$$\frac{\mathrm{d}}{\mathrm{d}t}\int_0^R rh\,\mathrm{d}r = -E\int_0^R rJ\,\mathrm{d}r\,. \tag{4.35}$$

Note that this equation is simply conservation of volume, balancing the change in droplet volume with the total evaporation rate. For simplicity, we assume in this derivation that the droplet shape is a spherical cap given by

$$h(r,t) = \frac{R(t)}{2}\tan\theta_a\left(1-\left(\frac{r}{R(t)}\right)^2\right), \tag{4.36}$$

where θ_a is the apparent contact angle (assumed constant). We then have the volume-change

$$\frac{\mathrm{d}}{\mathrm{d}t}\int_0^R rh\,\mathrm{d}r = \frac{3}{8}R^2\tan\theta_a\frac{\mathrm{d}R}{\mathrm{d}t}. \tag{4.37}$$

Under diffusion-limited evaporation with a spherical-cap droplet, we have

$$J_{tot} = \int_0^R rJ \,\mathrm{d}r = \frac{2(1-c_\infty)}{\pi} \int_0^R \frac{r}{\sqrt{R^2 - r^2}} \,\mathrm{d}r = \frac{2}{\pi} R(1-c_\infty), \tag{4.38}$$

where we substituted equation (4.29) for J. It is known that the total evaporation rate for diffusion-limited evaporation is proportional to the droplet radius;[11,94] here, we see that the constant of proportionality is $2(1-c_\infty)/\pi$ in equation (4.38). Inserting equation (4.37) and (4.38) into equation (4.35) and integrating gives the relation

$$R(t) = \sqrt{C_d \left(t_0^{(d)} - t\right)}, \tag{4.39}$$

where $C_d = 32E(1-c_\infty)/3\pi \tan\theta_a$ and $t_0^{(d)}$ is the droplet lifetime for diffusion-limited evaporation ($R(t_0^{(d)}) = 0$). With an initial radius $R_i = R(t=0)$, we can solve for $t_0^{(d)}$:

$$t_0^{(d)} = \frac{R_i^2}{C_d} = \frac{3\pi}{32} \frac{R_i^2 \tan\theta_a}{E(1-c_\infty)}. \tag{4.40}$$

When dimensionalized (accounting for the factor J_D^*/J^* discussed in §2), this expression is equivalent to that shown in Ref. 11.

Under one-sided evaporation, with equation (4.36) for h, we have the total evaporation rate

$$J_{tot} = \int_0^R rJ \,\mathrm{d}r = \int_0^R \frac{r}{K + h + \kappa} \,\mathrm{d}r = \frac{R}{\tan\theta_a} \ln\left(1 + \frac{R\tan\theta_a}{2\,(K+\kappa)}\right), \tag{4.41}$$

where we have neglected the pressure contribution in equation (4.19) for J. Substituting equation (4.37) and (4.41) into equation (4.35) and integrating gives the

relation

$$\mathrm{li}\left((1+\Gamma)^2\right) - \mathrm{li}\,(1+\Gamma) - \ln 2 = \frac{2E}{3(K+\kappa)^2}(t_0^{(o)} - t), \tag{4.42}$$

where li is the logarithmic integral function,[110] $\Gamma = R\tan\theta_a/2(K+\kappa)$, and $t_0^{(o)}$ is the droplet lifetime under one-sided evaporation. While this expression is complicated and implicit in the droplet radius R, it will be shown in §V that with $\Gamma \ll 1$, it reduces to a linear dependence $R \sim t_0^{(o)} - t$.

By equating $t_0^{(d)}$ from equation (4.40) and $t_0^{(o)}$ from equation (4.42), we obtain an expression for c_∞ in terms of parameters from the one-sided evaporation model,

$$\frac{1}{1-c_\infty} = \frac{4}{\pi}\frac{\tan\theta_a}{\Gamma_i^2}\left[\mathrm{li}\left((1+\Gamma_i)^2\right) - \mathrm{li}\,(1+\Gamma_i) - \ln 2\right], \tag{4.43}$$

where $\Gamma_i = R_i\tan\theta_a/2(K+\kappa)$. Note that this assumes a spherical-cap droplet and constant θ_a. Furthermore, c_∞ from equation (4.43) depends on the initial radius of the droplet R_i since the two evaporation models have different dependencies on the droplet radius (equations (4.38) and (4.41)). Relation (4.43) thus serves as starting point for time matching, where given K, R_i, and an approximate θ_a (e.g., from numerical results), an initial estimate for c_∞ can be obtained. The parameter Z (see equation (4.23)) is then obtained from the relation

$$Z = -\delta \ln c_\infty \tag{4.44}$$

that ensures equations (4.21) and (4.27) yield the same precursor film thickness h_p.

As discussed in §D, all results presented use $K = 10$, $\delta = 10^{-3}$, and $E = 10^{-2}$ which was found by Murisic and Kondic[82] to well-approximate evaporating water droplets. These parameters result in an evaporation time of $t_0^{(o)} \approx 630$ in the nonlinear simulations with one-sided evaporation. From equations (4.43) and (4.44), we then obtain $c_\infty \approx 9.38 \times 10^{-1}$ and $Z \approx 6.4 \times 10^{-5}$ for diffusion-limited evaporation. While close, these parameters do not give exactly the same evaporation time due to the assumptions used to obtain equations (4.43) and (4.44). Thus, we iteratively adjust c_∞ and Z from the initial guess provided by equations (4.43) and (4.44) until we obtain $t_0^{(d)} \approx t_0^{(o)} \approx 630$; we found that $c_\infty = 9.26 \times 10^{-3}$ with $Z \approx 7.69 \times 10^{-5}$ achieves this. Remarkably, the value of c_∞ predicted by equation (4.43) was within 1% of the value required for time-matching in the full nonlinear simulations.

Because we are concerned with comparing one-sided and diffusion-limited evaporation and not the specific behavior of a single model, we do not present the effects of varying K, δ, Z, or c_∞ in this work. They do not qualitatively change the comparisons presented in §V and §VI, and many studies have investigated each model in isolation (see the discussion in §I). However, we will investigate the effect of varying E in §V because it accentuates the models' fundamental differences.

V Comparison of Droplet Radius and Contact Angle

In this section, we make direct comparisons between predictions of the droplet radius and contact angle under one-sided and diffusion-limited evaporation. We begin by discussing the main qualitative features of predictions from each evaporation model. Figure 4.4 (a) shows an example of the droplet height evolution under diffusion-limited evaporation; the droplet rapidly spreads out from the initial radius $R_0 = 1$ (not shown) and then begins to retract as evaporation proceeds. The droplet profile under one-sided evaporation is qualitatively similar. Figure 4.4 (b) shows the evaporative flux J halfway through the droplet lifetime, $t = t_0/2$, for both one-sided and diffusion-limited evaporation. Note that the one-sided evaporative flux (red line) is nearly constant throughout the droplet and rapidly decays to $J = 0$ at the contact line. The diffusion-limited evaporative flux (black line) varies more throughout the droplet, resembling the spherical cap solution given by equation (4.29) (though not singular due to the precursor film). It rapidly increases near the contact line before decaying to $J = 0$ in the precursor film.

The diffusion-limited evaporative flux shown in figure 4.4 (b) (black line) is similar to what has been reported in previous studies. However, the qualitative shape of the one-sided evaporative flux (red line) changes depending on the value of the parameter K in equation (4.19). When $K \gg h$, the evaporative flux is insensitive to the droplet profile and $J \approx K^{-1}$ is nearly constant throughout the droplet. However, if $K \sim h$ or $K \ll h$, J will increase as the droplet thins near

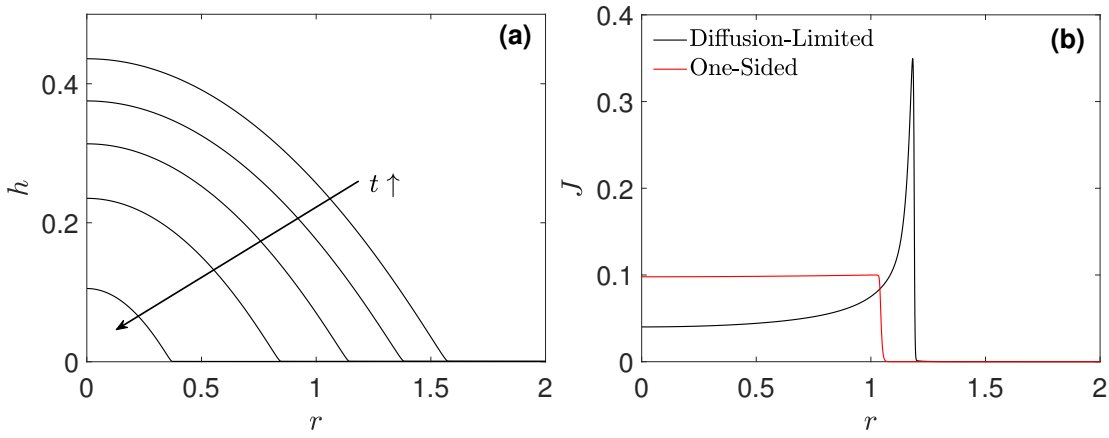

Figure 4.4: (a) Droplet shape sampled at intervals of $t_0/5$ under diffusion-limited evaporation, starting from $t = t_0/10$ where t_0 is the droplet lifetime. The arrow points in the direction of increasing time. The evolution is qualitatively similar under one-sided evaporation. (b) The evaporative flux J for both evaporation models at $t = t_0/2$. Note that the droplet radius is larger under diffusion-limited evaporation, despite the same t_0, due to different dependencies on the droplet radius (see equations (4.38) and (4.41)).

the contact line and the one-sided evaporative flux will qualitatively resemble the diffusion-limited evaporative flux (see refs. 65 and 92). In this work, we focus on the case where $K \gg h$ since this is the parameter regime investigated by Murisic and Kondic[82] and also allows an insightful analytical simplification that will be discussed in §A. Furthermore, the value of K does not affect the qualitative behavior of the temperature profiles we investigate in §VI.

Figure 4.5 shows the droplet radius R and apparent contact angle θ_a versus time for both evaporation models. Under diffusion-limited evaporation (black lines), the droplet radius (figure 4.5 (a)) is well approximated by equation (4.39) (dashed line) which shows the expected scaling $R \sim \sqrt{t_0 - t}$, and the apparent contact angle (figure 4.5 (b)) remains nearly constant throughout most of the droplet lifetime. This behavior of the radius and contact angle has been observed in previous experimental studies.[94,98] However, under one-sided evaporation (red

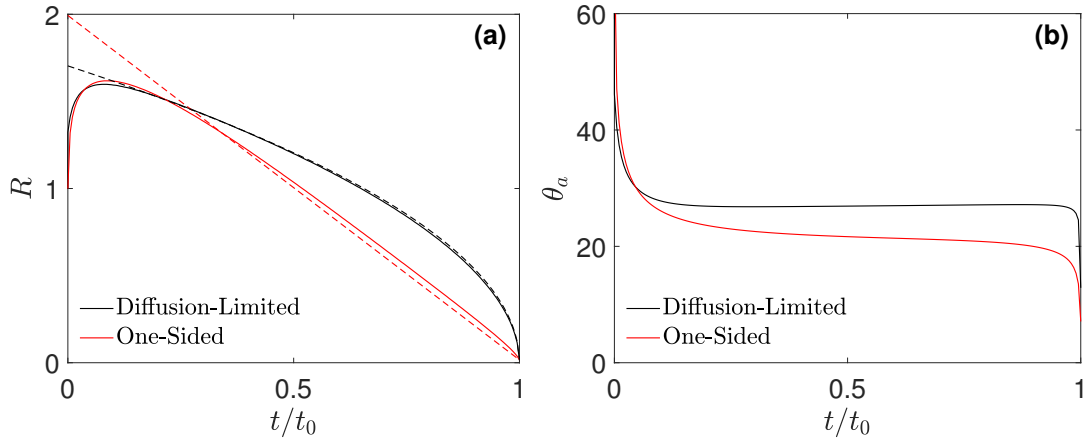

Figure 4.5: (a) Radius R and (b) apparent contact angle θ_a over time for both evaporation models. Analytical approximations given by equations (4.39) (black) and (4.47) (red) are plotted as dashed lines in panel (a). Note that they do not capture the initial spreading phase of the droplet. The apparent contact angle θ_a is computed from the maximum slope of the liquid-air interface.

lines), the radius shrinks almost linearly with time (figure 4.5 (a)) and the apparent contact angle noticeably decreases over time (figure 4.5 (b)) which is qualitatively distinct from the behavior under diffusion-limited evaporation. Note that in the analysis given below, we will disregard the initial spreading phase (giving the initial increase in R and decrease in θ_a) as well as the end of the droplet lifetime where the droplet is small enough so that the bulk is no longer distinct from the contact-line region (resulting in another decrease in θ_a).

A Comparison of Droplet Radius

We now compare the two evaporation models to understand the differences in the predictions of the droplet radius. Turning first to diffusion-limited evaporation, the droplet radius shown in figure 4.5 (a) (black lines) is well-approximated by equation (4.39) because the droplet shape is well-approximated by a spherical cap. Note that this results in equation (4.38) for the total evaporative flux $J_{tot} \sim R$

which scales with the droplet circumference. This result holds regardless of the parameters c_∞ and Z as long as the droplet shape is well-approximated by a spherical cap.

Now focusing on one-sided evaporation, we may rewrite J given by equation (4.19) in terms of Γ (neglecting the pressure contribution because it is unimportant in the bulk),

$$J = \frac{(K+\kappa)^{-1}}{1+\Gamma\left(1-\left(\frac{r}{R}\right)^2\right)}. \tag{4.45}$$

In the limit that $\Gamma = R\tan\theta_a/2(K+\kappa) \ll 1$, this reduces to the constant evaporative flux $J \approx (K+\kappa)^{-1}$. The total evaporative flux then becomes

$$J_{tot} = \int_0^R rJ\,\mathrm{d}r \approx \frac{R^2}{2(K+\kappa)}. \tag{4.46}$$

The condition $\Gamma \ll 1$ states that the droplet shape does not influence the evaporative flux, hence giving a nearly constant J throughout the bulk. In contrast to the simple analytical relations one obtains for diffusion-limited evaporation (equation (4.38)), equation (4.46) is only valid in parameter regimes where $\Gamma \ll 1$.

With $R \sim 1$, $\theta_a \approx 23°$, and $K+\kappa = 10$, we have $\Gamma \ll 1$ for results presented in this work – as evidenced by the nearly constant one-sided evaporative flux in figure 4.4 (b). Substituting equation (4.46) into equation (4.35) results in a linear scaling for the droplet radius under one-sided evaporation:

$$R(t) = \frac{4E}{3\tan\theta_a(K+\kappa)}(t_0^{(o)} - t). \tag{4.47}$$

Note that this assumes a constant apparent contact angle θ_a, and despite θ_a varying as shown in figure 4.5 (b), well-approximates the radius evolution shown in figure 4.5 (a) (red lines). Equation (4.47) can equivalently be obtained by simplifying equation (4.42) in the limit $\Gamma \ll 1$.

In experimental studies of drying droplets, it has been observed that J_{tot} is proportional to the surface area ($\sim R^2$) in some systems (such as forced convection over the droplet),[94] and diffusion-limited evaporation fails to capture the evolution because it predicts J_{tot} proportional to the circumference of the droplet ($J_{tot} \sim R$ as shown in equation (4.38)). In such a scenario, one-sided evaporation may be able to capture the droplet evolution since it predicts $J_{tot} \sim R^2$ when $\Gamma \ll 1$; by treating the value of K in relations (4.46) and (4.47) as a fitting parameter, one can adjust the evaporation rate to fit experimental data.

B Comparison of Droplet Contact Angle

We now discuss trends in the apparent contact angle θ_a and elucidate fundamental differences in the structure of the two evaporation models near the droplet contact line. Figure 4.5 (b) shows that, after the initial spreading phase, θ_a remains nearly constant under diffusion-limited evaporation (black line) but decreases steadily under one-sided evaporation (red line). To understand this difference, we must look more closely at the dynamics near the droplet contact line that give rise to θ_a. Figure 4.6 shows a scaled-up view of the droplet contact line, where capillary effects tend to spread the droplet while evaporation tends to contract it. Eggers and Pismen[17] showed that, under diffusion-limited evaporation, the size of the

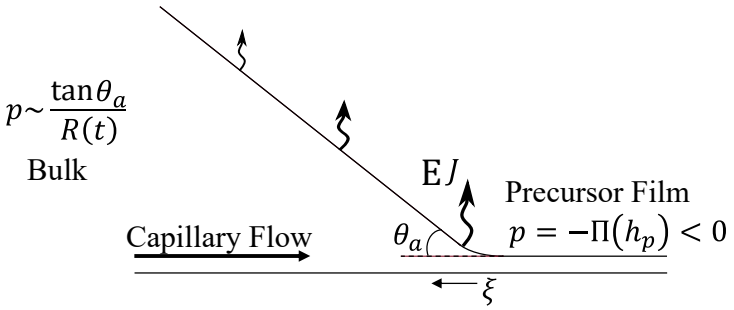

Figure 4.6: Schematic of droplet contact-line region. Evaporation competes with capillary flow to establish the apparent contact angle θ_a. The coordinate ξ is a scaled distance from the droplet contact line given by equation (4.48). The bulk pressure is given by equation (4.49).

contact-line region w scales as $w \sim R^{1/3}$, so ξ depicted in figure 4.6 is a scaled distance away from the contact line such that $\xi \sim 1$ in the contact-line region:

$$\xi \sim \frac{R - r}{R^{1/3}}. \tag{4.48}$$

The driving force for spreading arises from the difference in capillary pressure in the bulk and disjoining pressure in the precursor film. For a spherical-cap droplet, substituting equation (4.36) into equation (4.6) (and neglecting disjoining pressure in the bulk) gives

$$p \approx -\frac{1}{r}\frac{\partial}{\partial r}\left(r\frac{\partial h}{\partial r}\right) = \frac{2\tan\theta_a}{R(t)}. \tag{4.49}$$

While the pressure in the precursor film $p = -\Pi(h_p)$ remains constant and negative, the bulk pressure scales as $p \sim R^{-1}$ which grows as the droplet shrinks. Thus, the driving force for spreading becomes larger as the droplet evaporates which tends to decrease θ_a over time.

Opposing this capillary spreading is evaporation, where a nonuniform evaporative flux that is focused at the contact line will tend to increase θ_a. Under

diffusion-limited evaporation (assuming a spherical cap for simplicity), we have near the contact line

$$J \sim \frac{1}{\sqrt{R^2 - r^2}} \sim \frac{1}{\sqrt{R(R-r)}} \sim \frac{1}{R^{2/3}\sqrt{\xi}}. \tag{4.50}$$

First, we see that J grows like $\xi^{-1/2}$ as we move toward the contact line ($\xi \to 0$), obtaining its maximum (singular) value at $r = R$. Second, note that as the droplet shrinks and R decreases, J increases and becomes more nonuniform (the peak shown in figure 4.4 (b) becomes steeper). Thus, diffusion-limited evaporation tends to increase θ_a as the droplet shrinks, balancing the increasing capillary pressure and giving the nearly constant θ_a shown in figure 4.5 (b) (black line).

For one-sided evaporation, note that near the contact line $h \approx h_p$, and the pressure is dominated by the disjoining pressure, so we have from equation (4.19),

$$J = \frac{1 + \delta p}{K + h + \kappa} \approx \frac{1}{K + h_p + \kappa} \left(1 - \delta\Pi(h)\right). \tag{4.51}$$

Thus, as we move toward the contact line and precursor film where $1 - \delta\Pi(h) \to 0$ (see equation (4.20)), the evaporative flux J decreases (shown in figure 4.4 (b)). This behavior is opposite to that for diffusion-limited evaporation, resulting in the steady decrease in θ_a shown in figure 4.5 (b) (red line). This may explain the decreasing contact angle experimentally observed by Murisic and Kondic[82] for evaporating water droplets well-described by one-sided evaporation.

These effects are amplified as the evaporative number E is increased. Figure 4.7

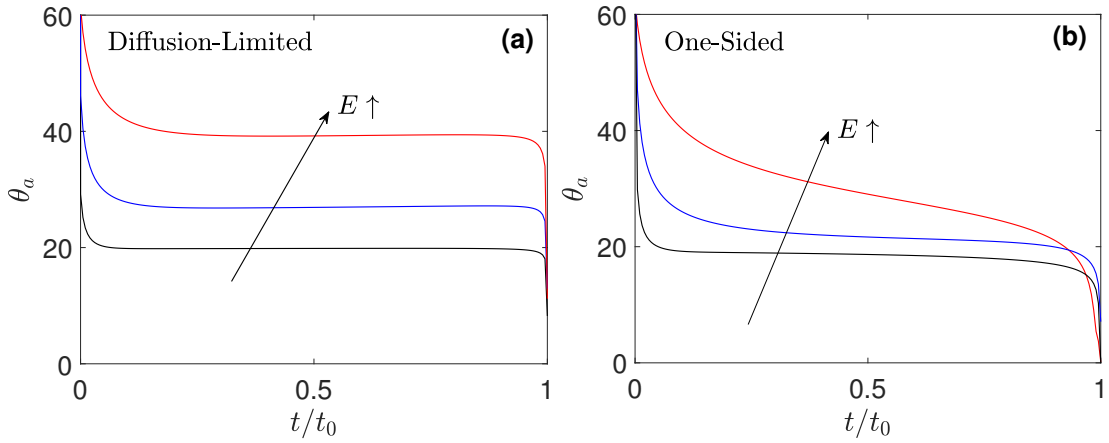

Figure 4.7: The apparent contact angle θ_a over time for (a) diffusion-limited and (b) one-sided evaporation as E is increased by an order of magnitude for each line. The black line is for $E = 10^{-3}$. Note that θ_a approaches the equilibrium contact angle $\theta_{eq} \approx 18°$ (see §D) as E is decreased because the droplet approaches its equilibrium shape.

shows the apparent contact angle θ_a over time for both one-sided and diffusion-limited evaporation as E is increased. With slow evaporation, the droplet will assume its equilibrium shape and the contact angle will remain nearly constant at θ_{eq} under both evaporation models (though the radius evolution remains qualitatively different as shown in figure 4.5 (a)). This is what we observe for $E = 10^{-3}$ in figure 4.7 (black lines). Now, as E is increased under diffusion-limited evaporation, θ_a increases but remains nearly constant throughout most of the droplet lifetime. As E is increased, the effect of evaporation increasing θ_a is intensified (see figure 4.6), leading to a larger θ_a. This in turn increases the bulk capillary pressure (equation (4.49)), maintaining the balance between capillary spreading and nonuniform evaporation. However, one-sided evaporation tends to decrease θ_a. So while increasing E results in a net increase in θ_a due to faster overall evaporation, there is a steeper decrease in θ_a over time due to increasing capillary pressure.

VI Comparison of Thermal Gradients

In this section, we discuss how the fundamental differences revealed in §V give rise to qualitative differences in the predicted temperature profiles under each evaporation model. Specifically, we will show that the contact line is always warmer than the bulk droplet under one-sided evaporation, whereas it can be warmer or cooler under diffusion-limited evaporation. For the results presented here, we set $Ma = 0.1$; we have found that the magnitude of Marangoni flow does not qualitatively change our findings.

Figure 4.8 shows temperature profiles T_I at the liquid-air interface under diffusion-limited (black line) and one-sided (red line) evaporation. The temperature profile at the interface is given by equation (4.16), so the temperature will change throughout the droplet as J and h vary, and then rapidly increase to $T_I = 1$ in the precursor film where $J = 0$. For an infinitely conductive substrate, we have $\kappa = 0$ and figure 4.8 (a) shows that both evaporation models predict qualitatively similar temperature profiles; the droplet is cooler in the center and warms as it thins toward the contact line where more heat is transported from the substrate to the liquid-air interface. However, at a larger conductivity ratio $\kappa = 2/3$ (less conductive or thicker substrate), figure 4.8 (b) shows that the evaporation models predict opposite trends in the temperature profile. While one-sided evaporation still predicts a warmer contact line, diffusion-limited evaporation now predicts a colder contact line. This trend for diffusion-limited evaporation is consistent with findings by Ristenpart et al.,[83] where the sign of thermal gradients near the

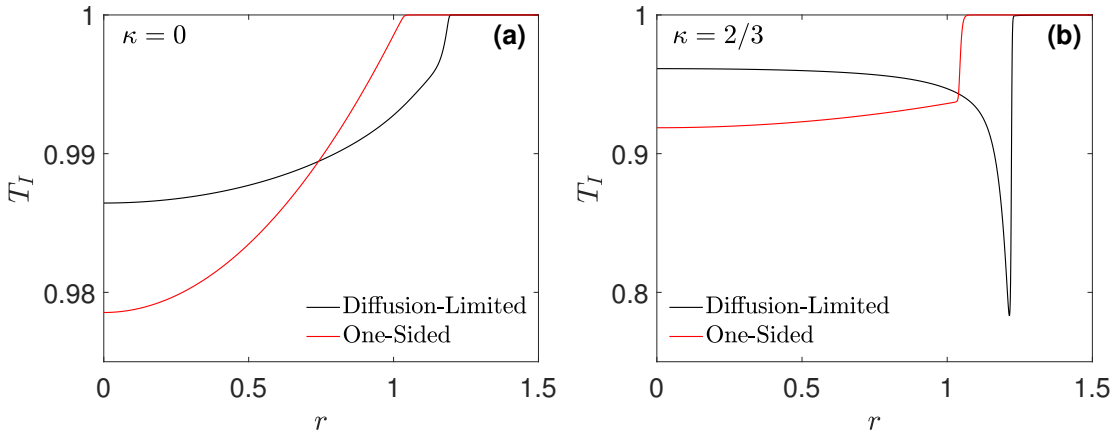

Figure 4.8: Interface temperature T_I profiles at $t = t_0/2$ for (a) $\kappa = 0$ and (b) $\kappa = 2/3$. Note that the temperature reaches its maximum $T_I = 1$ in the precursor film where $J = 0$ and there is no evaporative cooling. The droplet radius at $t = t_0/2$ is larger under diffusion-limited evaporation, despite the same t_0, due to different dependencies on the droplet radius (see equations (4.38) and (4.41)).

contact line reverses as κ is increased above a critical value κ_c.

Figure 4.8 (b) shows that thermal gradients under one-sided evaporation do not reverse at the same κ_c as diffusion-limited evaporation; we will show that one-sided evaporation always predicts a warmer contact line. For a general evaporative flux J, thermal gradients at the interface are given by

$$\frac{\partial T_I}{\partial r} = -\underbrace{(h+\kappa)\frac{\partial J}{\partial r}}_{\text{(a)}} - \underbrace{J\frac{\partial h}{\partial r}}_{\text{(b)}}, \tag{4.52}$$

which has contributions from (a) gradients in evaporative cooling/heating and (b) gradients in the droplet thickness – a thinner droplet will conduct more heat from the substrate to the liquid-air interface. Note that, for most droplets, $\partial h/\partial r < 0$, so term (b) contributes to positive thermal gradients (a warmer contact line). To have a negative thermal gradient, the evaporative flux J must offset this and

satisfy the inequality

$$\frac{1}{J}\frac{\partial J}{\partial r} > -\frac{1}{h+\kappa}\frac{\partial h}{\partial r}. \tag{4.53}$$

That is, the evaporative flux must increase sufficiently fast to offset heating from the substrate.

Recall from equation (4.51) that the one-sided evaporative flux decreases as one approaches the contact line (see figure 4.4 (b)), so $\partial J/\partial r < 0$ and inequality (4.53) can never be satisfied. Thus, one-sided evaporation always results in a warmer contact line. Substituting equation (4.19) into equation (4.52) gives

$$\frac{\partial T_I}{\partial r} = -\frac{1}{K+h+\kappa}\left(\delta\left(h+\kappa\right)\frac{\partial p}{\partial r} + KJ\frac{\partial h}{\partial r}\right). \tag{4.54}$$

Noting that both $\partial p/\partial r < 0$ and $\partial h/\partial r < 0$ near the contact line, $\partial T_I/\partial r$ is strictly positive near the contact line under one-sided evaporation for all values of K, δ, and κ. While increasing κ decreases the influence of substrate heating in inequality (4.53), it also decreases the evaporative flux given by equation (4.19). This is not the case with diffusion-limited evaporation, where the evaporative flux does not explicitly depend on κ. As shown in figure 4.4 (b), the diffusion-limited evaporative flux (black line) increases rapidly near the contact line, so $\partial J/\partial r > 0$. For a sufficiently large $\kappa > \kappa_c$, this increase in J is larger than the substrate-heating effect on the right-hand side of equation (4.53) and we observe a cooler contact line as shown in figure 4.8 (b).

While it does not qualitatively affect our results, we briefly discuss the influence

of Marangoni flow on droplet evolution. When the contact line is warmer than the bulk, as in figure 4.8 (a), Marangoni flow is directed away from the contact line toward the bulk. This causes the droplet to retract and have a smaller radius R and larger apparent contact angle θ_a. Consequently, evaporation is slower in both one-sided and diffusion-limited evaporation (see equations (4.38) and (4.46)). When the contact line is colder than the bulk droplet, as for diffusion-limited evaporation (black line in figure 4.8 (b)), Marangoni flow is directed outward toward the contact line. This causes the droplet to spread, giving larger R and smaller θ_a and consequently faster evaporation. This effect of Marangoni flow is consistent with what has been previously observed theoretically and experimentally for evaporating sessile droplets.[66,82,99]

VII Conclusions

In this work, we have compared predictions from one-sided and diffusion-limited evaporation to develop a fundamental understanding of each model and their differences. First, while it is known that the diffusion-limited evaporation rate is proportional to the droplet circumference ($\sim R$), we show that for a sufficiently large inverse mass-transfer coefficient, the one-sided evaporation rate is proportional to the droplet surface area ($\sim R^2$). Previous work has reported that in some scenarios, experimentally measured evaporation rates are proportional to the droplet surface area and diffusion-limited evaporation is inaccurate.[94] One-sided evaporation may be able to capture experimental data in these scenarios by

treating the inverse mass-transfer coefficient as a fitting parameter.

Second, we showed that fundamental differences in the structure of the evaporation models near the contact line leads to fundamentally different behavior of apparent contact angles. Under diffusion-limited evaporation, the apparent contact angle remains nearly constant throughout most of the droplet lifetime; the diffusion-limited evaporative flux grows increasingly quickly near the contact line as the droplet shrinks, counteracting increasing capillary pressures to give a nearly constant apparent contact angle. In contrast, under one-sided evaporation the apparent contact angle decreases appreciably as the droplet shrinks; the one-sided evaporative flux decreases near the contact line and cannot oppose increasing capillary pressures. This can explain the decrease in θ_a experimentally observed by Murisic and Kondic[82] for evaporating water droplets well-described by one-sided evaporation.

The form of the one-sided evaporative flux near the contact line leads to it always predicting a warmer contact line; because the evaporative flux decreases near the contact line, evaporative cooling cannot compete with heating from the substrate as the droplet thins. In contrast, the contact line under diffusion-limited evaporation can either be warmer or colder than the bulk depending on the conductivity ratio of the liquid and solid.

To conclude, we speculate on the differences in deposition patterns under one-sided and diffusion-limited evaporation. The formation of a coffee-ring-like deposition pattern is linked to pinning of the contact line that leads to particle

accumulation.[11,65,74] The diffusion-limited evaporative flux shown in figure 4.4 (b) (black line) increases sharply near the contact line, which is expected to cause particle accumulation there. This accumulation would increase the viscosity and possibly cause self-pinning,[112] leading to a coffee-ring-like deposition pattern. In contrast, the one-sided evaporative flux shown in figure 4.4 (b) (red line) is not as peaked at the contact line, so one might expect a coffee-ring-like deposition pattern to form more slowly and to be less pronounced. However, as discussed in §V, under some conditions the one-sided evaporative flux resembles the diffusion-limited evaporative flux, in which case we would expect the deposition patterns to be more similar.

Chapter 5

Future Directions

The work presented in this thesis has developed fundamental understanding of several important coating flows that can aid in the design of coating processes. However, there are many extensions of this work that could also produce insightful understanding; this chapter identifies and motivates some promising future directions that build on the work presented chapters 2-4.

I Multilayer Coatings: Surfactants and Evaporation

Chapter 2 developed fundamental understanding of the evolution of multilayer coatings. To this end, the model was idealized to a binary, nonvolatile liquid. It was found the multilayer geometry causes convective steeping and destabilizes the liquid coating, leading to larger nonuniformities. In §A, it is hypothesized that the addition of surfactant may stabilize the coating by inhibiting the convective

steepening mechanism. In addition, liquid coatings are often dried, so §B discusses how evaporation may couple with the findings presented in chapters 2 and 3.

A Surfactants

In chapter 2, it was shown that Marangoni flow due to solutal concentration gradients couples with the multilayer geometry to generate large height nonuniformities (convective steepening). This is often undesirable, so one may wish to lessen the magnitude of Marangoni flow beyond what is possible by simply changing the parameters discussed in chapter 2. A promising method is the addition of surfactants because they lower the surface tension and are convected with the flow. Under the influence of Marangoni flow, the surfactant will accumulate in regions of high surface tension, lowering the surface tension and driving flow backwards to level the coating. Thus, it is hypothesized that surfactants will help to stabilize the multilayer geometries studied in chapter 2.

A study that incorporates surfactant into the model derived in chapter 2 could offer value insight into methods to stabilize multilayer coatings. This would require introducing bulk and interfacial conservation equations for the surfactant species, as well as incorporating the dependence of the surface tension on the surfactant concentration (see Refs. 13 and 61 for examples). The convective steepening mechanism highlighted in chapter 2 will likely introduce complicated couplings between bulk and interfacial surfactant concentrations that may lead to unexpected effects on the evolution of the multilayer coatings.

B Evaporation

In addition to surfactants, evaporation offers another promising avenue for expanding the work presented in chapter 2. Liquid coatings are often dried to obtain the final solidified coating, so evaporation can have significant effects on the evolution of liquid coatings in coating processes. Nonuniform evaporation inherently creates gradients in the liquid temperature, inducing Marangoni flow. Furthermore, it was shown in 3 that the species concentration gradients that develop from evaporation can be important in the evolution of the coating. Both of these phenomena will couple with the convective steepening mechanism discussed in 2.

By incorporating evaporation and a solidification mechanism, such as colloidal particles or a nonvolatile polymer, into the model used in chapter 2, one can develop important fundamental understanding of how evaporation couples with multilayer geometries. The Marangoni flow and species concentration gradients induced by evaporation may couple with the convective steepening mechanism to lead to unique and interesting phenomena. Furthermore, as the film solidifies the viscosity will increase which may lessen the effect of convective steepening. The understanding gained from this model would be of great use in many multilayer coating applications.

II Particle-Laden Droplets

Coating processes such as inkjet printing and spray coating deposit droplets of liquid onto a solid substrate. This liquid is often particle-laden so that the droplets

leave behind a deposition of particles once fully dried. The shape and density (or pattern) of this deposition is crucial to applications that employ droplets – inkjet printing, for example, must have precise control over where the pigment deposits. Control over deposition patterns requires a deep, fundamental knowledge of how particle-laden droplets dry and the resulting effects on particle deposition patterns.

As a droplet dries, the contact line will recede. This sweeps particles towards the center of the droplet and can result in a myriad of deposit shapes.[65] However, a phenomenon known as pinning (where the contact line pins and ceases to move) causes outward flow and particles accumulate in a ring at the contact line. This causes the "coffee-ring" effect, where particles accumulate heavily in a ring and more lightly in the center. This is often undesirable (e.g., in printing), so a great wealth of literature has been dedicated to understanding the drying of pinned and particle-laden droplets.

A Comparison of Evaporation Models

Akin to the motivation for chapter 4, there are two predominant models for evaporation that can give qualitatively different predictions of the evolution of liquid droplets. However, the question of how these two evaporation models, one-sided and diffusion-limited, affect pinning and particle deposition patterns remains open; chapter 4 briefly speculates on the phenomenon known as self-pinning, but does not draw any conclusions about the evolution of pinned droplets and the resulting deposition patterns under each model. A study that extends the work in chapter 4 to pinned and particle-laden droplets can develop the fundamental understanding

necessary to answer this question.

The inclusion of colloidal particles requires a conservation equation for the particle mass. Since these particles are typically rigid and small compared to the domain size, this takes the form a standard convection-diffusion equation for the particle volume fraction (see Refs. 65 and 66). Without enforcing the droplet contact line be stationary *a priori*, pinning can be incorporated by introducing small bumps on the solid substrate that represent defects. As the contact line moves over this defect, a pressure gradient develops that arrests the contact line if the defect is sufficiently large. This approach has been shown to qualitatively agree with experimental studies of drying, pinned droplets.[65]

B Multiscale Modeling of Particle Packing

Another complication that arises when modeling drying particle-laden liquids is how to model the system when the particles become packed. According to the Krieger-Dougherty relation, the viscosity μ of a particle-laden liquid is given by

$$\mu = \mu_0 \left(1 - \frac{\phi}{\phi_p}\right)^{-2}, \tag{5.1}$$

where μ_0 is the viscosity of the pure liquid, ϕ is the volume fraction of particles, and ϕ_p is the maximum packing fraction. As ϕ approaches ϕ_p, the viscosity diverges because the system undergoes a transition from continuous liquid to porous media; the particles pack and the liquid fills the interstitial space between them. This could be strongly linked to self-pinning, since this packed region of particles may

act as a solid defect for the contact line to pin to. The liquid menisci inside the packing also lead to stresses in dried particulate coatings that cause cracking and delamination (common problems in coating processes).[113]

A model that incorporates the continuous liquid-phase modeling presented in this thesis with a model for the packed-particle region would be poised to make great advances in the field of multiscale modeling. This model could develop understanding of the dynamics of self-pinning as well as generate physical insight into the cracking and delamination of dried particulate coatings.[113]

Bibliography

[1] C. K. Buerkin, I. de Vries, S. M. Raupp, P. Scharfer, W. Schabel, and P. Groen, Investigation of interfacial instabilities with a two-layer slide coating process, Journal of Coatings Technology and Research **14**, 991 (2017).

[2] P. Kolliopoulos, K. S. Jochem, R. K. Lade, L. F. Francis, and S. Kumar, Capillary flow with evaporation in open rectangular microchannels, Langmuir **35**, 8131 (2019).

[3] S. Karki, H. Kim, S. J. Na, D. Shin, K. Jo, and J. Lee, Thin films as an emerging platform for drug delivery, Asian Journal of Pharmaceutical Sciences **11**, 559 (2016).

[4] M. Dey, A. S. Vivek, H. N. Dixit, A. Richhariya, and J. J. Feng, A model of tear-film breakup with continuous mucin concentration and viscosity profiles, Journal of Fluid Mechanics **858**, 352 (2019).

[5] R. J. Braun, T. A. Driscoll, C. G. Begley, P. E. King-Smith, and J. I. Siddique, On tear film breakup (tbu): dynamics and imaging, Mathematical Medicine and Biology: A Journal of the IMA **35**, 145 (2018).

[6] M. Schmitt, S. Raupp, D. Wagner, P. Scharfer, and W. Schabel, Analytical determination of process windows for bilayer slot die coating, Journal of Coatings Technology and Research **12**, 877 (2015).

[7] D. Lohse, Fundamental Fluid Dynamics Challenges in Inkjet Printing, Annual Review of Fluid Mechanics **54**, 349 (2022).

[8] D. Lohse and X. Zhang, Physicochemical hydrodynamics of droplets out of equilibrium, Nature Reviews Physics **2**, 426 (2020).

[9] K. B. Sutton, C. B. Clemons, K. L. Kreider, J. P. Wilber, and G. W. Young, Surface Nonuniformities in Latex Paints Due to Evaporative Mechanisms, AIChE Journal **64**, 1841 (2018).

[10] A. Oron, S. H. Davis, and S. G. Bankoff, Long-scale evolution of thin liquid films, Reviews of Modern Physics **69**, 931 (1997).

[11] S. K. Wilson and H.-M. D'Ambrosio, Evaporation of Sessile Droplets, Annual Review of Fluid Mechanics **55**, 481 (2022).

[12] R. Horiuchi, W. J. Suszynski, and M. S. Carvalho, Simultaneous multilayer coating of water-based and alcohol-based solutions, Journal of Coatings Technology and Research **12**, 819 (2015).

[13] O. E. Jensen and J. B. Grotberg, The spreading of heat or soluble surfactant along a thin liquid film, Physics of Fluids A: Fluid Dynamics **5**, 58 (1993).

[14] T. Pham, X. Cheng, and S. Kumar, Drying of multicomponent thin films on substrates with topography, Journal of Polymer Science Part B: Polymer Physics **55**, 1681 (2017).

[15] T. Pham and S. Kumar, Imbibition and evaporation of droplets of colloidal suspensions on permeable substrates, Physical Review Fluids **4**, 034004 (2019).

[16] M. H. Eres, D. E. Weidner, and L. W. Schwartz, Three-Dimensional Direct Numerical Simulation of Surface-Tension-Gradient Effects on the Leveling of an Evaporating Multicomponent Fluid, Langmuir **15**, 1859 (1999).

[17] J. Eggers and L. M. Pismen, Nonlocal description of evaporating drops, Physics of Fluids **22**, 112101 (2010).

[18] R. G. Larson, Transport and deposition patterns in drying sessile droplets, AIChE Journal **60**, 1538 (2014).

[19] S. D. Howison, J. A. Moriarty, J. R. Ockendon, E. L. Terrill, and S. K. Wilson, A mathematical model for drying paint layers, Journal of Engineering Mathematics **32**, 377 (1997).

[20] C. Parrish and S. Kumar, Simultaneous liquid flow and drying on rotating cylinders, Physical Review Fluids **5**, 034001 (2020).

[21] L. Espín and S. Kumar, Sagging of Evaporating Droplets of Colloidal Suspensions on Inclined Substrates, Langmuir **30**, 11966 (2014).

[22] M. R. Moore, D. Vella, and J. M. Oliver, The nascent coffee ring: how solute diffusion counters advection, Journal of Fluid Mechanics **920**, A54 (2021).

[23] S. Shenvi Usgaonkar, C. J. Ellison, and S. Kumar, Controlling surface deformation and feature aspect ratio in photochemically induced marangoni patterning of polymer films, Langmuir **28**, 475 (2000).

[24] C. Larsson and S. Kumar, Nonuniformities in miscible two-layer two-component thin liquid films, Physical Review Fluids **6**, 034004 (2021).

[25] C. Girotto, B. P. Rand, J. Genoe, and P. Heremans, Exploring spray coating as a deposition technique for the fabrication of solution-processed solar cells, Solar Energy Materials and Solar Cells **93**, 454 (2009).

[26] R. V. Craster and O. K. Matar, Dynamics and stability of thin liquid films, Reviews of Modern Physics **81**, 1131 (2009).

[27] S. K. Serpetsi and S. G. Yiantsios, Stability characteristics of solutocapillary marangoni motion in evaporating thin films, Physics of Fluids **24**, 122104 (2012).

[28] J. R. A. Pearson, On convection cells induced by surface tension, Journal of Fluid Mechanics **4**, 489 (1958).

[29] L. E. Scriven and C. V. Sternling, On cellular convection driven by surface-tension gradients: effects of mean surface tension and surface viscosity, Journal of Fluid Mechanics **19**, 321 (1964).

[30] C. V. Sternling and L. E. Scriven, Interfacial turbulence: Hydrodynamic instability and the marangoni effect, AIChE Journal **5**, 514 (1959).

[31] S. G. Yiantsios, S. K. Serpetsi, F. Doumenc, and B. Guerrier, Surface deformation and film corrugation during drying of polymer solutions induced by marangoni phenomena, International Journal of Heat and Mass Transfer **89**, 1083 (2015).

[32] M. Rodríguez-Hakim, J. M. Barakat, X. Shi, E. S. G. Shaqfeh, and G. G. Fuller, Evaporation-driven solutocapillary flow of thin liquid films over curved substrates, Physical Review Fluids **4**, 034002 (2019).

[33] J. P. Burelbach, S. G. Bankoff, and S. H. Davis, Nonlinear stability of evaporating/condensing liquid films, Journal of Fluid Mechanics **195**, 463 (1988).

[34] S. G. Yiantsios and B. G. Higgins, Marangoni flows during drying of colloidal films, Physics of Fluids **18**, 082103 (2006).

[35] A. F. Routh and W. B. Zimmerman, Distribution of particles during solvent evaporation from films, Chemical Engineering Science **59**, 2961 (2004).

[36] L. Merklein, M. Mink, D. Kourkoulos, B. Ulber, S. M. Raupp, K. Meerholz, P. Scharfer, and W. Schabel, Multilayer oleds with four slot die-coated layers, Journal of Coatings Technology and Research **16**, 1643 (2019).

[37] V. Derflinger, Multilayer hard coating for tools, U.S. Patent No. 7618720 (2009).

[38] J. C. Grunlan, Multilayer coating for flame retardant substrates, U.S. Patent No. 9540763 (2012).

[39] R. Belden, Multilayer coating with visual effect, International Patent Application No. 2017/066604 (2017).

[40] K. D. Danov, V. N. Paunov, N. Alleborn, H. Raszillier, and F. Durst, Stability of evaporating two-layered liquid film in the presence of surfactant - i. the equations of lubrication approximation, Chemical Engineering Science **53**, 2809 (1998).

[41] K. D. Danov, V. N. Paunov, S. D. Stoyanov, N. Alleborn, H. Raszillier, and F. Durst, Stability of evaporating two-layered liquid film in the presence

of surfactant - ii. linear analysis, Chemical Engineering Science **53**, 2823 (1998).

[42] V. N. Paunov, K. D. Danov, N. Alleborn, H. Raszillier, and F. Durst, Stability of evaporating two-layered liquid film in the presence of surfactant - iii. non-linear stability analysis, Chemical Engineering Science **53**, 2839 (1998).

[43] J. Nam and M. S. Carvalho, Linear stability analysis of two-layer rectilinear flow in slot coating, AIChE Journal **56**, 2503 (2010).

[44] A. Kalogirou, Instability of two-layer film flows due to the interacting effects of surfactants, inertia, and gravity, Physics of Fluids **30**, 030707 (2018).

[45] S. Ghosh, R. Usha, and K. C. Sahu, Linear stability analysis of miscible two-fluid flow in a channel with velocity slip at the walls, Physics of Fluids **26**, 014107 (1994).

[46] B. Tsai, M. S. Carvalho, and S. Kumar, Leveling of thin films of colloidal suspensions, Journal of Colloid and Interface Science **343**, 306 (2010).

[47] R. V. Craster and O. K. Matar, Numerical simulations of fingering instabilities in surfactant-driven thin films, Physics of Fluids **18**, 032103 (2006).

[48] B. D. Edmonstone, O. K. Matar, and R. V. Craster, A note on the coating of an inclined plane in the presence of soluble surfactant, Journal of Colloid and Interface Science **293**, 222 (2006).

[49] G. Vazquez, E. Alvarez, and J. M. Navaza, Surface tension of alcohol + water from 20 to 50 c, Journal of Chemical and Engineering Data **40**, 611 (1995).

[50] J. P. Boyd, *Chebyshev and Fourier Spectral Methods: Second Revised Edition* (2001).

[51] L. N. Trefethen, *Spectral Methods in MATLAB* (2000).

[52] D. Kosloff and H. Tal-Ezer, A modified chebyshev pseudospectral method with an o(n-1) time step restriction, Journal of Computational Physics **104**, 457 (1993).

[53] J. L. Mead and R. A. Renaut, Optimal runge-kutta methods for first order pseudospectral operators, Journal of Computational Physics **152**, 404 (1999).

[54] M. Mistry and R. Misener, Optimising heat exchanger network synthesis using convexity properties of the logarithmic mean temperature difference, Computers and Chemical Engineering **94**, 1 (2016).

[55] M. Schulz and J. L. Keddie, A critical and quantitative review of the stratification of particles during the drying of colloidal films, Soft Matter **14**, 6181 (2018).

[56] J. Nam and M. S. Carvalho, Mid-gap invasion in two-layer slot coating, Journal of Fluid Mechanics **631**, 397 (2009).

[57] M. Dizechi and E. Marschall, Viscosity of some binary and ternary liquid mixtures, Journal of Chemical and Engineering Data **27**, 358 (1982).

[58] C. Larsson and S. Kumar, Quantitative analysis of the vertical-averaging approximation for evaporating thin liquid films, Physical Review Fluids **7**, 094002 (2022).

[59] M. Dey, F. Doumenc, and B. Guerrier, Numerical simulation of dip-coating in the evaporative regime, The European Physical Journal E **39**, 19 (2016).

[60] H. J. Palmer, The hydrodynamic stability of rapidly evaporating liquids at reduced pressure, Journal of Fluid Mechanics **75**, 487 (1976).

[61] S. G. Yiantsios and B. G. Higgins, A mechanism of marangoni instability in evaporating thin liquid films due to soluble surfactant, Physics of Fluids **22**, 022102 (2010).

[62] C. M. Cardinal, Y. D. Jung, K. H. Ahn, and L. F. Francis, Drying regime maps for particulate coatings, AIChE Journal **56**, 2769 (2010).

[63] C. Sodtke, V. S. Ajaev, and P. Stephan, Dynamics of volatile liquid droplets on heated surfaces: theory versus experiment, Journal of Fluid Mechanics **610**, 343 (2008).

[64] V. S. Ajaev, Spreading of thin volatile liquid droplets on uniformly heated surfaces, Journal of Fluid Mechanics **528**, 279 (2005).

[65] T. Pham and S. Kumar, Drying of Droplets of Colloidal Suspensions on Rough Substrates, Langmuir **33**, 10061 (2017).

[66] K. L. Maki and S. Kumar, Fast evaporation of spreading droplets of colloidal suspensions, Langmuir **27**, 11347 (2011).

[67] G. Karapetsas, K. C. Sahu, and O. K. Matar, Evaporation of Sessile Droplets Laden with Particles and Insoluble Surfactants, Langmuir **32**, 6871 (2016).

[68] D. P. Sheetz, Formation of Films by Drying of Latex, Journal of Applied Polymer Science **9**, 3759 (1965).

[69] A. F. Routh, Drying of thin colloidal films, Reports on Progress in Physics **76**, 046603 (2013).

[70] C. Loussert, F. Doumenc, J. B. Salmon, V. S. Nikolayev, and B. Guerrier, Role of Vapor Mass Transfer in Flow Coating of Colloidal Dispersions in the Evaporative Regime, Langmuir **33**, 14078 (2017).

[71] E. Sultan, A. Boudaoud, and M. B. Amar, Evaporation of a thin film: Diffusion of the vapour and Marangoni instabilities, Journal of Fluid Mechanics **543**, 183 (2005).

[72] B. Sobac, P. Colinet, and L. Pauchard, Influence of Bénard-Marangoni instability on the morphology of drying colloidal films, Soft Matter **15**, 2381 (2019).

[73] R. D. Deegan, O. Bakajin, T. F. Dupont, G. Huber, S. R. Nagel, and T. A. Witten, Capillary flow as the cause of ring stains from dried liquid drops, Nature **389**, 827 (1997).

[74] R. D. Deegan, O. Bakajin, T. F. Dupont, G. Huber, S. R. Nagel, and T. A. Witten, Contact line deposits in an evaporating drop, Physical Review E **62**, 756 (2000).

[75] H. Hu and R. G. Larson, Evaporation of a sessile droplet on a substrate, Journal of Physical Chemistry B **106**, 1334 (2002).

[76] C. Diddens, J. G. M. Kuerten, C. W. M. van der Geld, and H. M. A. Wijshoff, Modeling the evaporation of sessile multi-component droplets, Journal of Colloid and Interface Science **487**, 426 (2017).

[77] P. J. Sáenz, A. W. Wray, Z. Che, O. K. Matar, P. Valluri, J. Kim, and K. Sefiane, Dynamics and universal scaling law in geometrically-controlled sessile drop evaporation, Nature Communications **8**, 14783 (2017).

[78] B. Sobac, P. Talbot, B. Haut, A. Rednikov, and P. Colinet, A comprehensive analysis of the evaporation of a liquid spherical drop, Journal of Colloid and Interface Science **438**, 306 (2015).

[79] P. Talbot, B. Sobac, A. Rednikov, P. Colinet, and B. Haut, Thermal transients during the evaporation of a spherical liquid drop, International Journal of Heat and Mass Transfer **97**, 803 (2016).

[80] B. Sobac, Z. Larbi, P. Colinet, and B. Haut, Mathematical modeling of the drying of a spherical colloidal drop, Colloids and Surfaces A: Physicochemical and Engineering Aspects **576**, 110 (2019).

[81] C. Poulard, O. Bénichou, and A. M. Cazabat, Freely Receding Evaporating Droplets, Langmuir **19**, 8828 (2003).

[82] N. Murisic and L. Kondic, On evaporation of sessile drops with moving contact lines, Journal of Fluid Mechanics **679**, 219 (2011).

[83] W. D. Ristenpart, P. G. Kim, C. Domingues, J. Wan, and H. A. Stone, Influence of Substrate Conductivity on Circulation Reversal in Evaporating Drops, Physical Review Letters **99**, 234502 (2007).

[84] H. Hu and R. G. Larson, Marangoni effect reverses coffee-ring depositions, Journal of Physical Chemistry B **110**, 7090 (2006).

[85] M. Bestehorn and I. D. Borcia, Thin film lubrication dynamics of a binary mixture: Example of an oscillatory instability, Physics of Fluids **22**, 104102 (2010).

[86] S. Kumar and V. Charitatos, Influence of Surface Roughness on Droplet Evaporation and Absorption: Insights into Experiments from Lubrication-Theory-Based Models, Langmuir **38**, 15889 (2022).

[87] M. N. Popescu, G. Oshanin, S. Dietrich, and A.-M. Cazabat, Precursor films in wetting phenomena, Journal of Physics: Condensed Matter **24**, 243102 (2012).

[88] N. Savva and S. Kalliadasis, Dynamics of moving contact lines: A comparison between slip and precursor film models, EPL **94**, 64004 (2011).

[89] R. W. Schrage, *A theoretical study of interphase mass transfer.*, Ph.D. thesis, Columbia University Press, New York (1953).

[90] A.-M. Cazabat and G. Guéna, Evaporation of macroscopic sessile droplets, Soft Matter **6**, 2591 (2010).

[91] V. Charitatos and S. Kumar, A thin-film model for droplet spreading on soft solid substrates, Soft Matter **16**, 8284 (2020).

[92] V. S. Ajaev, Spreading of thin volatile liquid droplets on uniformly heated surfaces, Journal of Fluid Mechanics **528**, 279 (2005).

[93] J. M. Stauber, S. K. Wilson, B. R. Duffy, and K. Sefiane, On the lifetimes of evaporating droplets, Journal of Fluid Mechanics **744**, R2 (2014).

[94] N. Shahidzadeh-Bonn, S. Rafaï, A. Azouni, and D. Bonn, Evaporating droplets, Journal of Fluid Mechanics **549**, 307 (2006).

[95] S. J. Morris, Contact angles for evaporating liquids predicted and compared with existing experiments, Journal of Fluid Mechanics **432**, 1 (2001).

[96] E. Jambon-Puillet, O. Carrier, N. Shahidzadeh, D. Brutin, J. Eggers, and D. Bonn, Spreading dynamics and contact angle of completely wetting volatile drops, Journal of Fluid Mechanics **844**, 817 (2018).

[97] H. Hu and R. G. Larson, Marangoni effect reverses coffee-ring depositions, Journal of Physical Chemistry B **110**, 7090 (2006).

[98] K. Sefiane, S. David, and M. E. R. Shanahan, Wetting and Evaporation of Binary Mixture Drops, The Journal of Physical Chemistry B **112**, 11317 (2008).

[99] Y. Tsoumpas, S. Dehaeck, A. Rednikov, and P. Colinet, Effect of Marangoni Flows on the Shape of Thin Sessile Droplets Evaporating into Air, Langmuir **31**, 13334 (2015).

[100] S. Karpitschka, F. Liebig, and H. Riegler, Marangoni Contraction of Evaporating Sessile Droplets of Binary Mixtures, Langmuir **33**, 4682 (2017).

[101] A. A. Pahlavan, L. Yang, C. D. Bain, and H. A. Stone, Evaporation of Binary-Mixture Liquid Droplets: The Formation of Picoliter Pancakelike Shapes, Physical Review Letters **127**, 24501 (2021).

[102] L. Thayyil Raju, C. Diddens, Y. Li, A. Marin, M. N. van der Linden, X. Zhang, and D. Lohse, Evaporation of a Sessile Colloidal Water–Glycerol Droplet: Marangoni Ring Formation, Langmuir **38**, 12082 (2022).

[103] C. Diddens, H. Tan, P. Lv, M. Versluis, J. G. M. Kuerten, X. Zhang, and D. Lohse, Evaporating pure, binary and ternary droplets: thermal effects and axial symmetry breaking, Journal of Fluid Mechanics **823**, 470 (2017).

[104] H. Gelderblom, C. Diddens, and A. Marin, Evaporation-driven liquid flow in sessile droplets, Soft Matter **18**, 8535 (2022).

[105] L. W. Schwartz, Hysteretic effects in droplet motions on heterogeneous substrates: Direct numerical simulation, Langmuir **14**, 3440 (1998).

[106] L. Espín and S. Kumar, Droplet wetting transitions on inclined substrates in the presence of external shear and substrate permeability, Physical Review Fluids **2**, 014004 (2017).

[107] V. Charitatos, T. Pham, and S. Kumar, Droplet evaporation on inclined substrates, Physical Review Fluids **6**, 084001 (2021).

[108] J. A. Diez and L. Kondic, Computing Three-Dimensional Thin Film Flows Including Contact Lines, Journal of Computational Physics **183**, 274 (2002).

[109] C. Diddens, Detailed finite element method modeling of evaporating multi-component droplets, Journal of Computational Physics **340**, 670 (2017).

[110] M. Abramowitz and I. A. Stegun, *Handbook of Mathematical Functions with Formulas, Graphs, and Mathematical Tables*, ninth dover printing, tenth gpo printing ed. (Dover, New York, 1964).

[111] R. M. Corless, G. H. Gonnet, D. E. Hare, D. J. Jeffrey, and D. E. Knuth, On the Lambert W function, Advances in Computational Mathematics **5**, 329 (1996).

[112] R. D. Deegan, Pattern formation in drying drops, Physical Review E **61**, 475 (2000).

[113] K. K. Price, Y. Wu, A. V. McCormick, and L. F. Francis, Stress Development in Hard Particle Coatings in the Absence of Lateral Drying, Journal of the American Ceramic Society **98**, 2214 (2015).

Appendices

I Derivation of Characteristic Scales

To obtain the scales used in equation (2.2), we begin by noting that the initial film height H provides a scale for z' and h'. Then, from lubrication theory, the lateral length scale $L = H/\epsilon$ is used for x', where $\epsilon = H/L \ll 1$. Denoting the scales for the lateral velocity v_x' and the vertical velocity v_z' as v_x^* and v_z^*, respectively, the continuity equation

$$\frac{\partial v_x'}{\partial x'} + \frac{\partial v_z'}{\partial z'} = 0 \tag{A1}$$

implies $v_z^* = \epsilon v_x^*$. From the kinematic condition,

$$v_z' = \frac{\partial h'}{\partial t'} + v_x' \frac{\partial h'}{\partial x'},$$

we obtain the scale t^* for t' as $t^* = H/v_x^*\epsilon$.

Now, substituting these scales into the x-momentum balance

$$\rho\left(\frac{\partial v_x'}{\partial t'} + v_x'\frac{\partial v_x'}{\partial x'} + v_z'\frac{\partial v_x'}{\partial z'}\right) = -\frac{\partial p'}{\partial x'} + \mu\left(\frac{\partial^2 v_x'}{\partial x'^2} + \frac{\partial^2 v_x'}{\partial z'^2}\right)$$

and assuming $\epsilon Re \ll 1$, where the Reynolds number $Re = \rho v_x^* H/\mu$, we obtain the pressure scale $p^* = \mu v_x^*/H\epsilon$. The normal-stress balance is, at leading order,

$$p' = -\frac{\partial^2 h'}{\partial x'^2}\sigma'. \tag{A2}$$

Substituting the scales obtained above and using $\sigma' \sim \sigma_0$ gives an expression for the velocity scale $v_x^* = \epsilon^3\sigma_0/\mu$.

The result that appears in equation (2.1) is obtained from the tangential-stress balance, which at leading order is

$$\mu\frac{\partial v_x'}{\partial z'} = -\frac{\partial \sigma'}{\partial x'}. \tag{A3}$$

The left-hand side scales as $\mu v_x^*/H$, and the right-hand side scales as $\Delta\sigma\omega_0/L$. Substituting $v_x^* = \epsilon^3\sigma_0/\mu$ gives equation (2.1).

II Solution of Convection Equation

In this section we derive characteristics (2.34) used in §B of chapter 2. The method of characteristics seeks characteristic curves $(t, x(t), z(t))$ on which the solution to equations (2.32) is constant. This leads to the system of nonlinear ODEs

$$\frac{\partial x}{\partial t} = v_m z \sin(x), \quad \frac{\partial z}{\partial t} = \frac{v_m}{2} z^2 \cos(x), \tag{A4}$$

subject to the initial conditions $x = x_0$ and $z = z_0$. This system is autonomous, allowing us to seek a solution for z of the form $z = z(x(t))$ so that

$$\frac{\partial z}{\partial t} = \frac{\partial z}{\partial x}\frac{\partial x}{\partial t}. \tag{A5}$$

Inserting the time derivatives from equation (A4) and simplifying yields

$$\frac{1}{z}\frac{\partial z}{\partial x} = \frac{1}{2}\cot(x) \quad \Rightarrow \quad z(x(t)) = z_0\sqrt{\frac{\sin(x(t))}{\sin(x_0)}}. \tag{A6}$$

We then substitute this form for $z(x(t))$ into the former of equations (A4) and integrate to obtain the implicit solution for $x(t)$

$$\int_{x_0}^{x(t)} \frac{1}{\sin^{3/2}(y)}\,\mathrm{d}y = v_m \frac{z_0}{\sqrt{\sin(x_0)}} t. \tag{A7}$$

The integral in this solution is not trivial to evaluate; skipping some intermediate details, the key is to rewrite the integrand and then integrate by parts, giving

$$\int_{x_0}^{x(t)} \frac{1}{\sin^{3/2}(y)}\,\mathrm{d}y = \int_{x_0}^{x(t)} \sqrt{\sin(y)}\csc^2(y)\,\mathrm{d}y = -2\,\frac{\cos(y)}{\sqrt{\sin(y)}}\bigg|_{x_0}^{x(t)} - \int_{x_0}^{x(t)} \sqrt{\sin(y)}\,\mathrm{d}y\,. \tag{A8}$$

Through the change of variable $Y = \frac{1}{4}(\pi - 2y)$, the latter integral can be rewritten in terms of E, the elliptic integral of the second kind:

$$\int_{x_0}^{x(t)} \sqrt{\sin(y)}\,\mathrm{d}y = -2\int_{Y_0}^{Y} \sqrt{1 - 2\sin^2(Y)}\,\mathrm{d}Y = -2\,E\left(\frac{1}{4}(\pi - 2y)\Big|\,2\right)\bigg|_{x_0}^{x(t)}. \tag{A9}$$

Denoting the function f as

$$f(x) = 2E\left(\frac{1}{4}(\pi - 2x)\Big|\,2\right) - 2\frac{\cos(x)}{\sqrt{\sin(x)}} \tag{A10}$$

and putting together equations (A7), (A8), and (A9) yields

$$\int_{x_0}^{x(t)} \frac{1}{\sin^{3/2}(y)}\,\mathrm{d}y = f(y)\Big|_{x_0}^{x(t)} \quad \Rightarrow \quad x(t) = f^{-1}\left(f(x_0) + v_m \frac{z_0}{\sqrt{\sin(x_0)}} t\right). \tag{A11}$$

III Higher-Order Terms in VA Approximation

In the vertical-averaging (VA) approximation, one expands the concentration field in a perturbation series given by equation (3.16). Using this, one derives governing equation (3.19) and averages to obtain equation (3.22). By subtracting these two equations, we obtain

$$\frac{\partial^2 c_1}{\partial z^2} = (v_{x,0} - \overline{v_x}) \frac{\partial c_0}{\partial x} + \frac{1}{hPe} \frac{\partial h}{\partial x} \frac{\partial c_0}{\partial x} + \frac{c_0}{h} EJ, \tag{A12}$$

which gives c_1 purely in terms of c_0 and h, and this can be integrated twice to obtain

$$c_1 - c_1|_{z=0} = \left[\int_0^z \int_0^{z'} v_{x,0} - \overline{v_x} \, \mathrm{d}z'' \, \mathrm{d}z' \right] \frac{\partial c_0}{\partial x} + \frac{z^2}{2hPe} \frac{\partial h}{\partial x} \frac{\partial c_0}{\partial x} + \frac{z^2 c_0}{2h} EJ, \tag{A13}$$

$$\int_0^z \int_0^{z'} v_{x,0} - \overline{v_x} \, \mathrm{d}z'' \, \mathrm{d}z' = -\frac{1}{6} \left(\frac{1}{4} z^4 - h z^3 + h^2 z^2 \right) \frac{\partial^3 h}{\partial x^3} - \frac{1}{2} \left(\frac{1}{3} z^3 - \frac{1}{2} h z^2 \right) \frac{\partial c_0}{\partial x}. \tag{A14}$$

The boundary conditions for c_1 given by equations (3.21) are insufficient to fully determine c_1, so we enforce the condition

$$\frac{1}{h} \int_0^h c_1 \, \mathrm{d}z = 0. \tag{A15}$$

This implies that c_0 is the vertical average of c and that c_1 gives a perturbation around this average. We then have

$$c_1|_{z=0} = -\left[\frac{1}{h} \int_0^h \int_0^z \int_0^{z'} v_{x,0} - \overline{v_x} \, \mathrm{d}z'' \, \mathrm{d}z' \, \mathrm{d}z \right] \frac{\partial c_0}{\partial x} - \frac{h}{6Pe} \frac{\partial h}{\partial x} \frac{\partial c_0}{\partial x} - \frac{h c_0}{6} EJ, \tag{A16}$$

$$\frac{1}{h} \int_0^h \int_0^z \int_0^{z'} v_{x,0} - \overline{v_x} \, \mathrm{d}z'' \, \mathrm{d}z' \, \mathrm{d}z = -\frac{1}{45} h^4 \frac{\partial^3 h}{\partial x^3} + \frac{1}{24} h^3 \frac{\partial c_0}{\partial x}. \tag{A17}$$

To evaluate the magnitude of Marangoni stresses, we require the concentration at the interface $c_1|_{z=h}$. With the above, this is given by

$$c_1|_{z=h} = \frac{1}{72} \left(-\frac{7}{5} h^4 \frac{\partial^3 h}{\partial x^3} + h^3 \frac{\partial c_0}{\partial x} \right) \frac{\partial c_0}{\partial x} + \frac{h}{3Pe} \frac{\partial h}{\partial x} \frac{\partial c_0}{\partial x} + \frac{h c_0}{3} EJ. \tag{A18}$$

IV Solution of Laplace's Equation

We wish to solve Laplace's equation $\boldsymbol{\nabla}^2 u = 0$ for the function u on the rectangular domain $(x, z) \in [0, L_x] \times [0, L_z]$ with periodic conditions in x and the following conditions in z,

$$u|_{z=0} = f(x), \qquad u|_{z=L_z} = 0. \tag{A19}$$

Decomposing $u = \phi(x)\Psi(z)$ and substituting into Laplace's equation yields the two ordinary differential equations

$$\frac{\partial^2 \phi}{\partial x^2} + \lambda^2 \phi = 0, \qquad \frac{\partial^2 \Psi}{\partial z^2} - \lambda^2 \Psi = 0, \tag{A20}$$

where λ is an undetermined (eigen)value. Considering the periodic conditions in x, we must have $\sqrt{\lambda} = 2\pi k / L_x$ for $k \in \mathbb{Z}$ and solutions are of the form

$$\phi(x) = A e^{\frac{2\pi k}{L_x} ix}, \qquad \Psi(z) = B e^{\frac{2\pi k}{L_x} z} + C e^{-\frac{2\pi k}{L_x} z}. \tag{A21}$$

Requiring that $u|_{z=L_z} = 0$ gives the relation $B = -Ce^{-4\pi k\ell}$ where $\ell = L_z/L_x$. The function u is thus of the form

$$u(x, z) = \sum_k A_k e^{\frac{2\pi k}{L_x} ix} \left(e^{-\frac{2\pi k}{L_x} z} - e^{\frac{2\pi k}{L_x} z - 4\pi k\ell} \right), \tag{A22}$$

where $\{A_k\}_{k\in\mathbb{Z}}$ are constants. At $z = 0$, we have $u(x, z = 0) = f(x)$ and thus

$$f(x) = \sum_k A_k e^{\frac{2\pi k}{L_x} ix} \left(1 - e^{-4\pi k\ell} \right). \tag{A23}$$

Multiplying by the basis function $e^{-\frac{2\pi m}{L_x} ix}$ and applying the operator $\frac{1}{L_x} \int_0^{L_x} \cdot \, \mathrm{d}x$ gives expressions for the unknown constants:

$$A_m = \frac{1}{L_x} \frac{1}{1 - e^{-4\pi m\ell}} \int_0^{L_x} f(x) e^{-\frac{2\pi m}{L_x} ix} \, \mathrm{d}x = \frac{\tilde{f}_m}{1 - e^{-4\pi m\ell}}, \tag{A24}$$

where $\tilde{f}_m$ is the m-th Fourier coefficient of f.

The flux at the interface $z = 0$ is obtained by Fick's law:

$$J = -\left. \frac{\partial u}{\partial z} \right|_{z=0} = \sum_k \frac{2\pi k}{L_x} A_k e^{-\frac{2\pi k}{L_x} ix} \left(1 + e^{-4\pi k\ell} \right) = \frac{2\pi}{L_x} \sum_k \tilde{f}_k e^{-\frac{2\pi k}{L_x} ix} k \coth(2\pi k\ell). \tag{A25}$$

The value for $k = 0$ must be taken in a limiting sense. It is, however, instructive to separate it from the sum to see

$$J = \frac{\overline{f}}{L_z} + \frac{2\pi}{L_x} \sum_{k\neq 0} \tilde{f}_k e^{-\frac{2\pi k}{L_x} ix} k \coth(2\pi k\ell), \tag{A26}$$

where $\overline{f} = \tilde{f}_0$ is the average of f over $(0, L_x)$. Taking $L_x = 2\pi/\alpha$ and $L_z = \mathscr{L}$ as in §C of chapter 3, the solution reads

$$J = \frac{\overline{f}}{\mathscr{L}} + \sum_{k \neq 0} \tilde{f}_k e^{-\alpha k i x} \alpha k \coth(\alpha k L_z), \tag{A27}$$

which is equation (3.36). One may recognize this solution as a discrete Fourier transform, and thus truncations of it can be efficiently computed by FFT algorithms.

V Additional Figures for Chapter 3

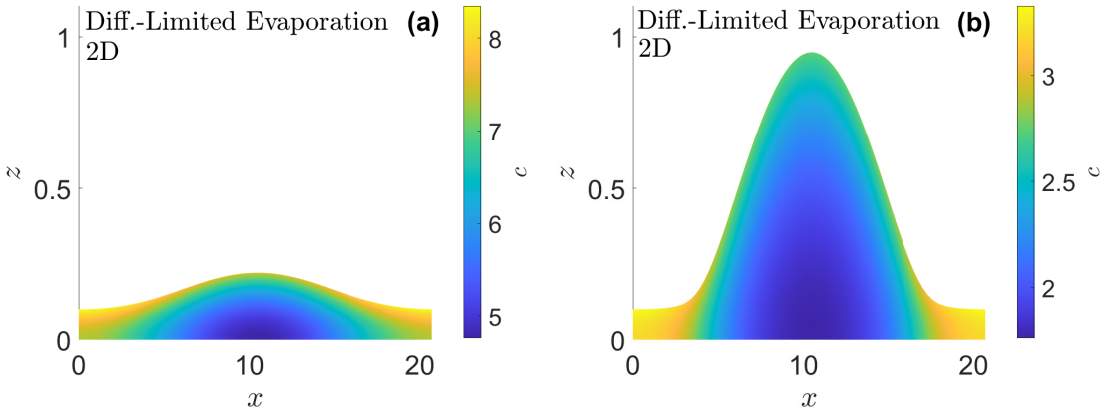

Figure A1: Concentration contours for $Pe = 4.6 \times 10^5$ at $t = t_{max}$ for (a) $\mathscr{L} = 1$ and (b) $\mathscr{L} = 10$ from the 2D description under diffusion-limited evaporation. The differences in the film-height perturbations result from larger or smaller vertical gradients from faster or slower evaporation.

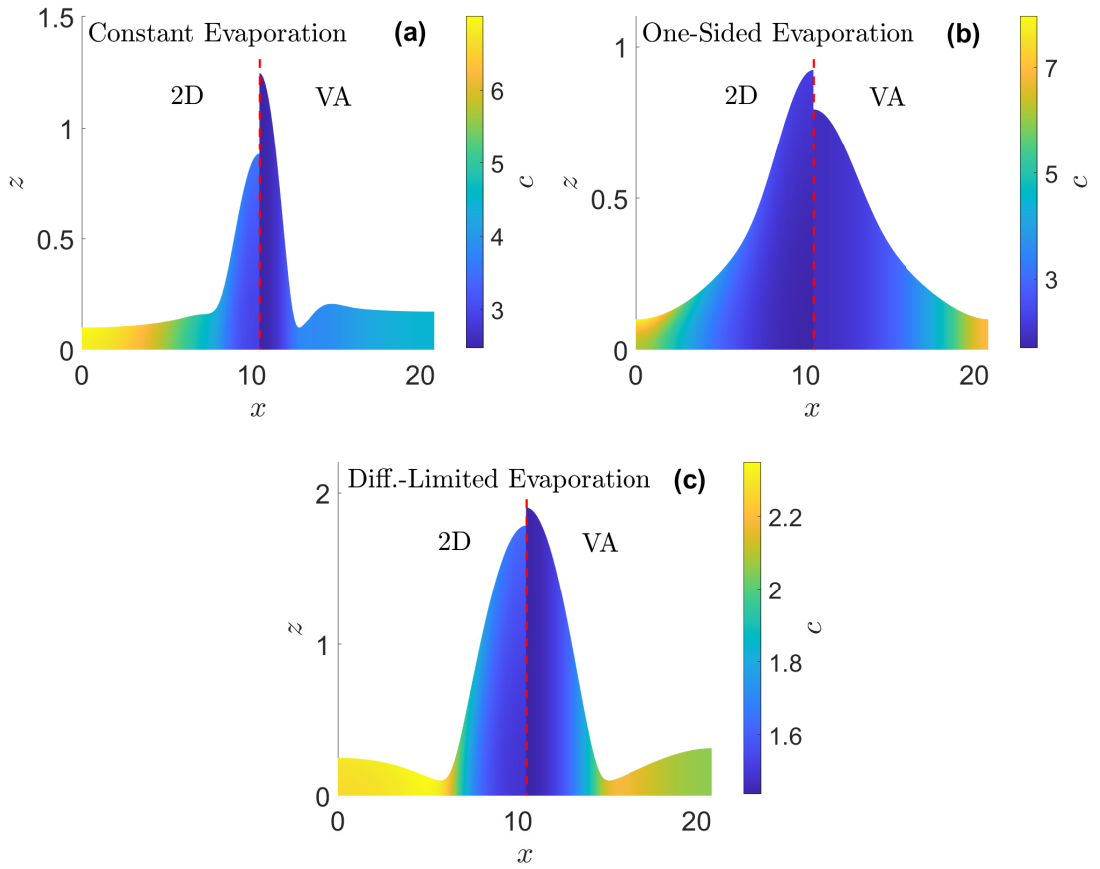

Figure A2: Alternate presentation of figure 2 from the main text. The left half of each panel is the prediction from the 2D description, while the right half is the prediction from the VA approximation.

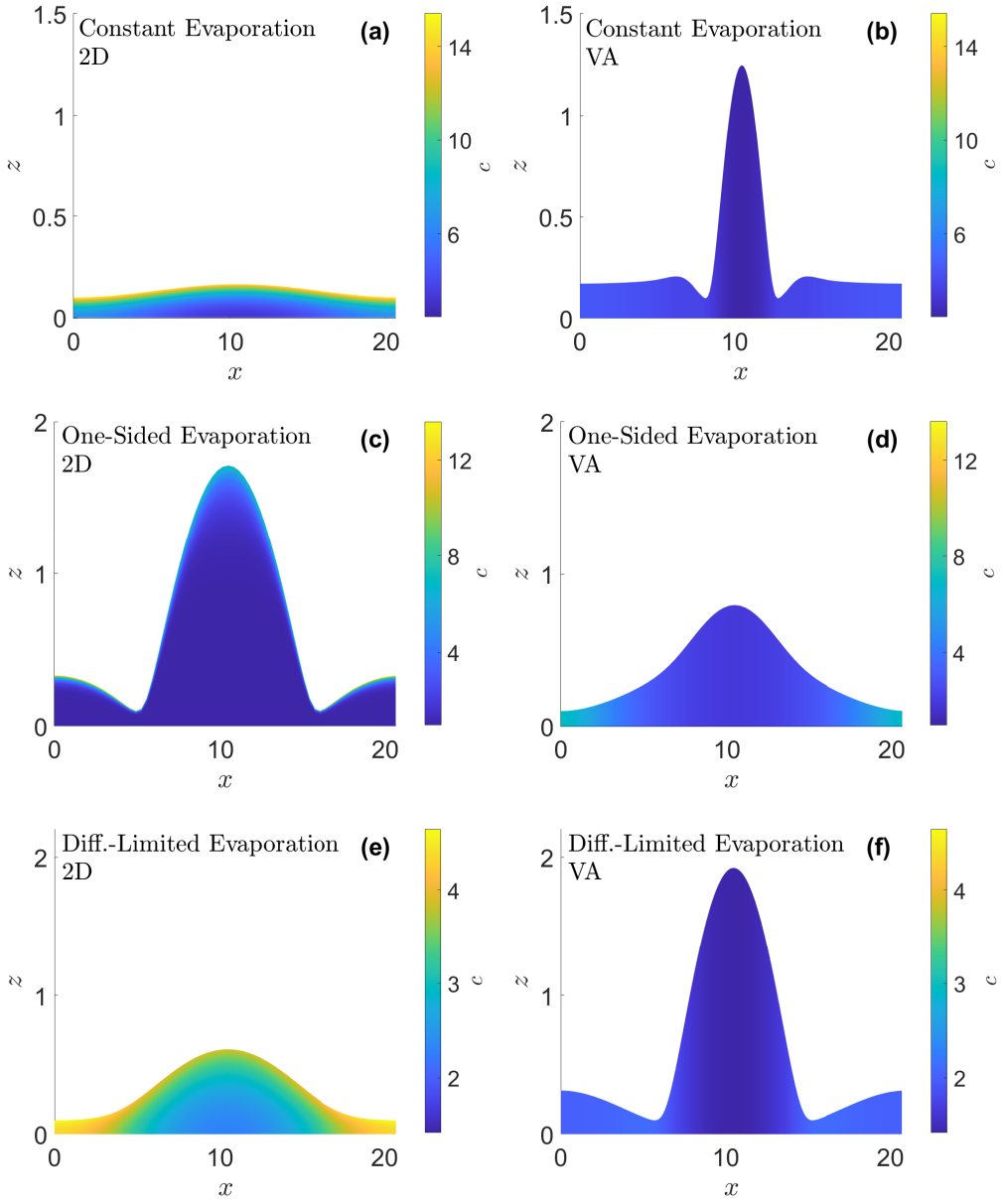

Figure A3: Concentration contours for $Pe = 4.6 \times 10^5$, $E = 3 \times 10^{-3}$, and $\epsilon = 0.1$ at $t = t_{max}$. Note the stark qualitative differences in both the film-height and solute concentration profiles. The value of Pe chosen is large enough to make clear the differences between each approach. The corresponding times are (a) $t_{max} = 2.89 \times 10^2$, (b) $t_{max} = 2.35 \times 10^2$, (c) $t_{max} = 8.84 \times 10^1$, (d) $t_{max} = 1.41 \times 10^2$, (e) $t_{max} = 2.81 \times 10^3$, and (f) $t_{max} = 1.37 \times 10^3$.

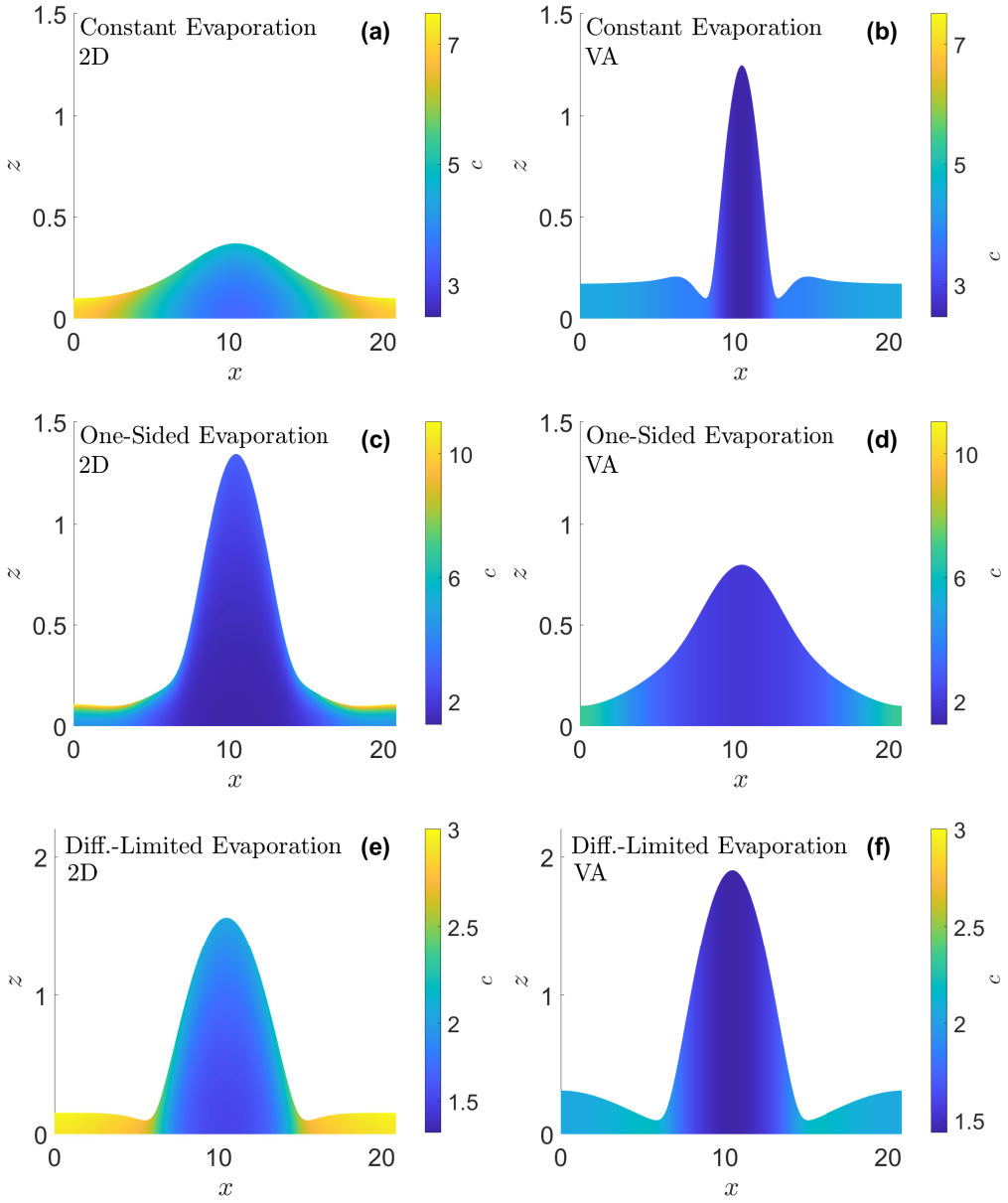

Figure A4: Concentration contours for $Pe = 6 \times 10^4$, $E = 3 \times 10^{-3}$, and $\epsilon = 0.1$ at $t = t_{max}$. Note the stark qualitative differences in both the film-height and solute concentration profiles. The value of Pe chosen is large enough to make clear the differences between each approach. The corresponding times are (a) $t_{max} = 2.65 \times 10^2$, (b) $t_{max} = 2.35 \times 10^2$, (c) $t_{max} = 1.32 \times 10^2$, (d) $t_{max} = 1.41 \times 10^2$, (e) $t_{max} = 8.50 \times 10^2$, and (f) $t_{max} = 6.76 \times 10^2$.

VI Effect of Droplet Height on Gas Phase Concentration

We can rigorously justify the change in domain $z^* \in (\epsilon h, \infty) \mapsto z^* \in (0, \infty)$ discussed in §2 of chapter 4 by the mapping

$$z^* \mapsto z^* - \epsilon h. \tag{A28}$$

Note that z^* derivatives are unaffected by this translation, but x derivatives must be transformed using the chain rule:

$$\frac{\partial}{\partial x} \mapsto \frac{\partial}{\partial x} - \epsilon \frac{\partial h}{\partial x} \frac{\partial}{\partial z^*} = \frac{\partial}{\partial x} + O(\epsilon). \tag{A29}$$

The correction in equation (A29) is $O(\epsilon)$ and may be neglected provided that derivatives of h and c_g are $O(1)$. Thus, x-derivatives are also unaffected (up to $O(\epsilon)$) and this change of domain causes no change in the governing equations; we may neglect the droplet height at $z^* = \epsilon h$, instead applying boundary conditions at $z^* = 0$, with only $O(\epsilon)$ error.

VII Detailed Derivation of Numerical Method for Chapter 4

Here we describe the procedure for solving the axisymmetric Laplace's equation with the hybrid spectral-finite-difference method described in §III of chapter 4. For ease of use, we present this method for a more general problem than that considered in §III of chapter 4.

We wish to numerically solve for the concentration c_g governed by

$$0 = \boldsymbol{\nabla}^2 c_g = \frac{\partial^2 c_g}{\partial z^{*2}} + \frac{1}{r}\frac{\partial}{\partial r}\left(r\frac{\partial c_g}{\partial r}\right) \tag{A30}$$

on the the semi-infinite domain $(r, z^*) \in (0, d) \times (0, \infty)$. The concentration c_g is subject to the symmetric boundary condition $c_g(r) = c_g(-r)$ as well as $c_g(r = d) = 0$ and $c_g \to 0$ as $z^* \to \infty$. At $z^* = 0$, it takes on the value $c_g(r, z^* = 0) = f(r)$. Since equation (A30) must be solved at each time step, the goal of this numerical method is to reduce equation (A30) to a matrix equation that can be quickly and efficiently solved. Note that we do not explicitly include time-dependence in this derivation because it can be encapsulated in the boundary data f.

We begin by writing c_g as an expansion of Laguerre functions L_n,

$$c_g(r, z^*) \approx \sum_{n=0}^{M-1} a_n(r) L_n(z^*), \tag{A31}$$

where the coefficients $a_n(r)$ vary radially. For now, we assume that there is some set of coefficients $a_n''(r)$ such that

$$\frac{\partial^2 c_g}{\partial z^{*2}} = \sum_{n=0}^{M-1} a_n(r)\frac{\partial^2 L_n}{\partial z^{*2}} = \sum_{n=0}^{M-1} a_n''(r) L_n(z^*). \tag{A32}$$

Then, substituting equation (A31) into equation (A30) and applying orthogonality of the Laguerre functions gives, for each n,

$$a_n''(r) + \frac{1}{r}\frac{\partial}{\partial r}\left(r\frac{\partial a_n}{\partial r}\right) = 0. \tag{A33}$$

We first determine a_n'', and then show how we discretize in r.

The Laguerre functions are defined as

$$L_n(x) = e^{-x/2}\ell_n(x), \tag{A34}$$

where $\ell_n(x)$ is the n-th Laguerre polynomial which satisfies

$$\frac{\partial \ell_n}{\partial x} = -\sum_{k=0}^{n-1} \ell_k(x). \tag{A35}$$

Thus, we have

$$\frac{\mathrm{d}L_n}{\mathrm{d}x} = \frac{\mathrm{d}}{\mathrm{d}x}\left(e^{-x/2}\ell_n(x)\right) \tag{A36}$$

$$= -\frac{1}{2}e^{-x/2}\ell_n(x) - e^{-x/2}\sum_{k=0}^{n-1}\ell_k(x) \tag{A37}$$

$$= -\frac{1}{2}L_n(x) - \sum_{k=0}^{n-1} L_k(x). \tag{A38}$$

Defining the lower triangular matrix $\mathbf{D}$ and vector of Laguerre functions $\mathbf{L}$ as

$$(\mathbf{D})_{i,j} = \begin{cases} 0 & i \geq j \\ 1 & i < j \end{cases}, \qquad (\mathbf{L})_i = L_i(x), \tag{A39}$$

we can use equation (A38) to write

$$\frac{\mathrm{d}\mathbf{L}}{\mathrm{d}x} = \left(-\frac{1}{2}\mathbf{I} - \mathbf{D}\right)\mathbf{L}, \tag{A40}$$

where $\mathbf{I}$ is the identity matrix. Thus,

$$\frac{\mathrm{d}^2\mathbf{L}}{\mathrm{d}x^2} = \left(-\frac{1}{2}\mathbf{I} - \mathbf{D}\right)^2\mathbf{L} = \underbrace{\left(\frac{1}{4}\mathbf{I} + \mathbf{D} + \mathbf{D}^2\right)}_{\mathbf{D}_z}\mathbf{L}. \tag{A41}$$

With a vector of coefficients $\mathbf{a}(r)$, we have $c_g = \mathbf{a}^T\mathbf{L}$ and thus

$$\frac{\partial^2 c_g}{\partial z^{*2}} = \mathbf{a}^T\mathbf{D}_z\mathbf{L}, \tag{A42}$$

so the coefficients a_n'' are given in vector form by $\mathbf{a}'' = \left(\mathbf{a}^T\mathbf{D}_z\right)^T$.

We now discretize each coefficient $a_n(r)$ into its values at a discrete set of N nodes $\{r_j\}$ placed in the center of cells. We then apply a positivity-preserving second-order centered finite-difference method that gives

$$\frac{1}{r}\frac{\partial}{\partial r}\left(r\frac{\partial a_n}{\partial r}\right)\bigg|_{r_j} = \frac{2}{r_j\Delta r_j}\left[\alpha_j a_n(r_{j-1}) - (\alpha_j + \alpha_{j+1})\, a_n(r_j) + \alpha_{j+1}a_n(r_{j+1})\right], \tag{A43}$$

where

$$\alpha_j = \frac{r_{j-1/2}}{\Delta r_j + \Delta r_{j-1}}, \tag{A44}$$

$r_{j-1/2}$ is the position of the boundary between cells j and $j-1$, and Δr_j is the width of cell j. Note that the boundary conditions in r define the values of ghost nodes needed to evaluate the above expressions near the boundaries of the domain. Defining the $N \times M$ coefficient matrix $(\mathbf{A})_{i,j} = a_j(r_i)$ and r-derivative matrix $\mathbf{D}_r$ as

$$(\mathbf{D}_r)_{i,j} = \frac{2}{r_i \Delta r_i} \begin{cases} \alpha_i & j = i-1 \\ -(\alpha_i + \alpha_{i+1}) & j = i \\ \alpha_{i+1} & j = i+1 \\ 0 & \text{otherwise} \end{cases}, \tag{A45}$$

the discrete form of the left-hand side of equation (A33) is

$$\mathbf{A}\mathbf{D}_z + \mathbf{D}_r\mathbf{A}. \tag{A46}$$

If a higher order-of-accuracy is desired, one can replace the second-order method here for one of higher order. Doing so simply changes the entries of $\mathbf{D}_r$ and the rest of this method is unchanged.

Unfortunately the form of equation (A46) is not computationally useful since the coefficient matrix $\mathbf{A}$ is both left and right multiplied by other matrices. However, we can remedy this by stacking the matrix $\mathbf{A}$ into a vector and expressing the right multiplication as a left multiplication. Define the mapping vectors $\mathbf{I}$ and $\mathbf{J}$ and coefficient vector $\mathbf{u}$ (all with lengths NM) such that

$$(\mathbf{u})_i = a_{J_i}(r_{I_i}) = (\mathbf{A})_{I_i,J_i}. \tag{A47}$$

Note that $J_i \in \{1, ..., M\}$ and $I_i \in \{1, ..., N\}$. Now, we can use the stacked z-derivative matrix

$$(\mathbf{D}_z^*)_{i,j} = \begin{cases} (\mathbf{D}_z)_{J_j,J_i} & I_i = I_j \\ 0 & \text{otherwise} \end{cases}. \tag{A48}$$

To see this matrix gives the desired result (left multiplication instead of right), note that

$$(\mathbf{D}_z^*\mathbf{u})_i = \sum_{j=1}^{NM} (\mathbf{D}_z^*)_{i,j} (\mathbf{u})_j = \sum_{\substack{j \\ I_i=I_j}} (\mathbf{D}_z^*)_{i,j} a_{J_j}(r_{I_j}) = \sum_{\substack{j \\ I_i=I_j}} (\mathbf{D}_z)_{J_j,J_i} a_{J_j}(r_{I_i}). \tag{A49}$$

Now, for a given index i, there are precisely M indices j such that $I_i = I_j$ (i.e., $\mathbf{I}$ contains each value in $\{1, ..., N\}$ exactly M times). These indices must be distinct, and furthermore, the corresponding J_j cover $\{1, ..., M\}$. Thus, the above sum can

be replaced by

$$(\mathbf{D}_z^*\mathbf{u})_i = \sum_{j=1}^{M} (\mathbf{D}_z)_{j,J_i}\, a_j(r_{I_i}) = (\mathbf{A}\mathbf{D}_z)_{I_i,J_i}\,. \tag{A50}$$

Thus, we have turned the right multiplication by a derivative matrix into a left multiplication.

We can similarly form the stacked r-derivative matrix

$$(\mathbf{D}_r^*)_{i,j} = \begin{cases} (\mathbf{D}_r)_{I_i,I_j} & J_i = J_j \\ 0 & \text{otherwise} \end{cases}. \tag{A51}$$

By arguments similar to those above, one can show that

$$(\mathbf{D}_r^*\mathbf{u})_i = (\mathbf{D}_r\mathbf{A})_{I_i,J_i}\,. \tag{A52}$$

Therefore, equation (A33) can also be written

$$\mathbf{D}_z^*\mathbf{u} + \mathbf{D}_r^*\mathbf{u} = \underbrace{(\mathbf{D}_z^* + \mathbf{D}_r^*)}_{\mathbf{K}}\,\mathbf{u}. \tag{A53}$$

The boundary conditions in r are encoded in the r-derivative matrix $\mathbf{D}_r$. The boundary condition $c_g \to 0$ as $z^* \to \infty$ is naturally satisfied by the Laguerre function expansion, but the boundary condition at $z^* = 0$ is not. For this, we use boundary bordering. Noting that $L_n(0) = 1$, we have

$$c_g(r_k, z^* = 0) = \sum_{n=0}^{M-1} a_n(r_k) = f(r_k) \tag{A54}$$

for each k. Thus, we redefine $\mathbf{K}$ and define the boundary data vector $\mathbf{c}$ as

$$(\mathbf{K})_{i,j} = \begin{cases} 1 & J_i = M, I_i = I_j \\ 0 & J_i = M, I_i \neq I_j \\ (\mathbf{D}_z^* + \mathbf{D}_r^*)_{i,j} & \text{otherwise} \end{cases}, \qquad (\mathbf{c})_i = \begin{cases} f(r_{I_i}) & J_i = M \\ 0 & \text{otherwise} \end{cases}, \tag{A55}$$

giving the linear system

$$\mathbf{K}\mathbf{u} = \mathbf{c}. \tag{A56}$$

This enforces that the quantity in equation (A53) vanishes except for a set of N equations that are replaced with equation (A54) for each k (the choice of $J_i = M$ is heuristic; formally, we can replace any set of N equations). While $\mathbf{K}$ has $(NM)^2$ components, it is strongly banded with proper choice of the mapping vectors $\mathbf{I}$ and $\mathbf{J}$, so equation (A56) can be quickly solved by a banded-system solver. While this must be done every time the boundary data $f(r)$ changes, $\mathbf{K}$ is constant and can be precomputed (and factorized using banded LU factorization).

With equation (A31), the evaporative flux J is given by

$$J = -\left.\frac{\partial c_g}{\partial z^*}\right|_{z^*=0} \approx -\sum_{n=0}^{M-1} a'_n(r). \tag{A57}$$

In discrete matrix form, the coefficients a'_n are (from equation (A40))

$$\mathbf{A}' = \mathbf{A}\left(-\frac{1}{2}\mathbf{I} - \mathbf{D}\right). \tag{A58}$$

One then computes the sum $-\sum_j (\mathbf{A}')_{i,j}$ to obtain the evaporative flux $J(r_i)$ at each node position r_i.